

**INVERSE MODELING OF DIFFUSIVE PROCESSES
USING INSTANTANEOUS MEASUREMENTS AND
STOCHASTIC DIFFERENTIAL EQUATIONS**

BY

ASHRAF MOHAMED

M.Sc., Cairo University, Cairo, Egypt, 2005

B.Eng., Cairo University, Cairo, Egypt, 2002

A Thesis

Submitted to the School of Graduate Studies in partial fulfilment of the requirements

for the degree of

Doctor of Philosophy

Department of Electrical and Computer Engineering

McMaster University, 2010

©Copyright by Ashraf Mohamed, Jan 2010

Doctor of Philosophy McMaster University, Hamilton, ON, Canada

Master of Science Cairo University, Cairo, Egypt

Bachelor of Engineering Cairo University, Cairo, Egypt

TITLE: Inverse Modeling of Diffusive Processes Using
Instantaneous Measurements and
Stochastic Differential Equations

AUTHOR: Ashraf Mohamed, M.Sc. (Cairo University)

SUPERVISOR: Professor A. Jeremic

NUMBER OF PAGES: xv, 141

Abstract

Modeling the dispersion of diffusive sources and signal processing algorithms for its prediction is an important issue in many applications such as cardiac activation, drug delivery, and environmental monitoring. This work focuses on the development of computationally efficient algorithms for modeling diffusion processes and estimation of their different properties.

First, we implement the well known Fick's law of diffusion for localizing and estimating the properties of diffusive sources. Moreover, we propose a new model for the cardiac activation using inhomogeneous reaction-diffusion equations in the presence of diffusivity disorders. We also derive corresponding statistical signal processing algorithms for estimating (localizing) parameters describing these anomalies using ECG/MCG sensor arrays.

However, in some applications, such as drug delivery and capillary exchange process, where low-intensity diffusive sources are considered, random effects such as Brownian motion should be accounted for. Hence, we propose a computationally efficient framework for localizing low-intensity diffusive sources using stochastic differential equations. To achieve computational efficiency, we model the dispersion using the Fokker-Planck equation and derive corresponding inverse model and maximum likelihood estimator of source intensity, location and release time. Also, we expand our stochastic model to account for drift and propose an algorithm for the estimation of boundary properties.

Finally, we present a novel technique for modeling the exchange process and particle clearance in capillary networks using coupled stochastic- differential and Navier-Stokes equations. Numerical examples are used to demonstrate the applicability of our models.

Acknowledgements

This thesis arose in part out of years of research that has been done since I came to McMaster University. By that time, I have worked with a great number of people whose contribution in assorted ways to the research and the making of the thesis deserved special mention. It is a pleasure to convey my gratitude to them all in my humble acknowledgment.

Foremost, I would like to express my sincere gratitude to my advisor Prof. Aleksandar Jeremic for the continuous support of my Ph.D study and research, for his patience, motivation, enthusiasm, and immense knowledge. His guidance helped me in all the time of research and writing of this thesis. I could not have imagined having a better advisor and mentor for my Ph.D study.

Besides my advisor, I would like to thank Prof. Mohamed Bakr and Prof. Hubert deBruin for their encouragement and insightful comments.

Last but not the least, I owe everlasting gratefulness to my parents, family, and friends who pleasantly involved themselves in helping me undertake this dissertation and supported me spiritually throughout my life.

Contents

Descriptive Note	ii
Abstract	iii
Acknowledgements	iv
List of Figures	ix
List of Tables	xiii
Glossary	xiv
1 Introduction	1
1.1 Forward Diffusion Problems	1
1.1.1 Diffusion in Chemical Systems	2
1.1.2 Diffusion in Biomedical Systems	3
1.1.3 Diffusion in Financial Systems	4
1.2 Inverse Diffusion Problems	6
2 Estimation of the Properties of Diffusive Sources Using Classical Diffusion	

Model	9
2.1 Introduction	9
2.2 Classical Diffusion Model	11
2.3 Measurement Model	14
2.4 Numerical Results	16
2.5 Conclusions	17
3 An Inverse Model for Localization of Low-diffusivity Regions in the Heart Using ECG/MCG Sensor Arrays	22
3.1 Introduction	22
3.2 Physical Model	24
3.3 Measurement Model and Statistical Model	26
3.4 Parameter Estimation	28
3.5 Numerical Examples	30
3.6 Conclusions	36
3.7 Publications	36
4 Estimation of the Properties of Diffusive Sources Using Stochastic Differential Equations	37
4.1 Introduction	37
4.2 Physical Model	40
4.3 Statistical Model	43
4.4 Numerical Examples	47
4.5 Conclusions	50
4.6 Publications	51

5	Estimation of Boundary Properties Using Stochastic Differential Equations	58
5.1	Introduction	58
5.2	Physical Model	60
5.3	Statistical Model	64
5.4	Estimation Algorithm	68
5.5	Numerical Results	69
5.5.1	Sphere with absorbing segment	70
5.5.2	Cylinder with absorbing segment	76
5.6	Conclusions	79
5.7	Publications	83
6	Modeling the Bacterial Clearance in Capillary Network Using Coupled Stochastic-Differential and Navier-Stokes Equations	84
6.1	Introduction	84
6.2	Capillary Blood Flow Model	87
6.3	Modeling the Exchange Process	92
6.4	Segmentation Model of the Capillary Network	98
6.5	Modeling the Exchange of Multiple Particles	105
6.6	Conclusions	109
6.7	Publications	109
7	Concluding Remarks	110
A	Solution of the Diffusion Equation	112
B	Computation of the Classical Estimators for \bar{c}_0 and \bar{r}_0	115

C Derivation of the Likelihood Function in the Presence of Noise	117
D Values of P_{A_i,t_j} and P_{T_i,t_j} for 50 Capillary Sections	119
Bibliography	128

List of Figures

2.1	Mean square error for estimating n_0 and r_0 as a function of SNR and the number of sensors for 1000 particles. a) MSE for estimating $n_0 - r_0$ is known. b) MSE for estimating $r_0 - n_0$ is known.	18
2.2	Mean square error for estimating n_0 and r_0 as a function of SNR and the number of sensors for 1000 particles. a) MSE for estimating $n_0 - r_0$ is unknown. b) MSE for estimating $r_0 - n_0$ is unknown.	19
2.3	Mean square error for estimating n_0 and r_0 as a function of SNR and the number of sensors for 1000 particles. a) MSE for estimating $n_0 - r_0$ is known. b) MSE for estimating $r_0 - n_0$ is known.	20
2.4	Mean square error for estimating n_0 and r_0 as a function of SNR and the number of sensors for 1000 particles. a) MSE for estimating $n_0 - r_0$ is unknown. b) MSE for estimating $r_0 - n_0$ is unknown.	21
3.1	Mesh geometry used for numerical study.	30
3.2	Activation wavefront, at a) $t = T/3$, b) $t = 2T/3$	32
3.3	Body surface map of electric potential, at a) $t = T/3$, b) $t = 2T/3$	33
3.4	Body surface map of magnetic field, at a) $t = T/3$, b) $t = 2T/3$	34
3.5	Mean square error for estimating the size of the anomaly.	35

3.6	Mean square error for estimating the location of the anomaly.	35
4.1	Evolution of particles in two dimensional space. a) 50000 particles - green. b) 1000 particles - red.	44
4.2	Mean square error for estimating n_0 and r_0 as a function of number of sensors and time samples for 500 particles - in the absence of noise. a) MSE for estimating $n_0 - r_0$ is known. b) MSE for estimating $r_0 - n_0$ is known.	52
4.3	Mean square error for estimating n_0 and r_0 as a function of number of sensors and time samples for 500 particles - in the absence of noise. a) MSE for estimating $n_0 - r_0$ is unknown. b) MSE for estimating $r_0 - n_0$ is unknown.	53
4.4	Mean square error for estimating n_0 and r_0 as a function of number of sensors and time samples for 1000 particles - in the absence of noise. a) MSE for estimating $n_0 - r_0$ is known. b) MSE for estimating $r_0 - n_0$ is known.	54
4.5	Mean square error for estimating n_0 and r_0 as a function of number of sensors and time samples for 1000 particles - in the absence of noise. a) MSE for estimating $n_0 - r_0$ is unknown. b) MSE for estimating $r_0 - n_0$ is unknown.	55
4.6	Mean square error for estimating n_0 and r_0 as a function of SNR and the number of sensors for 1000 particles. a) MSE for estimating $n_0 - r_0$ is known. b) MSE for estimating $r_0 - n_0$ is known.	56
4.7	Mean square error for estimating n_0 and r_0 as a function of SNR and the number of sensors for 1000 particles. a) MSE for estimating $n_0 - r_0$ is unknown. b) MSE for estimating $r_0 - n_0$ is unknown.	57

5.1	Bounded domain \mathcal{V} with boundary \mathcal{S}	60
5.2	Behavior of a particle near a reflecting boundary.	62
5.3	Specular reflection method. Solid dot represents a particle, hollow dot represents a hole.	63
5.4	Mean diffusion distance for 1000 particles at two different time samples - $D = 4.29 * 10^{-13}m^2/s$. Blue: $t = 0.02sec$, $d = 22.69 * 10^{-8}m$. Green: $t = 0.04sec$, $d = 32.09 * 10^{-8}m$	64
5.5	Closed circular domain with reflecting and absorbing boundaries - $R =$ $2mm$, $D = 4mm^2/s$, and $\pi/6 \leq l \leq \pi/3$	65
5.6	Evolution of $f(r, t)$ for a boundary problem.	66
5.7	Flow chart.	69
5.8	Sphere with absorbing segment defined by $(R, \theta_1 : \theta_2, \phi_1 : \phi_2)$	71
5.9	MLE error of the absorbing region - $n_0 = 500$	73
5.10	MLE error of the absorbing region - $n_0 = 1000$	73
5.11	Robustness curves with respect to MSE in D - $n_0 = 500$	74
5.12	Robustness curves with respect to MSE in D - $n_0 = 1000$	74
5.13	Robustness curves with respect to MSE in n_0 - $n_0 = 500$	75
5.14	Robustness curves with respect to MSE in n_0 - $n_0 = 1000$	75
5.15	Cylinder with absorbing segment defined by $(R, \phi_1 : \phi_2, z_1 : z_2)$	77
5.16	MLE error of the absorbing region - no drift.	79
5.17	MLE error of the absorbing region.	80
5.18	MLE error of the absorbing region - known drift.	80
5.19	MLE error of the absorbing region - unknown drift.	81
5.20	Robustness curves with respect to MSE in D - drift free.	81

5.21	Robustness curves with respect to MSE in $D - \beta = 0.5$	82
5.22	Robustness curves with respect to MSE in n_0 - drift free.	82
5.23	Robustness curves with respect to MSE in $n_0 - \beta = 0.5$	83
6.1	Axial velocity profile at $z = L/2$ for different slip coefficients.	91
6.2	Axial velocity profile along the axis $r = 0$ for different slip coefficients. . .	92
6.3	Radial velocity at two different levels of the capillary segment.	93
6.4	Pressure profile along the axis $z = 0$ of a capillary segment.	94
6.5	Cross section of the capillary showing the different mechanisms of trans- portation and different capillary boundaries.	97
6.6	Evolution of the probabilities of absorption and transmission of a single particle traveling from the arteriole to a venule via a capillary segment. . . .	99
6.7	Evolution of $f(r, t)$ inside a capillary segment.	100
6.8	Discretization of a capillary segment.	101
6.9	Probability of absorption of the i^{th} capillary section, for $i = 1, \dots, n$, as a function of capillary blood pressure.	102
6.10	Probability of transmission of the i^{th} capillary section, for $i = 1, \dots, n$, as a function of capillary blood pressure.	103
6.11	Comparison of the Finite Element and Segmentation Methods in calculat- ing P_A and P_T	106
6.12	Absorbing probability ($P_{tot,t_j}^{A_n}$) of a capillary segment starts at $40mmHg$. . .	108

List of Tables

4.1	The estimation results of classical and stochastic estimation	48
4.2	Minimum error achieved for different source intensities.	49
5.1	Computational times for FE and FD solvers.	72
5.2	Computational times for FE and FD solvers.	77
6.1	Capillary specifications.	90
D.1	P_{A_i,t_j} for 50 sections and 10 time steps.	123
D.2	P_{T_i,t_j} for 50 sections and 10 time steps.	127

Glossary

ECG	Electrocardiography
FD	Finite Difference
FDM	Finite Difference Method
FE	Finite Element
FEM	Finite Element Method
GLS	Generalized Least Squares
MCG	Magnetocardiography
ML	Maximum Likelihood
MLE	Maximum Likelihood Estimator
MSE	Mean Square Error
pdf	probability density function

PLC Product Like Cycle

PMF Probability Mass Function

SDE Stochastic Differential Equation

SM Segmentation Model

SNR Signal-to-Noise Ratio

Chapter 1

Introduction

1.1 Forward Diffusion Problems

Diffusion commonly refers to the spontaneous movement of a substance (gas, liquid, or solid) into its surrounding area. The molecules, or particles, that make up the substance distribute over time from an area of higher concentration to an area of lower concentration in order to create, at equilibrium, a uniform distribution of particles throughout the system. Diffusion is a natural process that requires no added energy to occur. It increases the entropy of the system [Biddle 00] and hence is an energetically favorable and irreversible process.

Diffusion is often important in systems experiencing an applied force. In a conducting material, the net motion of electrons in an electrical field quickly reaches a terminal velocity (resulting in a steady current described by Ohm's law) because of the thermal (diffusive) motions of atoms. The Einstein relation [Einstein 56] relates the diffusion coefficient to the mobility of particles. In cell biology, diffusion is a main form of transport within cells

and across cell membranes. The spreading of any quantity that can be described by the diffusion equation or a random walk model (e.g. concentration, heat, momentum, ideas, price) can be called diffusion.

In principle, diffusion can be stated by either classical or stochastic models. Classical representation models the mean field of diffusion which is widely used in problems such as modeling the diffusion of ions in the heart, heat diffusion, and diffusion of chemical plums in sea water. On the other hand, stochastic models account for the random fluctuations in dispersion patterns and can be used to model different biological systems such as molecular exchange in capillary networks and tissues. Some of the most important examples of diffusion processes are listed below.

1.1.1 Diffusion in Chemical Systems

Chemical diffusion occurs in a presence of concentration (or chemical potential) gradient and it result in net transport of mass from an area of higher concentration to an area of lower concentration. An example is H_2S in a test tube will slowly diffuse into the air of a lab until equilibrium is reached.

Accidental gas releases from industrial sites that results in dangerous chemical plumes makes the problem of tracking such plumes extremely important. The fear of biological terrorist attacks is another motive that made this subject a hot research topic to answer the question of what is the fastest and most accurate approach to locate and track possible chemical sources [Russell 01, Ishida 01, Dhariwal 04, Russell 00].

1.1.2 Diffusion in Biomedical Systems

Transport processes are essential to the function of biological systems. Fluids constitute a large portion of body weight and provide the conduit for transfer of nutrients and energy to and from tissues through out the body. In order to successfully analyze the physiological cellular processes in the body, the biomedical engineer need to understand the mechanism of transport processes, and to have the ability to solve the mathematical models that describes these mechanisms. In addition, the design and operation of many biomedical devices for diagnostics and therapeutics depend on the flow of fluids and transport of nutrients. Moreover, the analysis of the spread of some viruses has a great important in the design of different drugs.

Many processes in biomedical systems can be approximated by diffusion processes, this includes stochastic processes describing population growth, some stochastic processes in infectious diseases as well as processes involving gas exchange across the alveolar-capillary membrane. Dargatz [Dargatz 06] employed an extended SIR (Susceptible-Infected-Resistant) model for a probabilistic analysis of the spatio-temporal spread of influenza in Germany, where the diffusion process is utilized to describe the infection dynamics.

Dialysis, discovered by Thomas Graham (1805-1869), is an important application of diffusion. In dialysis a solution is passed over a semipermeable membrane, allowing solutes up to a certain size (but not larger molecules) to diffuse across the membrane to a second solution. Artificial kidney machines use dialysis to remove metabolic waste products, such as urea and creatinine, from the blood. In these machines, blood is circulated on one side of a semipermeable membrane (made from cellophane), while a dialysis fluid, which closely matches the chemical composition of blood, is circulated on the other side of the

membrane. The waste products diffuse from the blood into the dialysis fluid and are then discarded. Important blood components, such as the oxygen-carrying protein hemoglobin, are too large to enter the pores of the membrane and hence are retained in the blood.

A final example of the biological importance of diffusion is the exchange of gases to and from the blood that occurs in the alveolar membrane of the lungs. This membrane separates the flowing blood from the gases within the lung. Carbon dioxide (CO_2), a chemical end product of biological metabolism, is plentiful in venous blood that enters the lung. Release of the CO_2 from this blood occurs by its diffusion across the alveolar membrane, and this CO_2 is expelled upon exhalation. Inhalation brings air into the lung, and air contains 20.95% by volume of oxygen (O_2). Diffusion of O_2 across the alveolar membrane, in the other direction, allows its dissolution in the blood. Oxygen is carried, bound to hemoglobin, by the arterial blood to the cells where it is released, again by diffusion, for its use by the cells as the terminal oxidant of aerobic respiration.

Information about electrical conductivity distribution inside biological tissues is useful for many biomedical studies. Especially, conductivity mapping of a human brain would play great roles to enhance the accuracy of EEG or MEG source localization for brain function studies [Mosher 99, Baillet 01, Phillips 00]. Many studies are done on the estimation of human tissue properties [Farrell 92, Doornbos 99, Gabriel 96b] and its relation to some pathological diseases [Jossinet 96, Grill 94, Kadah 96].

1.1.3 Diffusion in Financial Systems

One fundamental marketing concept for managing resources commitments to a new product is the product life cycle (PLC). The PLC hypothesizes that sales of a new product, over

time in a target market, go through different stages of launch, growth, maturity, and decline. New product diffusion models focus on models that analytically capture the life cycle of a new product over time in a target market. These models have been applied to forecast the demand for a new product. To price stock derivatives, it is necessary to characterize the evolution of the price of the stock through time. General diffusion models with time varying volatility are the most commonly used by market practitioners, but they fail to capture the higher order moments (which lead to fat-tailed distributions) observed in stock prices. In the jump diffusion model, price change dynamics can be divided into two distinct forms:

1. A *normal*, continuous price diffusion process modeled by Geometric Brownian Motion with mean reversion and a volatility term structure. The term structure of forward volatilities coupled with mean reversion allows us to capture electricity price dynamics without spikes.
2. An *abnormal*, discontinuous jump process modeled by a Poisson distribution. These discontinuous price jumps are usually a result of outages, transmission constraints, etc.

Kou [Kou 02] proposed, for the purpose of option pricing, a double exponential jump-diffusion model in order to produce analytical solutions for a variety of option-pricing problems, including call and put options, interest rate derivatives, and path-dependent options. In addition, different jump-diffusion models were proposed by Merton [Hull] and other authors [Hanson 04, Scott 97, Zhang 97b, Ball 93].

1.2 Inverse Diffusion Problems

The main goal of collecting data is to gain meaningful information about a physical system of interest. However, in many situations the parameters that we wish to determine are different from the ones which we are able to measure, or have measured. If the measured data depends, in some way, on the parameters we want, then the data at least contains some information about those parameters. Starting with the data that we have measured, the problem of trying to estimate or reconstruct the parameters of interest is called an *inverse problem*.

Here are some typical inverse problems:

- **Model fitting:** according to some theoretical model, the value of a quantity y depends on another quantity x via an equation such as

$$y = a_0 + a_1x + a_2x^2 + a_3x^3 + \cdots + a_nx^n \quad (1.1)$$

Given a set of measured points (x_i, y_i) , we wish to determine the set of parameters a_i $i = 1, \dots, n$ and how confident are we of the result. More generally, the model can be more complicated and may depend on the parameters in a non-linear way. Determining the half-life of a radioactive material using measurements of the times at which decay products are detected is an example of model fitting.

- **Geometry and shape design:** determination of shape, size and location of geometries of interest is an inverse problem. One example is the detection of voids and cracks in fabrications such as ceramics [Bashkansky 97] and concrete [Liang 01].

- **Material properties:** determination of physical properties of media such as electrical, magnetic properties of the human tissue using different imaging techniques [Gabriel 96b, Gabriel 96a]. If the exact properties of some internal organ were known, then on doing a scan, i.e. Targeting that area with radiation or ultrasound, the resultant reflection/attenuation map would be known. That would be the forward problem. But it is nearly always the properties of the internal organ that we are trying to find, and ideally without invasive surgery. Thus we have to solve an inverse problem.
- **Boundary values/initial values:** identification of the proper boundary conditions and/or initial conditions of a system of interest is a growing topic in research. A common example is estimation of boundary properties in heat conduction problems [Yang 96, Yang 97]. Another example is determination of initial chemical composition for environmental monitoring purposes.
- **Image analysis:** extraction of meaningful information from images, mainly from digital images by means of digital image processing techniques. The applications of digital image analysis are continuously expanding through various areas of science and industry. Medical imaging is an important example of creating images of the human body (or parts of the body) for clinical purposes. A typical example is the problem of classifying regions of a satellite image of the earth's surface into regions of ocean, forest, agricultural land, etc.

From this short and incomplete list, it is open to view that the scope of inverse problem theory is of great extent and its applications can be found in many diverse fields. The objective of this thesis is to develop new models for selected diffusion systems and their inverse problems. In Chapter 2, we describe the classical approach, which is based on the

well-known Fick's law of diffusion, for source localization. Chapter 3 describes an example implementation of the diffusion-reaction model for the estimating regions of low diffusivity in the heart using MCG/ECG sensor arrays. Chapter 4 details the stochastic approach for source localization and compares it to the classical representation for low intensity sources. Chapter 5 extends the approach in Chapter 4 to account for boundaries and provides two examples for estimating the boundary properties using stochastic differential equations. In Chapter 6, we model the capillary exchange process using coupled Navier-Stokes and Fokker-Planck equations for the calculation of the absorption and transmission probabilities of a particle in the capillary network. Chapter 7 provides a conclusion on our work carried out, a view of anticipated future work and closing remarks. Overall consideration is also given how the contribution of this thesis aids in the broader areas of related research, and how it is believed further research will evolve and in which directions this may take.

Chapter 2

Estimation of the Properties of Diffusive Sources Using Classical Diffusion Model

2.1 Introduction

Signal processing techniques for detection, localization, and tracking of biological and chemical sources have attracted significant attention in recent years because of their importance in many applications such as drug delivery, environmental monitoring, and homeland security. The two most important concerns in all of these applications are accuracy in dealing with random effects of dispersion and real time implementation of the aforementioned algorithms (detection, localization, and tracking of diffusive sources). Consequently, these models should provide tools for reliable decision making once a biochemical event of interest has been detected and localized.

In literature, several inverse models [Nehorai 95, Jeremic 98, Porat 96, Jeremic 00] are proposed and can potentially be used in many of these applications. In [Kuang 06], a wire-

less sensor network (WSN) is proposed to estimate the plume source location using Maximum Likelihood Estimation (MLE). In [Sahyoun 09], Sahyoun and Djouadi proposed a non-linear least square (NLS) approach for the plume source localization. They also proposed a stochastic approximation technique for better treatment of the optimization problem. In [Matthes 05, Matthes 04], Matthes and Groll implemented technique of continuous concentration measurements from spatially distributed electronic noises to determine the location of a point source assuming that the emitted substance is transported by advection caused by a known homogeneous wind field and by isotropic diffusion. They proposed a two-step approach for solving the source localization problem. The basic idea was to split the problem into two main steps:

- For each sensor, determine the set of points on which the source can be located using only the available measurements from each sensor.
- Then, determine an estimation of the source location by estimating the intersections of all sets.

Briggs [Briggs 73], proposed a simplified approach to the calculation of ground level concentrations of effluents from small industrial and fuel burning installations. In [Egan 72], Bruce presented numerical grid-element model developed for the study of air pollution transport from urban area-type sources. This advection-diffusion model is especially useful for the estimation of air pollution concentrations under conditions of spatial and time varying emissions, velocities and diffusion rates. Niliot [Niliot 98], proposed a point heat source identification in homogeneous solids, using the boundary-element method, to identify the strength of line heat sources when their position is known. In addition, other approaches, [Nievergelt 98, Khapalov 94], are proposed that use the analytical solution of the

advection-diffusion equation. Based on these analytical solutions, NLS estimates are formulated for the estimation of the different source properties (position, rate, and start time). In [Baillet 01], Baillet and Mosher studied MEG/EEG source localization and the underlying models currently used in source estimation and described the various signal processing steps required to compute these sources. Ishida [Ishida 97] proposed a new method to remotely locate an odor source using a mobile robot with a gas sensor. Furthermore, the release rate of the odor and the range of its distribution can be obtained using this method. In [Ram 07], Ram and Veeravalli considered a network of spatially distributed sensors deployed to track the intensity of a diffusing source whose location is fixed, but unknown.

In this Chapter, we present the commonly used classical diffusion model and its application to the estimation of different source properties. This Chapter is organized as follows. In Section 2.2, we present the classical model of the advection-diffusion process. In Section 2.3, we present our measurement model and the corresponding estimators of the source properties. We first present our measurement model. Then we derive the maximum likelihood estimator of the unknown parameters in the presence of noise. In Section 2.4, we demonstrate the applicability of our results using numerical examples.

2.2 Classical Diffusion Model

Molecular diffusion, often called classical diffusion, is a net transport of molecules from a region of higher concentration to one of lower concentration by random molecular motion. The result of diffusion is a gradual mixing of material. Diffusion is of fundamental importance in many disciplines of physics, chemistry, and biology. Molecular diffusion is typically described mathematically using two Fick's laws. Fick's laws describe diffusion

and can be used to solve for the concentration field, flux, or the diffusion coefficient. They were derived by Adolf Fick in the year 1855.

Fick's first law relates the diffusive flux to the concentration field, by postulating that the flux goes from regions of high concentration to regions of low concentration, with a magnitude that is proportional to the concentration gradient (spatial derivative). In one three dimensional space, this is

$$J(\mathbf{r}, t) = -\mathcal{K}(c, \mathbf{r})\nabla c(\mathbf{r}, t) \quad (2.1)$$

where

J is the diffusive flux vector at point \mathbf{r} and time t .

\mathcal{K} is a matrix of diffusion coefficients, which depends on the temperature, viscosity of the fluid and the size of the particles according to the Stokes-Einstein relation.

$c(\mathbf{r}, t)$ is the diffusive substance concentration.

∇ is the gradient operator.

\mathbf{r} is the position vector.

Fick's second law predicts how diffusion causes the concentration field to change with time. It relates the flux gradient to the general principles of mass conservation and states that

" the change with time of conservative property inside a given volumetric element, is equal to the algebraic sum of the fluxes across all the volume boundaries."

$$\frac{\partial c(\mathbf{r}, t)}{\partial t} = -\nabla \cdot J \quad (2.2)$$

Combining (2.1) and (2.2) we get

$$\frac{\partial c(\mathbf{r}, t)}{\partial t} = \nabla \cdot (\mathcal{K}(c, \mathbf{r}) \nabla c(\mathbf{r}, t)) \quad (2.3)$$

This is the classical diffusion equation that describes density (concentration) fluctuations in a material undergoing diffusion, also known as the heat equation. Note that, (2.3) does not account for external forces such as drift. Convection forces act as an external flux and can be added to the flux term in the diffusion equation as follows

$$\frac{\partial c(\mathbf{r}, t)}{\partial t} = \nabla \cdot (\mathcal{K}(c, \mathbf{r}) \nabla c(\mathbf{r}, t) - \nu(\mathbf{r}, t) c(\mathbf{r}, t)) \quad (2.4)$$

where $\nu(\mathbf{r}, t)$ is the convection coefficient which is in general, a function of space and time.

In order to solve (2.4), it is necessary to define the diffusion matrix. For simplicity, we assume homogeneous, isotropic, and drift free medium. Under these assumptions, the diffusion matrix \mathcal{K} reduces to a diagonal matrix, having the form

$$\mathcal{K} = \begin{bmatrix} \kappa & 0 & 0 \\ 0 & \kappa & 0 \\ 0 & 0 & \kappa \end{bmatrix} \quad (2.5)$$

where κ is a constant that represents the diffusion coefficient.

After this simplification, the solution of (2.4), detailed in Appendix A, can be formulated by the fundamental solution, which leads to

$$c(\mathbf{r}, t) = \frac{c_0}{4\pi\mathcal{K}(t-t_0)} \exp\left\{-\frac{\|\mathbf{r} - (\mathbf{r}_0 + \nu(t-t_0))\|^2}{4\mathcal{K}(t-t_0)}\right\} \quad (2.6)$$

where c_0 is the initial concentration, \mathbf{r}_0 and t_0 are the initial position and time, respectively.

Also note that the above formula is the solution of the diffusion equation for a point source defined by $c(\mathbf{r}, t_0) = c_0 \delta(\mathbf{r} - \mathbf{r}_0, t - t_0)$, where $\delta(\cdot)$ is the well-known Dirac function. Note that, from (2.6), the isometric lines of the concentration are given by concentric circles.

2.3 Measurement Model

To model the measurements, we suppose a spatially distributed array of m sensors located at known positions \mathbf{r}_i , $i = 1, \dots, m$, and measure the concentration at times t_k , where $k = 1, \dots, p$ and p is the number of time samples. The measurement of each sensor is

$$y(\mathbf{r}_i, t_k) = c(\mathbf{r}_i, t_k) + e(\mathbf{r}_i, t_k) \quad (2.7)$$

where $e(\mathbf{r}_i, t_k)$ is the measurement noise.

We lump the measurement model (2.7) into a vector form, as follows

$$\mathbf{y}_k = \mathbf{a}_k(\theta)c_0 + \mathbf{e} \quad (2.8)$$

where \mathbf{y}_k is an (m)-dimensional measurement vector, $\mathbf{a}_k(\theta)$ is an m -dimensional source-to-sensor vector, θ is a vector of unknown source and medium parameters (i.e. \mathbf{r}_0 and t_0), c_0 is the source intensity, and \mathbf{e} is a vector of measurement noise.

The transfer vector $\mathbf{a}_k(\theta)$ is given by

$$\mathbf{a}_k(\theta) = [a_{1k}(\theta) \dots a_{mk}(\theta)]^T \quad (2.9)$$

where $a_{ik}(\theta)$ is a measurement scalar, that represents the concentration at location r_i and time t_k arising from a release of the diffusive source. For the point source model (2.6) and in drift free medium, this element is

$$a_{ik}(\mathbf{r}_0, t_0, \kappa) = \frac{1}{4\pi\kappa(t_k - t_0)} e^{-\|\mathbf{r}_i - \mathbf{r}_0\|^2 / 4\kappa(t_k - t_0)} \quad (2.10)$$

The measurement noise in (2.7) corresponds to sensor noise and possibly incorrect modeling (which includes modeling a stochastic process as a classical diffusion process). We will assume that it is spatially and temporally uncorrelated, and Gaussian distributed

with zero mean and unknown variance σ^2 . Note that, since the concentration has nonnegative value, the Gaussian becomes an assumption and becomes more valid as the signal to noise ratio (SNR) increases, i.e., higher source intensity. The corresponding joint distribution of the measurement vector \mathbf{y}_k is given by

$$\begin{aligned}\mathbf{y}_k &\sim \mathcal{N}(\mathbf{a}_k(\theta)c_0, \sigma^2 I_m) \\ p(y_{1k}, \dots, y_{mk}) &= \frac{1}{2\pi^{m/2}\sigma^m} e^{\{-\frac{\sigma^2}{2}(\mathbf{y}_k - c_0\mathbf{a}_k(\theta))^T(\mathbf{y}_k - c_0\mathbf{a}_k(\theta))\}}\end{aligned}\quad (2.11)$$

where I_m is a $m \times m$ identity matrix.

The corresponding likelihood function is

$$\mathcal{L} = \prod_{k=1}^p \frac{1}{2\pi^{m/2}\sigma^m} e^{\{-\frac{1}{2\sigma^2}(\mathbf{y}_k - c_0\mathbf{a}_k(\theta))^T(\mathbf{y}_k - c_0\mathbf{a}_k(\theta))\}}\quad (2.12)$$

And the log likelihood function will be

$$\log(\mathcal{L}) = \sum_{k=1}^p \left\{ -m\log(\sigma) - \frac{1}{2\sigma^2}(\mathbf{y}_k - c_0\mathbf{a}_k(\theta))^T(\mathbf{y}_k - c_0\mathbf{a}_k(\theta)) \right\}\quad (2.13)$$

The estimators of c_0 and \mathbf{r}_0 , derived in Appendix B, are given by

$$\bar{c}_0 = \frac{\sum_{k=1}^p \mathbf{y}_k^T \mathbf{a}_k(\theta)}{\sum_{k=1}^p \|\mathbf{a}_k(\theta)\|^2}\quad (2.14)$$

$$\bar{\mathbf{r}}_0 = \arg \min_{\mathbf{r}_0} \sum_{k=1}^p \frac{1}{(t_k - t_0)} \frac{(\mathbf{y}_k - c_0\mathbf{a}_k(\theta))^T \mathcal{R} \mathbf{a}_k(\theta)}{\|(\mathbf{y}_k - c_0\mathbf{a}_k(\theta))\|}\quad (2.15)$$

where \bar{c}_0 and $\bar{\mathbf{r}}_0$ are the estimator (classical) of the source intensity and initial location, respectively. The solution to (2.14) and (2.15) is carried by non-linear optimization tool in MATLAB.

The maximum likelihood estimate of σ^2 is

$$\bar{\sigma}^2 = \frac{1}{p} \sum_{k=1}^p (\mathbf{y}_k - \bar{c}_0\mathbf{a}_k(\theta))^T (\mathbf{y}_k - \bar{c}_0\mathbf{a}_k(\theta))\quad (2.16)$$

One of the goals of this model is to estimate the number of initial particles, which is a discrete quantity. On the other hand, our model is based on the measurement of the concentration, which is a continuous quantity, at different locations. In order to achieve the true measurement, we count the number of particles located in an arbitrary area ($\Delta_i = \Delta(\mathbf{r}_i)$), given by

$$\Delta_i = (x_{1i} - \Delta \leq x_{1i} \leq x_{1i} + \Delta, x_{2i} - \Delta \leq x_{2i} \leq x_{2i} + \Delta) \quad (2.17)$$

Then, the concentration can be related to the number of particles, as follows

$$c(\mathbf{r}_i, t_k) = \frac{n_{ik}}{\Delta_i} \quad (2.18)$$

where n_{ik} is the number of particles located in Δ_i at time t_k .

Moreover, we use the well known Itô diffusion model, will be explained in details in Chapter 4, to simulate the evolution of the particles in 3D domain.

2.4 Numerical Results

In this section, we present numerical examples to demonstrate the accuracy of using classical model-based estimator. We estimate n_0 and \mathbf{r}_0 for different source strengths, number of sensors, and time samples. In all the examples, we assume the diffusion coefficient to be known, as it can be estimated using different techniques such as, the one in [Kvarnstrom 05, Kvarnstrom 06]. Also, we define the mean square error (MSE) as

$$MSE_\alpha = \frac{\|\hat{\alpha}_0 - \alpha_0\|^2}{\|\alpha_0\|^2} \quad (2.19)$$

where α_0 is the true value (i.e. n_0 or \mathbf{r}_0) and $\hat{\alpha}_0$ is the corresponding MLE estimate.

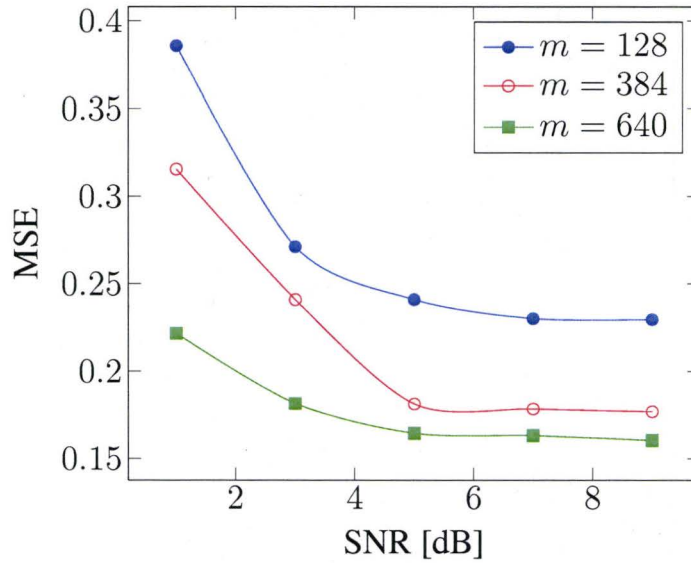
The estimation is carried for ($n_0 = 1000$) and ($k = 10$) with a square grid of equally distributed array of sensors covering an area of $80 * 10^{-6} \times 80 * 10^{-6} m^2$. The diffusivity is taken to be $4.29 * 10^{-13} m/s^2$ and the time step is 0.02 sec. We assume that the noise power is known, since, in principle, it can be estimated offline in the absence of the source. Also, the signal-to-noise ratio (SNR) is defined as $SNR = 10\log(\sum \|y_{ik}\|^2 / \bar{\sigma}^2)$

In Figures (2.1) and (2.2), we illustrate the error in estimating the source intensity and source location as a function of the SNR for 1000 particles. On the other hand, Figures (2.3) and (2.4) presents the estimation results for 50000 particles. Observe that, the estimation error, in the case of low intensity source (1000 particles), is unsatisfactory and decreases significantly for the high source intensity case (50000 particles) reaching a satisfactory level.

2.5 Conclusions

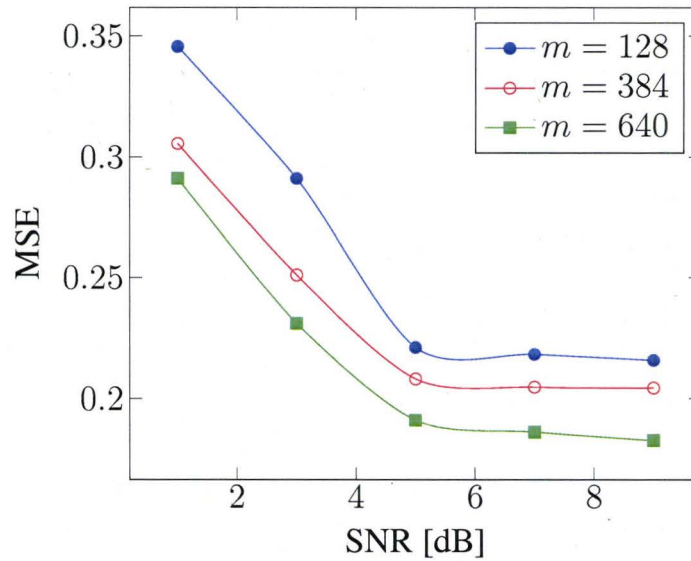
In this chapter, we address the problem of estimating the properties of diffusive sources using classical model of diffusion, i.e. Fick's law. The main advantage of this approach lies in the fact that it is computationally efficient and simple in implantation. On the other hand, it fails to provide satisfactory estimates when applied to low intensity sources since it does not account for the random effects in the motion of particles. In Chapter 4, we will address the problem of estimating the source properties using stochastic differential equations as an alternative method when dealing with low intensity sources.

Localization Mean Square Error - $n_0 - k = 15$



(a) MSE of estimating $n_0 - r_0$ is known.

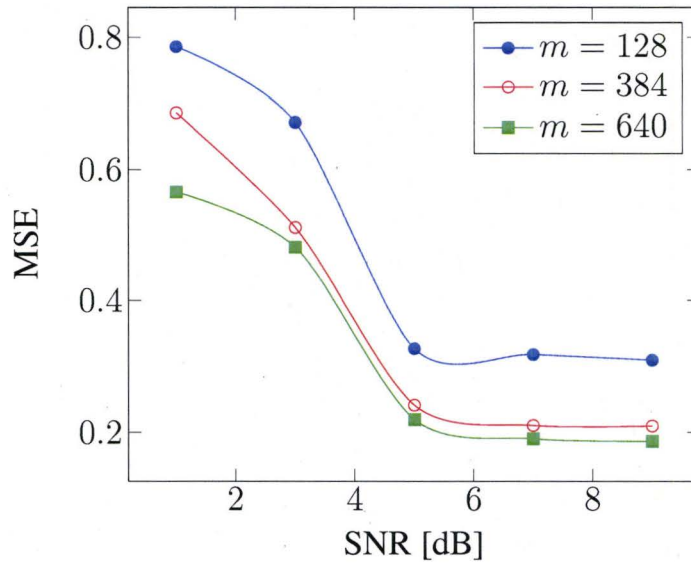
Localization Mean Square Error - $r_0 - k = 15$



(b) MSE of estimating $r_0 - n_0$ is known.

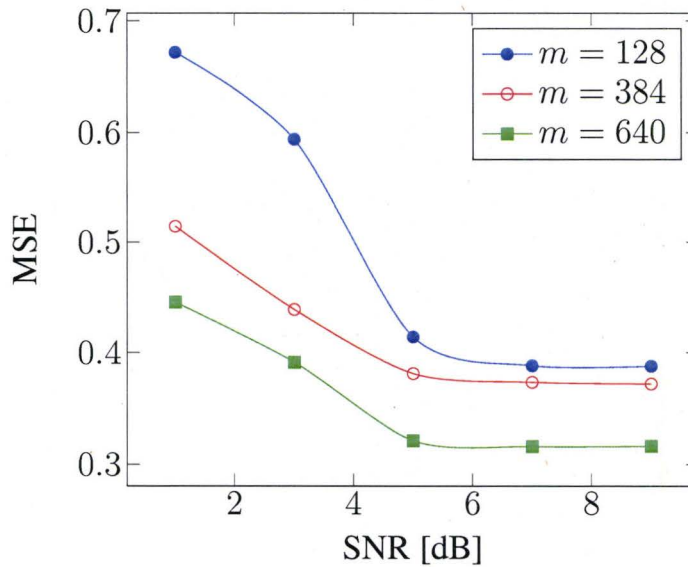
Figure 2.1: Mean square error for estimating n_0 and r_0 as a function of SNR and the number of sensors for 1000 particles. a) MSE for estimating $n_0 - r_0$ is known. b) MSE for estimating $r_0 - n_0$ is known.

Localization Mean Square Error - $n_0 - k = 15$



(a) MSE of estimating $n_0 - r_0$ is unknown.

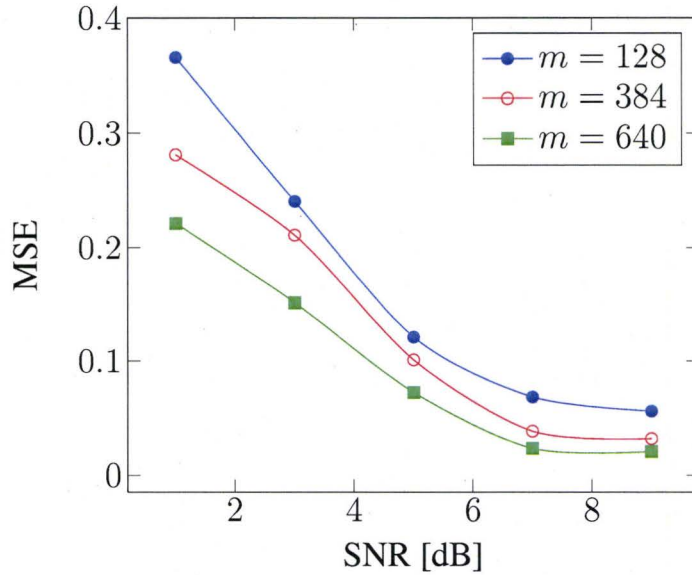
Localization Mean Square Error - $r_0 - k = 15$



(b) MSE of estimating $r_0 - n_0$ is unknown.

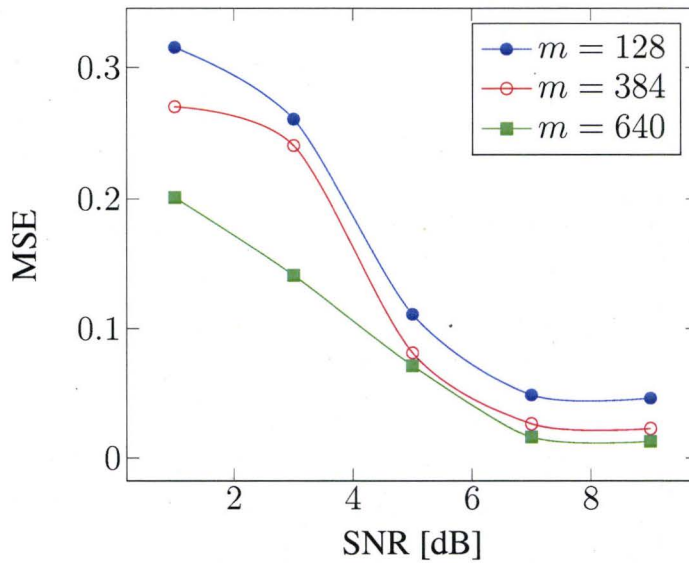
Figure 2.2: Mean square error for estimating n_0 and r_0 as a function of SNR and the number of sensors for 1000 particles. a) MSE for estimating $n_0 - r_0$ is unknown. b) MSE for estimating $r_0 - n_0$ is unknown.

Localization Mean Square Error - $n_0 - k = 15$



(a) MSE of estimating $n_0 - r_0$ is known.

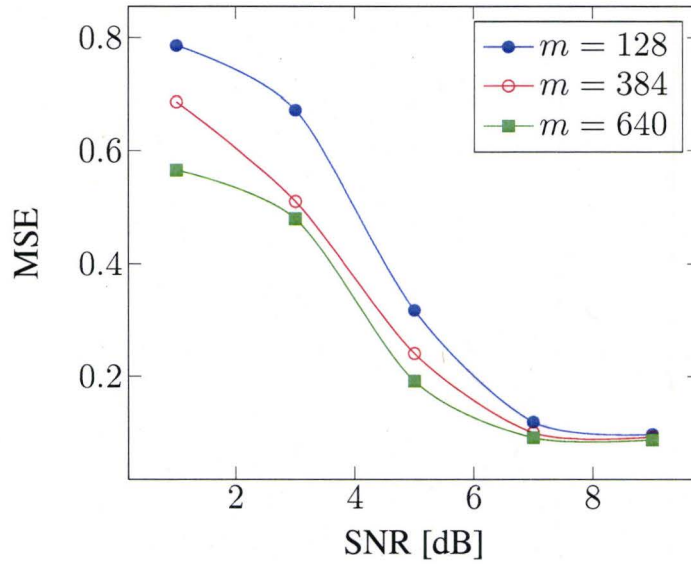
Localization Mean Square Error - $r_0 - k = 15$



(b) MSE of estimating $r_0 - n_0$ is known.

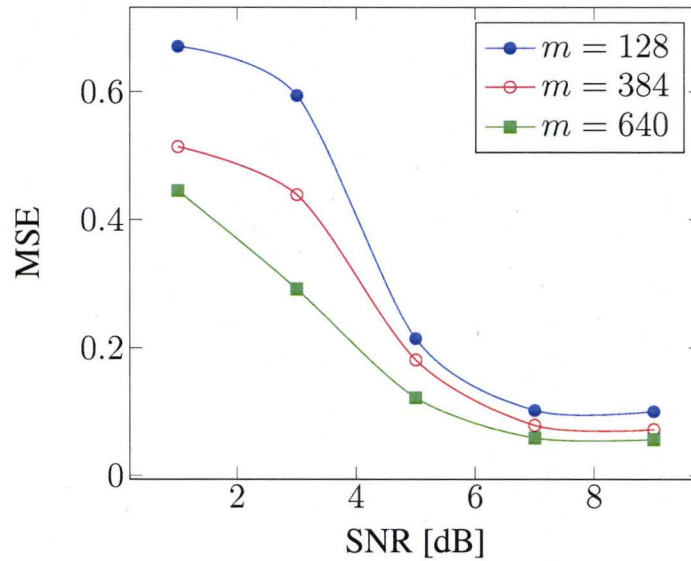
Figure 2.3: Mean square error for estimating n_0 and r_0 as a function of SNR and the number of sensors for 1000 particles. a) MSE for estimating $n_0 - r_0$ is known. b) MSE for estimating $r_0 - n_0$ is known.

Localization Mean Square Error - $n_0 - k = 15$



(a) MSE of estimating $n_0 - r_0$ is unknown.

Localization Mean Square Error - $r_0 - k = 15$



(b) MSE of estimating $r_0 - n_0$ is unknown.

Figure 2.4: Mean square error for estimating n_0 and r_0 as a function of SNR and the number of sensors for 1000 particles. a) MSE for estimating $n_0 - r_0$ is unknown. b) MSE for estimating $r_0 - n_0$ is unknown.

Chapter 3

An Inverse Model for Localization of Low-diffusivity Regions in the Heart Using ECG/MCG Sensor Arrays

3.1 Introduction

The phases of myocardial action potentials and processes of myocardial depolarization and repolarization are well studied and described in most handbooks of electrophysiology and electrocardiography [Gulrajani 98, Malmivuo 95]. The underlying processes controlling the (re)polarization in the cardiac activation can be described, on a molecular level, as diffusion of ions through various channels (Na, K, etc.) giving a rise to ionic current which in turn creates electromagnetic field on the torso surface which can be externally measured. Modeling the cardiac activation on a cellular level [Gulrajani 98] has been a subject of considerable research interest resulting in numerous models related to membrane poten-

tial (e.g., Hodgkin-Huxley model). However, these models are mainly suitable for forward modeling in which the cardiac activation is simulated using a priori knowledge of various parameters. Complimentary to this approach is inverse modeling in which information on cardiac activation (and some physiological parameters) is deduced from ECG/MCG measurements.

One of the most important parameters controlling the activation wavefront propagation is the diffusivity (i.e., mobility of ions). Namely, significant loss of ionic mobility can cause occurrence of irregular activation patterns and lead to various pathological conditions such as arrhythmia, early after-depolarization, etc. From a physiological point of view, these changes usually occur due to loss of conductivity of a particular region of the heart. As a result, the diffusivity in this region becomes very small preventing the propagation of the activation wavefront and causing the aforementioned irregular patterns. Therefore, any algorithm capable of detecting these anomalies can potentially be useful to predict the onset of these cardiac physiopathologies.

In this chapter, we propose a new activation model based on the diffusion equation. Although the FitzHugh-Nagumo model is based on the diffusion equation its applicability to inverse approach and real data is limited because of its isotropic and homogeneous nature. In Section 3.2, we develop cardiac activation model based on the reaction-diffusion equation with nonhomogeneous and anisotropic diffusion tensor. Such a model can be used for detecting different physiological conditions such as conductivity anomalies, which can predate onset of various pathological conditions such as cardiac arrhythmia, early after-depolarization, etc. In Sections 3.3 and 3.4, we derive the statistical and measurements

model using Geselowitz equations corresponding to our diffusion based source. Using these models we derive the generalized least squares (GLS) estimator for localizing conductivity anomalies/disorders. In Section 3.5, we demonstrate the applicability of our results using numerical simulations and in Section 3.6 we present conclusions.

3.2 Physical Model

During the spread of activation in the heart, the most significant bioelectric source is the large potential difference that exists across the moving wavefront that divides active (depolarized) from resting tissue. It has been proposed that the cardiac excitation can be modeled using reaction diffusion systems i.e., a set of nonlinear partial differential equations [Panfilov 97]

$$\frac{\partial u_i}{\partial t} = f_i(u) + \nabla \cdot (D_i \nabla u_i) \quad i = 1, \dots, n \quad (3.1)$$

where $u = [u_1, \dots, u_n]^T$ is the state variable vector, f_i are excitations, and D_i diffusion tensors.

Although the above models can be used to model the propagation even down to a cellular level, in order to develop an inverse model a simplified approach similar to [Fitzhugh 61, Rogers 94] is needed. Therefore, we propose a reaction diffusion model consisting of two state variables but with spatially dependent diffusivity tensor

$$\begin{aligned} \frac{\partial u_1(\mathbf{r}, t)}{\partial t} &= \nabla \cdot (D(\mathbf{r}) \nabla u_1(\mathbf{r}, t)) + g^T(u(\mathbf{r}, t)) A_1 g(u(\mathbf{r}, t)) \\ \frac{\partial u_2(\mathbf{r}, t)}{\partial t} &= (u^T(\mathbf{r}, t)) A_2 (u(\mathbf{r}, t)) \\ g(u(\mathbf{r}, t)) &= [u_1^2(\mathbf{r}, t), u_1(\mathbf{r}, t), u_2(\mathbf{r}, t), 1]^T \end{aligned} \quad (3.2)$$

where u_1 is the activation potential and u_2 is the resting potential. $g()$ is an arbitrary polynomial and A_1 and A_2 are arbitrary matrices. $g()$, A_1 and A_2 are chosen such that to control the activation wave shape.

The above model is the generalization of the existing models from at least two standpoints: a) by allowing the diffusivity matrix to be spatially dependent we can test for the presence of arbitrarily shaped anomalies, and b) by adding higher-order polynomial components we allow for wider range of dynamic behavior in the cardiac excitation. Note that in order to apply the above model to the realistic geometry we need to define boundary conditions. In our case we impose $\partial u_1 / \partial n = 0$ on the epicardial surface of the heart. As for initial conditions, we define the active potential at time $t = 0$ as $u_1(\mathbf{r}, 0) = u_0 \delta(\mathbf{r} - \mathbf{r}_0)$ where $\delta()$ is a Dirac delta function and \mathbf{r}_0 is the activation point in the myocardium. The initial condition for the inhibition (u_2) is set to zero.

To compute the electro-magnetic field on the torso surface we utilize the Geselowitz equations [Geselowitz 70] that compute the potential $V(\mathbf{r}, t)$ and magnetic field $B(\mathbf{r}, t)$ at a location \mathbf{r} on the torso surface at a time t from a given primary current distribution $J(\mathbf{r}_0, t) = \nabla u_1(\mathbf{r}, t)$ within the heart. We use a piecewise homogeneous torso model consisting of the following surfaces: the outer torso, the inner torso, and the heart. Therefore, we model the torso as a volume G of $M = 3$ homogeneous layers separated by closed surfaces S_i , $i = 1, \dots, M$. Let σ_i^- and σ_i^+ be the conductivities of the layers inside and outside S_i respectively. We will denote by G_i the regions of different conductivities, and by G_{M+1} the region outside the torso, which behaves as an insulator i.e., $\sigma_{M+1}^- = \sigma_M^+ = 0$

It has been shown that in the case of a piecewise homogeneous torso model and using

quasi-static assumption the magnetic field at a location \mathbf{r} and time t is given by [Gulrajani 98] and [Malmivuo 95]

$$\begin{aligned}
\mathbf{B}(\mathbf{r}, t) &= \mathbf{B}_0(\mathbf{r}, t) + \frac{\mu_0}{4\pi} \sum_{i=1}^M (\sigma_i^- - \sigma_i^+) \cdot \\
&\quad \cdot \int_{S_i} \phi(\mathbf{r}', t) \frac{(\mathbf{r} - \mathbf{r}')}{\|\mathbf{r} - \mathbf{r}'\|^3} \times dS(\mathbf{r}') \\
\mathbf{B}_0(\mathbf{r}, t) &= \frac{\mu_0}{4\pi} \int_G \frac{\mathbf{J}(\mathbf{r}', t) \times (\mathbf{r} - \mathbf{r}')}{\|\mathbf{r} - \mathbf{r}'\|^3} d^3r', \tag{3.3}
\end{aligned}$$

where μ_0 is the magnetic permeability of the vacuum and σ_i^- and σ_i^+ be the conductivities of the layers inside and outside S_i respectively.

Similarly, the potential $V(\mathbf{r}, t)$ is given by [Gulrajani 98]

$$\begin{aligned}
\frac{\sigma_k^- + \sigma_k^+}{2} V(\mathbf{r}, t) &= V_0(\mathbf{r})(\sigma_i^- - \sigma_i^+) + \\
&+ \frac{1}{4\pi} \sum_{i=1}^M (\sigma_i^- - \sigma_i^+) \int_{S_i} V(\mathbf{r}', t) \frac{(\mathbf{r} - \mathbf{r}')}{\|\mathbf{r} - \mathbf{r}'\|^3} \cdot dS(\mathbf{r}'), \\
V_0(\mathbf{r}, t) &= \frac{1}{4\pi} \int_G \frac{\mathbf{J}(\mathbf{r}', t) \cdot (\mathbf{r} - \mathbf{r}')}{\|\mathbf{r} - \mathbf{r}'\|^3} d^3r', \tag{3.4}
\end{aligned}$$

where we k is chosen so that $\mathbf{r} \in G_k$.

3.3 Measurement Model and Statistical Model

In this section we introduce our parametric description of the diffusion anomaly and measurement noise signals. To simplify the approach we assume that the anomaly region can be modeled with an ellipsoid i.e., the region \mathcal{R} of anomaly is given by

$$\mathcal{R} = \{\mathbf{r} : (\mathbf{r} - \mathbf{r}_a)^T F(a, b, c, \psi, \phi)^{-1} (\mathbf{r} - \mathbf{r}_a) \leq 1\}$$

where

$$F = T(\phi, \psi) \begin{bmatrix} a^2 & 0 & 0 \\ 0 & b^2 & 0 \\ 0 & 0 & c^2 \end{bmatrix} T^T(\phi, \psi)$$

where a, b, c are the axes of anomaly ellipsoid, \mathbf{r}_a is the center, and ϕ and ψ are the orientation parameters (in 3D). The matrix $T(\phi, \psi)$ is the rotation matrix given by

$$T(\phi, \psi) = \begin{bmatrix} \cos\phi & \sin\phi & 0 \\ -\sin\phi & \cos\phi & 0 \\ 0 & 0 & 1 \end{bmatrix} \cdot \begin{bmatrix} \cos\psi & 0 & \sin\psi \\ 0 & 1 & 0 \\ -\sin\psi & 0 & \cos\psi \end{bmatrix} \quad (3.5)$$

The diffusion tensor is then

$$D(\mathbf{r}) = \begin{cases} 0 & \mathbf{r} \in \mathcal{R} \\ D & \text{otherwise} \end{cases} \quad (3.6)$$

In the remainder of the myocardium tissue we assume homogeneous but possibly anisotropic diffusion tensor D .

Next, we assume that a bimodal array of n_B MCG and n_E ECG sensors is used for the measurements. Let $n = n_B + n_E$, we assume that the sensors are located at $\rho_j, j = 1, \dots, n$, and that time samples are taken at uniformly spaced time points $t_k, k = 1, \dots, n_s$. In addition, we assume that data acquisition is repeated n_c times during several heart cycles in order to improve the signal-to-noise (SNR) ratio. Then, the n_s -dimensional measurement vector of this array obtained at time t_k in the l^{th} cycle is

$$y_{lk} = f(\theta, t_k) + e_l(t_k) \quad (3.7)$$

where $y_{lk} = [y_B^T(t_k), y_E^T(t_k)]^T$, θ is the collection of all the parameters $(a, b, c, r_0, \phi, \psi, u_0, D, A_1, A_2)$, $f(\theta, t_k)$ is the vector solution computed using finite elements, and $e_l(t_k) = [e_B^T(t_k), e_E^T(t_k)]^T$ is additive noise. In the remainder of this chapter, we omit the subscript l whenever it is obvious that the samples belong to the same heart cycle. The subscripts B and E correspond to magnetic and electric components of the measurement vector (noise), respectively. We further assume that both magnetic and electric components of the noise are zero-mean Gaussian, uncorrelated in space and time with variances, σ_B^2 and σ_E^2 , respectively.

3.4 Parameter Estimation

We first start by splitting the unknown parameters θ into two groups: a) the unknown activation parameters $\theta_0 = [u_0, r_a]^T$, and b) the unknown anomaly parameters $\theta_a = [a, b, c, r_0, \phi, \psi]^T$. For simplicity, in the remainder of the paper we assume that the heart parameters

$$\theta_h = [\text{vec}(D), \text{vec}(A_1), \text{vec}(A_2)]^T \quad (3.8)$$

where vec is the vector operator, are known. Note that, some in vitro studies [Sachse 04] suggest that these parameters do not vary significantly between different subjects and thus can be easily estimated using data gathered from human subjects without any anomalies. Complicating the matter is the fact that the diffusion tensor in general is inhomogeneous. Namely, the ionic diffusion process is much larger along the myocardium fiber than across different fibers. Since the fiber orientations change in space, the diffusion tensor should be spatially dependent. However, these changes are smooth in nature and can be easily modeled using a set of a priori known basis functions. Furthermore, information about fiber

orientation can be easily obtained using cardiac diffusion MRI [Zhukov 03].

To compute estimates $\hat{\theta}_0$ and $\hat{\theta}_a$, we use the generalized least squares (GLS) estimator which minimizes the following cost function [Vonesh 97]

$$\begin{aligned}
c(\theta_0, \theta_a, \hat{\sigma}_E^2, \hat{\sigma}_B^2) &= \sum_{k=1}^{n_a} \sum_{l=1}^q \frac{1}{\hat{\sigma}_E^2} \|y_{kl}^E - f^E(\theta_0, \theta_a, t_k)\|^2 + \frac{1}{\hat{\sigma}_B^2} \|y_{kl}^B - f^B(\theta_0, \theta_a, t_k)\|^2 \\
\hat{\sigma}_E^2 &= \frac{1}{n_E n_s q} \sum_{k=1}^{n_a} \sum_{l=1}^q \|y_{kl}^E - f^E(\theta_0, \theta_a, t_k)\|^2 \\
\hat{\sigma}_B^2 &= \frac{1}{n_B n_s q} \sum_{k=1}^{n_a} \sum_{l=1}^q \|y_{kl}^B - f^B(\theta_0, \theta_a, t_k)\|^2
\end{aligned} \tag{3.9}$$

where we use superscripts E and B to denote electrical and magnetic, components of the measured field and solution vector.

The above GLS estimator is more efficient than the ordinary least squares estimator due to each contribution to the objective function being normalized to the same unit variance (i.e., those measurements with less variation are given greater weight). The actual optimization can be done using any of the well known algorithms such as Davidson-Fletcher-Powell or Broyden-Fletcher-Goldfarb-Shanno. To further simplify the computational complexity, we propose to estimate θ_0 assuming that $a = b = c = 0$, i.e., the diffusivity of the heart is homogeneous and using ordinary least squares. Then we can use this estimate as the initial guess for GLS estimation algorithm.

3.5 Numerical Examples

We now describe numerical study that demonstrates the applicability of the proposed algorithms. We used MRI extracted mesh of the human torso and the ventricular heart that was kindly provided to us by Prof. McLeod, Utah University. In our model the Purkinje network was approximated by a set of nodes near the apex. To achieve higher precision we remeshed the original data into a new mesh (see Figure 3.1). The volumetric mesh was created using 15902 elements with 20830 degrees of freedom for the torso (electromagnetic) model and 1856 elements and 6190 degrees of freedom for the heart (diffusion) model. The computational model was developed using a general partial differential (PDE) toolbox in COMSOL software.

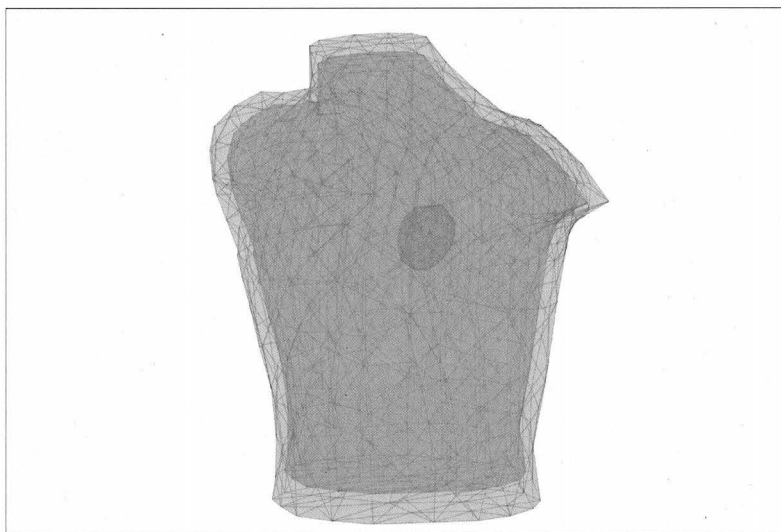
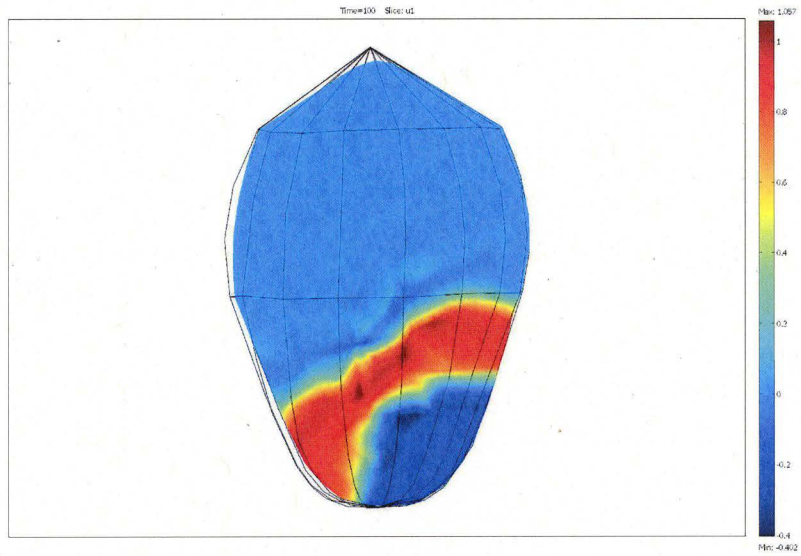


Figure 3.1: Mesh geometry used for numerical study.

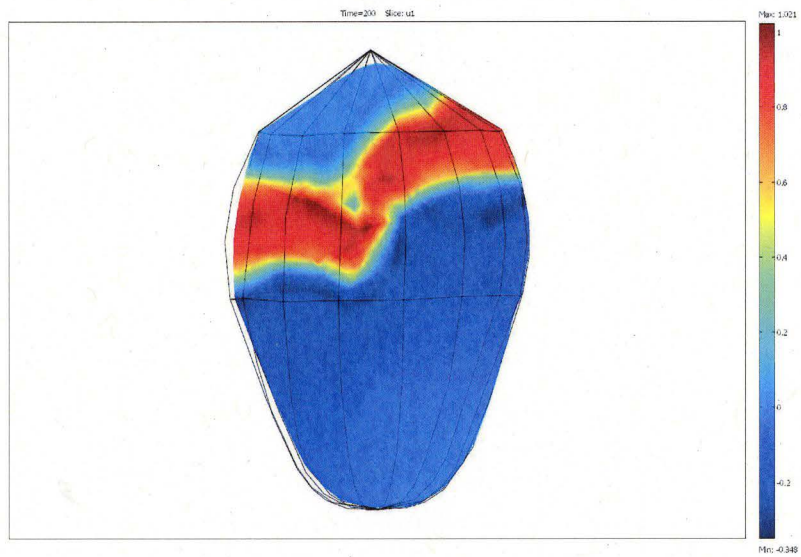
The torso conductivity was set to $5\mu S$ respectively as in [Malmivuo 95]. To simplify

the complexity of the numerical study we simulated the anomaly using $a = b = 2\text{cm}$, $c = 0.5\text{ cm}$, and $\phi = \psi = 0$ with the apex of the heart cycle located on the top. The diffusion tensor was set to be isotropic with diagonal elements equal to $40\text{cm}^3/\text{s}$. The diffusivity was chosen according to [Gulrajani 98] so that the activation wavefront propagates the whole heart in 0.2s . The control matrices A_1 and A_2 were chosen following the approach of [Rogers 94]. The heart rate was set to 72 beats per minute. We assume that the measurements are obtained using 64-channel ECG/MCG sensor array with sensors locations uniformly distributed on the chest. To evaluate the localization accuracy we use $MSE_{r_0} = \|\mathbf{r}_0 - \hat{\mathbf{r}}_0\|^2 / \|\mathbf{r}_0\|^2$, $MSE_a = \|a - \hat{a}\|^2 / \|a\|^2$, and $MSE_c = \|c - \hat{c}\|^2 / \|c\|^2$.

Figure 3.2 illustrates the activation wavefront in myocardium at approximately $t = 2T/3$ after the activation where T is the time period of ventricular polarization/depolarization cycle. In Figure 3.3 we illustrate the body surface map of the electric potential on the torso surface. Similarly, Figure 3.4 illustrates the magnetic field map at the same time. In Figure 3.5, we illustrate the mean square error of the axis parameters with $c = a = 10$ and $b = a$. The location of an anomaly was arbitrarily set to $r_0 = (0, 0.5, 0.75)$. As expected, due to the wavefront orientation as well as difference in size, the estimation accuracy of the cross-sectional axis parameters is much smaller. In Figure 3.6, we illustrate the localization accuracy i.e., MSE of r_0 as a function of noise. The SNR was defined as $\text{SNR} = 10\log(\sum \|y_{lk}\|^2 / \sigma_E^2 + \sigma_B^2)$.

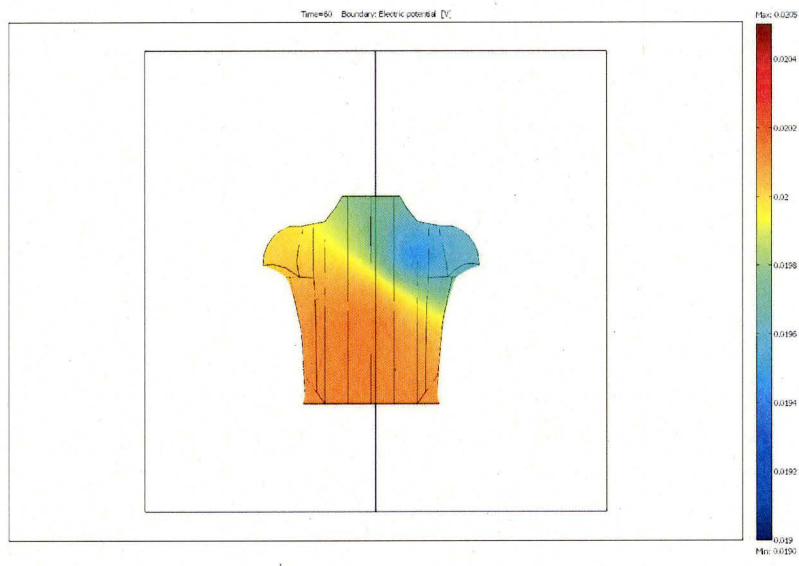


(a) $t = T/3$.

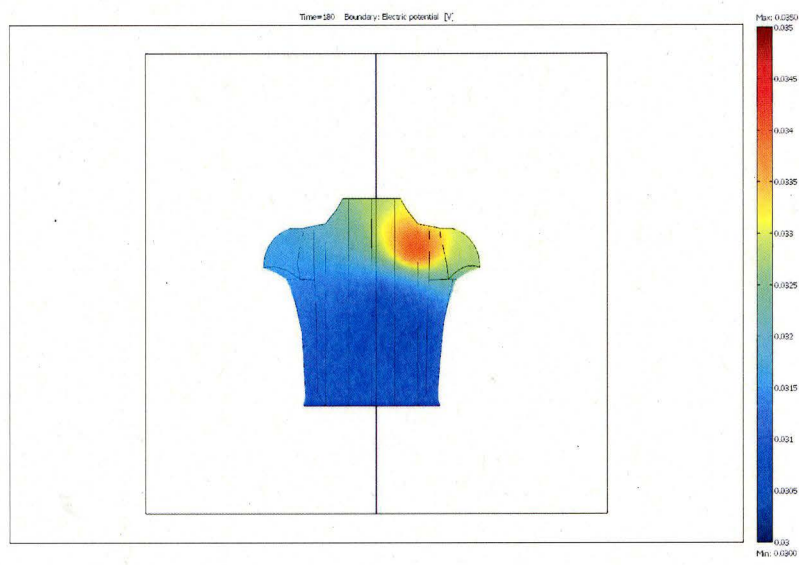


(b) $t = 2T/3$.

Figure 3.2: Activation wavefront, at a) $t = T/3$, b) $t = 2T/3$.

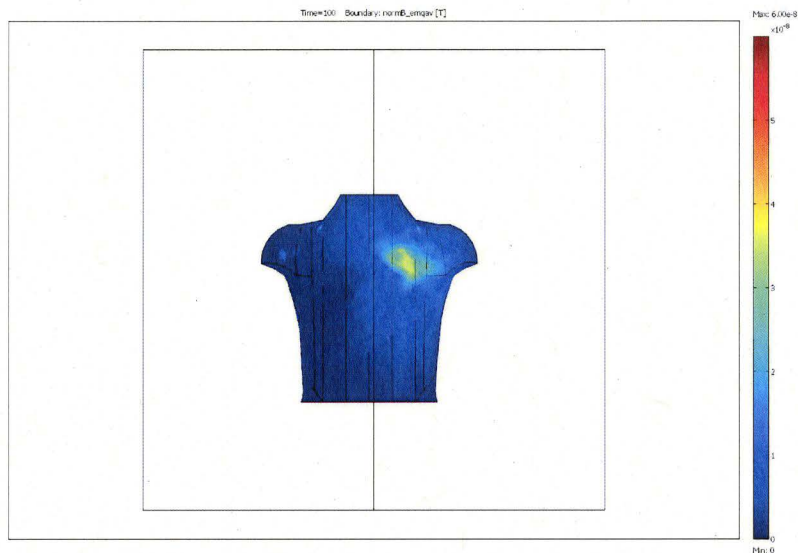


(a) $t = T/3$.

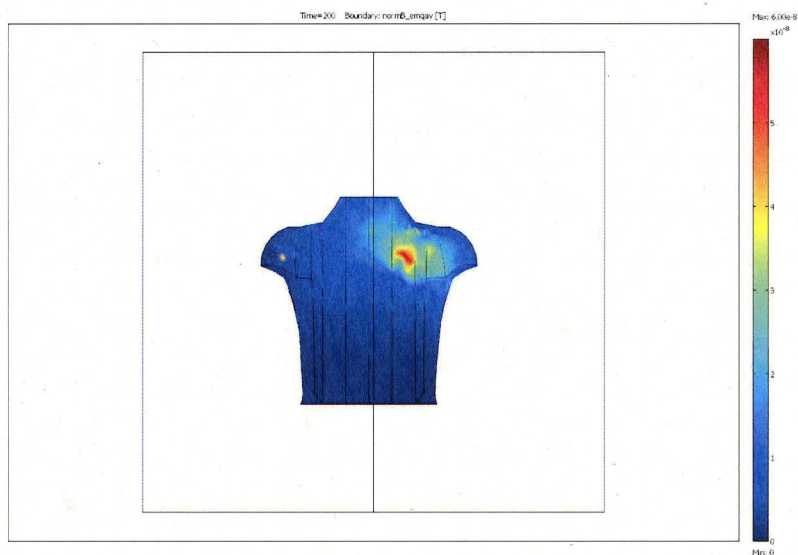


(b) $t = 2T/3$.

Figure 3.3: Body surface map of electric potential, at a) $t = T/3$, b) $t = 2T/3$.



(a) $t = T/3$.



(b) $t = 2T/3$.

Figure 3.4: Body surface map of magnetic field, at a) $t = T/3$, b) $t = 2T/3$.

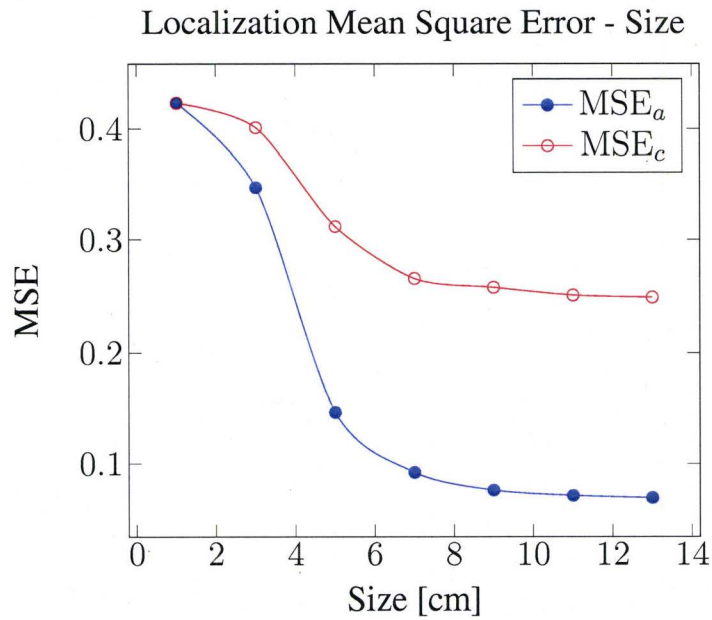


Figure 3.5: Mean square error for estimating the size of the anomaly.

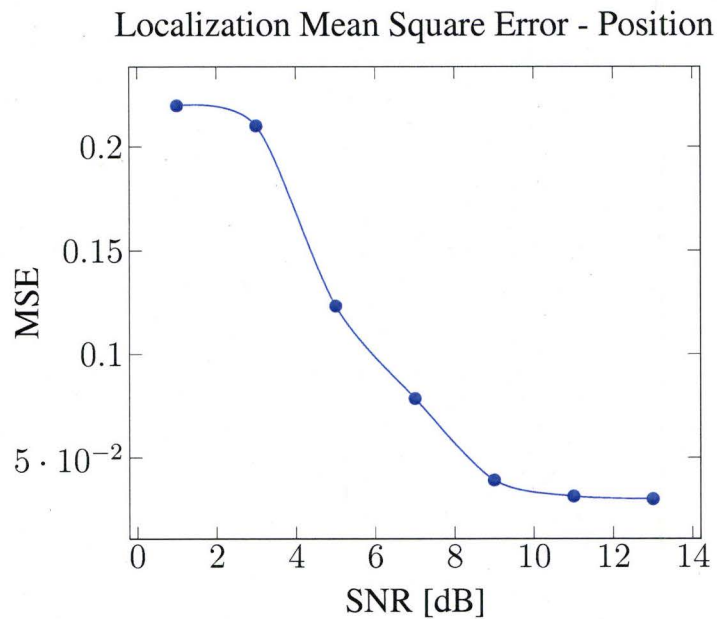


Figure 3.6: Mean square error for estimating the location of the anomaly.

3.6 Conclusions

In this chapter we addressed the problem of localizing the diffusivity disorder in the myocardium using ECG/MCG sensor arrays. To model the cardiac activation we considered an inhomogeneous reaction-diffusion model in a real human torso. To model the loss, we used a parametric model for an oblate spheroid and set its conductivity to zero. We assumed that the remainder of the myocardium tissue was homogeneous. The proposed algorithm can be easily extended to account for an arbitrary spatial variation in the diffusivity tensor using a set of *a priori* known basis functions. In addition, the parametric shape of the anomaly can be extended to model an arbitrary region using a three-dimensional spatial Fourier transform. An effort should be made to examine the sensitivity of the proposed algorithms to the size of diffusivity difference between “regular” tissue and anomaly as well as the number of the unknown parameters needed to model arbitrary shapes.

3.7 Publications

- A. Atalla and A. Jeremic, “*An Inverse Model for Localization of Low-diffusivity Regions in the Heart Using ECG/MCG Sensor Arrays*”, PIERS, pp 630-635, 2008.
- A. Atalla and A. Jeremic, “*An Inverse Model for Localization of Low-diffusivity Regions in the Heart Using ECG/MCG Sensor Arrays*”, BIOSIGNALS 2008, Volume 2, pp 508-51.

Chapter 4

Estimation of the Properties of Diffusive Sources Using Stochastic Differential Equations

4.1 Introduction

Signal processing techniques for detection, localization, and tracking of biological and chemical sources have attracted significant attention in recent years because of their importance in many applications such as drug delivery, environmental monitoring, and homeland security. The two most important concerns in all of these applications are accuracy in dealing with random effects of dispersion and real time implementation of the aforementioned algorithms (detection, localization, and tracking of diffusive sources). Consequently, these models should provide tools for reliable decision making once a biochemical event of interest has been detected and localized. Several inverse models [Jeremic 98, Jeremic 00,

Ortner 07] were proposed that can potentially be used in many of these applications. Most of the previous models were based on the second law of diffusion, the so called classical model. Although computationally efficient, these models can not account for the stochastic nature of diffusion in fluids (e.g. Brownian motion). It has been observed that the patterns of drug dispersion in human body organs exhibit certain irregularities (discontinuities) which can not be modeled with Fick's law of diffusion even using anisotropic and nonhomogeneous diffusivity. Ortner and Nehorai [Ortner 07] developed an inverse model based on Itô diffusion and corresponding Feynman-Kac's formula . However, this approach requires computationally intensive Monte Carlo simulations in order to obtain the probability density function required for maximum likelihood estimation. In literature, many attempts for the estimation of the properties of stochastic diffusion processes are presented. In [Pedersen 95], Pedersen proposed a new approach to maximum likelihood estimation (MLE) for stochastic differential equations based on discrete observations when the likelihood function is unknown. A sequence of approximations to the likelihood function is derived, and convergence results are proven. In [Jiang 97], Jiang and Knight suggested a nonparametric approach to the estimation of diffusion processes with an application to a short-term interest rate model. In [di Miscia 04], a Monte Carlo simulation is performed to investigate the finite sample properties of a nonparametric estimator, based on discretely sampled observations of continuous-time Itô diffusion process. Modeling the dynamics of short-term interest rates, in Itô diffusion process, can also be found in [Di Miscia , Sørensen 02, Arapis 06, Mancini 06, Sam 08].

In this chapter, we present a new framework for localization of diffusive sources using stochastic differential models. Namely, the most challenging part of modeling the dispersion of fluids lies in the statistical nature of particle motion. To properly account for

random effects one has to apply computationally intensive Brownian motion inverse algorithms (e.g. Feynman-Kac). Most of these algorithms are based on simulation propagation paths of numerous particles (i.e. Monte Carlo simulations). In our approach, we account for the stochastic nature of dispersion by utilizing well-known Fokker-Planck equation, which models the probability distribution of particle position when moving in a fluid environment. The main advantage of this approach over classical diffusion theory lies in the fact that it accounts for random fluctuations in dispersion patterns which may be of great importance if the source intensity (number of particles) is small. This is of particular interest in scenarios such as biochemical attacks, drug delivery, pollutant leakage, etc. On the other hand, it is computationally much more efficient than a Monte Carlo simulator, since it provides analytical expressions for probability density function of particle counts. Using the proposed model we derive the corresponding maximum likelihood estimator of source location, intensity, and release time in the presence of noise since the chemical sensors measuring the concentration of interest may be inaccurate.

This chapter is organized as follows. In Section 4.2, we present the stochastic process modeling the dispersion and corresponding Fokker-Planck equation and illustrate the main differences compared to classical diffusion theory. In Section 4.3, we first present our measurement model, then we derive the corresponding joint probability mass function of particle counts at sensors located at known (but arbitrary) locations and times. Using this result, we derive the maximum likelihood estimator of the unknown parameters in the presence of noise. In Section 4.4, we demonstrate the applicability of our results using numerical examples.

4.2 Physical Model

Let us assume that at arbitrary time t_0 we introduce n_0 (or equivalently concentration c_0) particles in an open domain environment at location r_0 . When the number of particles is large macroscopic approach corresponding to the Fick's law of diffusion is adequate for modeling the transport phenomena. However, to model the motion of the particles when their number is small a microscopic approach corresponding to stochastic differential equations (SDE) is required.

The diffusion process for the transport of particle in an open environment is given by the $it\tilde{o}$ stochastic differential equation:

$$dX_t = \boldsymbol{\mu}(X_t, t)dt + \boldsymbol{\sigma}(X_t, t)dW_t \quad (4.1)$$

where X_t , in R^3 , is the location and W_t is a standard Wiener process in R^3 .

The function $\boldsymbol{\mu}(X_t, t)$ is referred to as the drift coefficient while $\boldsymbol{\sigma}()$ is called the diffusion coefficient such that in a small time interval of length dt the stochastic process X_t changes its value by an amount that is normally distributed with expectation $\boldsymbol{\mu}(X_t, t)dt$ and variance $\boldsymbol{\sigma}^2(X_t, t)dt$ and is independent of the past behavior of the process.

The solution for (4.1) is carried out by means of stochastic integration. For three-dimensional isotropic space, i.e., $\boldsymbol{\sigma}$ is a diagonal matrix, (4.1) can be decomposed into three separate equations, given by

$$dX_{it} = \mu_i(t)dt + \sigma_i(t)dW_{it} \quad i = 1, \dots, 3 \quad (4.2)$$

For a homogeneous drift-free medium (i.e. $\boldsymbol{\mu} = 0$), where $\boldsymbol{\sigma}$ is a constant, the trajectories of $X_i(t)$, $i = 1, \dots, 3$ become

$$X_i(t) = X_{i0} + \sigma_i W_i(t - t_0) \quad i = 1, \dots, 3 \quad (4.3)$$

where $\mathbf{X}_0 = [X_{10} \ X_{20} \ X_{30}]^T$ is the initial position vector of the particle and $W_i(t) \sim \mathcal{N}(0, t - t_0)$.

Assuming three-dimensional environment $\mathbf{r} = (x_1, x_2, x_3)$, we compute the probability density function, $f(\mathbf{r}, t)$, of one particle occupying space around \mathbf{r} at time t using the Fokker-Planck equation [Risken 89]

$$\frac{\partial f(\mathbf{r}, t)}{\partial t} = \left[- \sum_{i=1}^3 \frac{\partial}{\partial x_i} D_i^1(\mathbf{r}) + \sum_{i=1}^3 \sum_{j=1}^3 \frac{\partial^2}{\partial x_i \partial x_j} D_{ij}^2(\mathbf{r}) \right] f(\mathbf{r}, t) \quad (4.4)$$

where partial derivatives apply the multiplication of D and $f(\mathbf{r}, t)$, D^1 is the drift vector and D^2 is the diffusion tensor given by

$$\begin{aligned} D_i^1 &= \mu \\ D_{ij}^2 &= \frac{1}{2} \sum_l \sigma_{il} \sigma_{lj}^T \end{aligned} \quad (4.5)$$

For simplicity of notation, we omitted the dependency of σ and μ on space and time.

In this chapter, we assume an infinite three-dimensional (3D) space, i.e., the domain of interest is much larger than the diffusion velocity. We also assume the diffusivity to be homogeneous (i.e., has no dependence on space or time) and isotropic. Furthermore, we assume a drift free space. Note that the above formulation can easily deal with both drift and reflection from boundaries, as will be discussed in Chapter 5, since these can be included as boundary conditions for (4.4) and the corresponding equation can then be solved numerically. However, our main goal in this chapter is to demonstrate the applicability of localizing diffusive sources using the Fokker-Planck equation and the corresponding difference compared with the classical approach. For the simplified environment, along with

the initial condition $f(\mathbf{r}, t_0) = \delta(\mathbf{r} - \mathbf{r}_0)$, the solution to (4.4) is given by

$$f(\mathbf{r}, t) = \frac{1}{4\pi D(t - t_0)^{3/2}} e^{-\|\mathbf{r} - \mathbf{r}_0\|^2 / 4D(t - t_0)} \quad (4.6)$$

where D is the coefficient of diffusivity, \mathbf{r}_0 is the release location, and t_0 is the release time.

Note that the above solution represents the probability density function (pdf) of one particle occupying position \mathbf{r} at time t , assuming it was released from location \mathbf{r}_0 at time t_0 . For a large number of particles starting from the same point (source location), the isometric lines are given by concentric circles, see Figure (4.1.a). This is an expected result, since for a large number of particles, the classical approach based on the well known Fick's law of diffusion is

$$\frac{\partial c(\mathbf{r}, t)}{\partial t} = \text{div}(\mathcal{D}\nabla c) \quad (4.7)$$

where \mathcal{D} is 3×3 classical diffusivity matrix and c is the concentration. Under the previously mentioned assumptions, the matrix \mathcal{D} reduces to a diagonal matrix (i.e., $\mathcal{D} = DI_3$), and the solution for (4.7) becomes

$$c(\mathbf{r}, t) = \frac{1}{4\pi D(t - t_0)^{3/2}} e^{-\|\mathbf{r} - \mathbf{r}_0\|^2 / 4D(t - t_0)} \quad (4.8)$$

Note that (4.8) shows the evolution of the concentration c which is deterministic (i.e. the expected value).

Figure (4.1) presents the evolution of 1000 and 50000 particles at different time steps. Observe that, for a large number of particles, Figure (4.1.a), the contour lines of the concentration (number of particles) are almost circular. On the other hand, for a small number of particles, the contour lines do not form a circular pattern. This can be seen from Figure (4.1.b). As a result, the estimation of the initial properties (intensity, location, time)

using the classical model can be inaccurate and can consequently lead to non-optimal decision making (detection, prediction, etc.).

4.3 Statistical Model

In this section we introduce a SDE based technique for estimating the different source properties. We assume a spatially distributed sensor array consisting of m chemical sensors measuring the number of particles at certain areas (volumes) and located at $\mathbf{r}_1, \mathbf{r}_2, \dots, \mathbf{r}_m$. Further, we assume that each sensor takes measurements at times t_1, \dots, t_k . Next, let y_{ij} be the number of particles measured by a sensor located at \mathbf{r}_i and time t_j . In general, the sensor measurements can be modeled as

$$y_{ij} = n_{ij}(n_0, r_0) + e_{ij} \quad (4.9)$$

where n_{ij} is the model predicted data and e_{ij} is the noise vector.

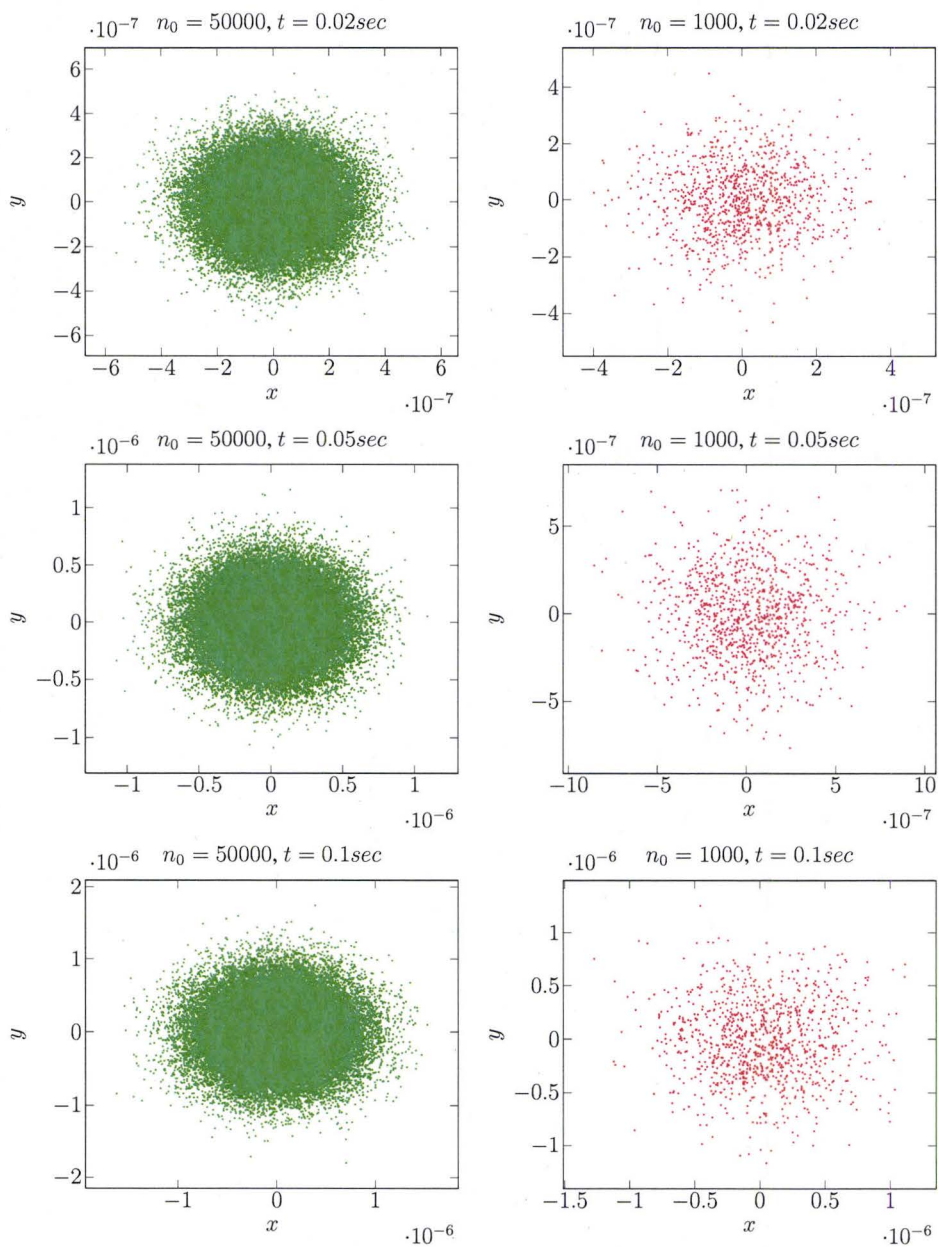
First, we compute the corresponding probability mass function (PMF) of model predicted data, i.e., the number of particles in an arbitrary spherical volume ($\Delta_i = \Delta(\mathbf{r}_i)$), that is corresponding to the sensor's volume, given by

$$\Delta_i = \|\mathbf{r} - \mathbf{r}_i\| \leq R_{sensor} \quad (4.10)$$

where R_{sensor} is the radius of the sensor.

Hence, the probability that there are n_i particles within Δ_i at time t_j becomes

$$P_j(y_{ij} = n) = \binom{n_0}{n} P_{j,\Delta_i}^n (1 - P_{j,\Delta_i})^{n_0-n} \quad n = 1, \dots, n_0 \quad (4.11)$$



(a) 50000 particles

(b) 1000 particles

Figure 4.1: Evolution of particles in two dimensional space. a) 50000 particles - green. b) 1000 particles - red.

where n_0 is the initial number of particles and P_{j,Δ_i} is the probability of a particle to occupy an volume Δ_i , which is given by

$$P_{j,\Delta_i} = \int \int \int_{\Delta_i} f(\mathbf{r}, t) r \partial r \partial \phi \quad (4.12)$$

Note that P_{j,Δ_i} can be computed numerically or analytically, since $f(\mathbf{r}, t)$ is a known function.

Next, assuming there are m sensors ($i = 1, \dots, m$) the joint PMF is given by

$$P_j(n_1, \dots, n_m) = \binom{n_0}{n_1 \cdots n_m} \cdot \left(1 - \sum_{i=1}^m P_{j,\Delta_i}\right)^{n_0 - \sum_{i=1}^m n_i} \cdot \prod_1^m P_{j,\Delta_i}^{n_i} \quad (4.13)$$

In the absence of noise the log likelihood function is given by

$$\begin{aligned} \mathcal{L}(\psi) &= \sum_{j=1}^k \log \binom{n_0}{y_{1j} \cdots y_{mj}} + \\ &+ \sum_{j=1}^k \sum_{i=1}^m y_{ij} \log P_{j,\Delta_i} + \\ &+ \sum_{j=1}^k \left\{ \left(n_0 - \sum_{i=1}^m y_{ij} \right) \log \left(1 - \sum_{i=1}^m P_{j,\Delta_i} \right) \right\} \end{aligned} \quad (4.14)$$

In the presence of noise, the probability mass function of the measurement vector \mathbf{y} becomes the convolution of the probability mass functions of the actual data, i.e., Equation (4.13), and the measurement noise. In order to account for the discrete nature of the measurement process, we propose to model the measurement noise using Poisson distribution. Note that Poisson distribution is commonly used for modeling the uncertainties in image processing problems [Chan 07, Han 07].

Next, we assume that the measurement noise is spatially and temporally uncorrelated Poisson distribution with a rate of λ

$$e_{ij} \sim \text{Pois}(\lambda)$$

$$\mathbb{E}[(e_{ij} - \lambda)(e_{i'j'} - \lambda)] = \lambda \delta(i - i') \delta(j - j')$$

where $\text{Pois}(\lambda)$ is a Poisson distribution with parameter λ and $\delta(\cdot)$ is the kronecker delta function.

The joint PMF of the measurement vector, derived in Appendix C, is given by

$$\begin{aligned} P(y_{1j}, \dots, y_{mj}) &= \sum_{\tau_1=0}^{y_{1j}} \cdots \sum_{\tau_m=0}^{y_{mj}} e^{-m\lambda} \binom{n_0}{\tau_1 \cdots \tau_m} \\ &\quad \left(1 - \sum_{i=1}^m P_{j, \Delta_i}\right)^{n_0 - \sum_{i=1}^m \tau_i} \prod_{i=1}^m \frac{\lambda^{y_{ij} - \tau_i}}{(y_{ij} - \tau_i)!} P_{j, \Delta_i}^{\tau_i} \end{aligned} \quad (4.15)$$

with the corresponding likelihood function

$$\begin{aligned} \mathcal{L}(\psi, \lambda) &= \prod_{j=1}^k \sum_{\tau_1=0}^{y_{1j}} \cdots \sum_{\tau_m=0}^{y_{mj}} e^{-m\lambda} \binom{n_0}{\tau_1 \cdots \tau_m} \\ &\quad \left(1 - \sum_{i=1}^m P_{j, \Delta_i}\right)^{n_0 - \sum_{i=1}^m \tau_i} \prod_{i=1}^m \frac{\lambda^{y_{ij} - \tau_i}}{(y_{ij} - \tau_i)!} P_{j, \Delta_i}^{\tau_i} \end{aligned} \quad (4.16)$$

and the corresponding log function is

$$\begin{aligned} \mathcal{L}(\psi, \lambda) &= \sum_{j=1}^k \log \sum_{\tau_1=0}^{y_{1j}} \cdots \sum_{\tau_m=0}^{y_{mj}} \binom{n_0}{\tau_1 \cdots \tau_m} \\ &\quad \left(1 - \sum_{i=1}^m P_{j, \Delta_i}\right)^{n_0 - \sum_{i=1}^m \tau_i} \prod_{i=1}^m \frac{\lambda^{y_{ij} - \tau_i}}{(y_{ij} - \tau_i)!} P_{j, \Delta_i}^{\tau_i} \end{aligned} \quad (4.17)$$

4.4 Numerical Examples

In this section, we present numerical examples to demonstrate the applicability of the proposed algorithms. we estimate n_0 and r_0 for different source strengths, number of sensors, and time samples. In all the examples, we assume the diffusion coefficient to be known, as it can be estimated using different techniques such as, the one in [Kvarnstrom 05, Kvarnstrom 06]. Also, we define the mean square error (MSE) as

$$\text{MSE}_\alpha = \frac{\|\hat{\alpha}_0 - \alpha_0\|^2}{\|\alpha_0\|^2} \quad (4.18)$$

where α_0 is the true value (i.e. n_0 or r_0) and $\hat{\alpha}_0$ is the corresponding MLE estimate.

Moreover, we calculate the probability density function (4.6) along with the integration (4.12) using finite element package (COMSOL Multiphysics). In order to achieve accurate results, the simulated domain is constrained with a spherical boundary which radius is much greater than the domain of interest. The numerical simulation is performed with 7450 elements and 11205 degrees of freedom. To illustrate the accuracy of the numerical method, we compare the results to the calculated analytical solution, of (4.6) and (4.12), for 10 time samples and 729 sample points that belongs to the domain of interest which is a square grid of 27×27 equally distributed points covering an area of $80 * 10^{-6} \times 80 * 10^{-6} m^2$. The diffusivity is taken to be $4.29 * 10^{-13} m/s^2$ and the time step is 0.02 sec. Figure (4.2) presents the histogram of relative error (i.e., $\frac{E_{analytical} - E_{numerical}}{E_{analytical}}$). The mean value of the relative error is 0.0399 which indicates an accurate numerical simulation.

Next, in Table (5.1), we show a comparison between the classical and stochastic estimations for $n_0 = 1000$, $m = 640$, $k = 15$, time step is 0.02 sec, and $\text{SNR} = 9$. The diffusivity is $4.29 * 10^{-13} m/s^2$ and the sensor array covers an area of $80 * 10^{-6} \times 80 * 10^{-6} m^2$. As

expected, the stochastic approach outperforms the classical technique since the number of particles is relatively small and the classical model does not account for its patterns, see Figure (4.1).

	Classical	Stochastic
Estimating intensity	18.01%	5.01%
Estimating location	16.26%	3.26%

Table 4.1: The estimation results of classical and stochastic estimation

Next, we show the estimation results in the absence of noise in Figures (4.2) and (4.3). In Figure (4.2a), we illustrate the mean square error for estimating the source intensity for $n_0 = 500$, as a function of the number of sensors and time samples, assuming that the release location and time are known. While in Figure (4.2b) we illustrates the mean square error for estimating the source location when the intensity is known. As expected, the estimation error decreases as the grid size increases. Moreover, increasing the number of time samples, reduces the estimation error. In Figure (4.3), we illustrate the estimation errors for n_0 and r_0 when both parameters are unknown. Observe that, the estimation error is higher than that when estimating n_0 and r_0 separately. Also, the error slope is smaller, therefore, increasing the grid size beyond certain value may not yield significant performance improvement. Similar results are obtained in Figures (4.4) and (4.5) for $n_0 = 1000$. As expected, increasing the number of particles gives more accurate results.

In Table (5.2), we show the reliability of the estimation algorithm, as the possible minimum achieved errors for the estimation of both n_0 and r_0 of different source intensities are

shown. It is obvious that the proposed algorithm provides satisfactory estimates for different intensities. On the other hand, it shows the importance of having a stochastic based estimation, as for very low source intensities, the estimation error increases.

Source intensity	min error in n_0	min error in r_0
500	4.11%	1.81%
1000	1.35%	0.091%

Table 4.2: Minimum error achieved for different source intensities.

For the case where Poisson noise is introduced, the estimation is carried for ($n_0 = 1000$) and ($k = 10$). We assume that the noise power is known, since, in principle, it can be estimated offline in the absence of the source. Also, the signal-to-noise ratio (SNR) is defined as the square root of the average (expected) signal value (μ_{sig}) to the square root of the sum of variances (which is also the mean value) of the Poisson noise (RMS_{noise}). The signal average is calculated over all time steps and sensors measurements, since the mean signal value is a spatial-temporal function. This definition of the SNR provides a deterministic representation and it doesn't vary from one run to run since the SNR is calculated using the expected values of n_{ij} from (4.13). The SNR is given by

$$\begin{aligned}
SNR &= 10\log \frac{\mu_{sig}}{RMS_{noise}} \\
&= 10\log \sqrt{\frac{\sum_{i=1}^m \sum_{j=1}^k \langle n_{ij} \rangle}{km\lambda}} \\
&= 5\log \frac{\sum_{i=1}^m \sum_{j=1}^k n_0 P_{j,\Delta_i}}{km\lambda} \tag{4.19}
\end{aligned}$$

This representation of the noise power is commonly used when calculating SNR [Raab , Haberkorn 82].

In Figures (4.6) and (4.7), we illustrate the error in estimating the source intensity and source location as a function of the SNR and the number of sensors (m). Observe that, satisfactory results can be reached when introducing the noise.

4.5 Conclusions

In this chapter, we address the problem of estimating the properties of diffusive sources using stochastic differential equations (SDE). The main advantage of our approach lies in the fact that it accounts (in a computationally efficient way) for random effects which are not accounted for in commonly used classical techniques based on Fick's law of diffusion. To achieve this goal, we utilize stochastic process and the corresponding Fokker-Planck equation to model the diffusion of particles. Then, we derive the corresponding probability mass function and maximum likelihood estimator for source intensity, location, and release time.

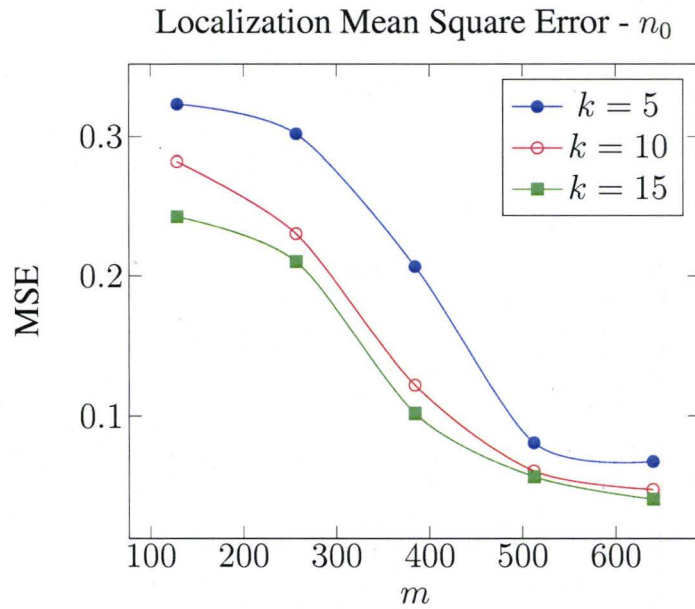
As expected, our proposed stochastic model significantly outperforms the classical approach. We demonstrate through numerical examples that the largest performance gain is achieved in the estimation of source intensity. In our opinion, estimating the source intensity is very critical, since potential failure to properly estimate the number of particles may result in severe consequences.

Our approach can be easily extended to various scenarios consisting of realistic geometries (urban environment, tunnel structures, turbulence etc.), by properly accounting

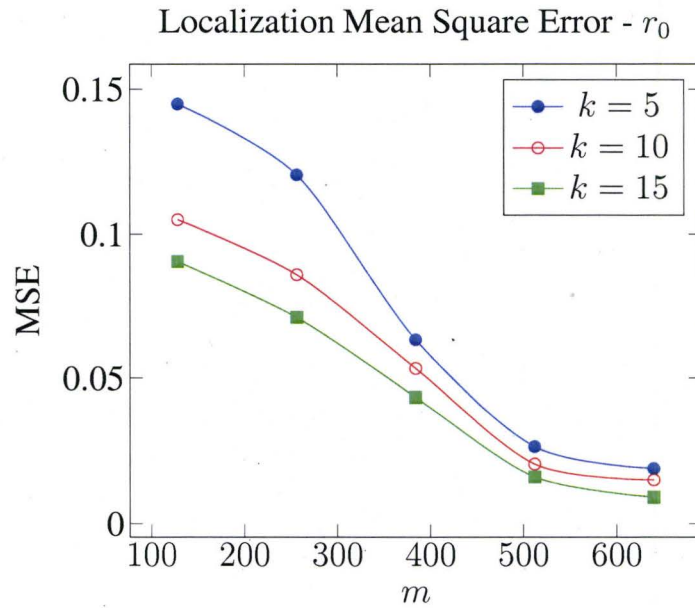
for drift (wind, flow) and boundary conditions. In the next chapter, we will include three dimensional geometries with different types of boundaries. In addition, we will evaluate the reliability of our estimator for various scenarios.

4.6 Publications

- A. Atalla and A. Jeremic, "*Localization of Diffusive sources Using Stochastic Differential Equations*", in revision for IEEE Trans. Signal Processing.
- A. Atalla and A. Jeremic, "*Localization of Chemical sources Using Stochastic Differential Equations*", IEEE International Conference on Acoustics, Speech and Signal Processing, pp 2573-2576.
- A. Atalla and A. Jeremic, "*Localization of Chemical Sources Using Stochastic Differential Equations in Realistic Environments*", COMSOL Conference 2008.

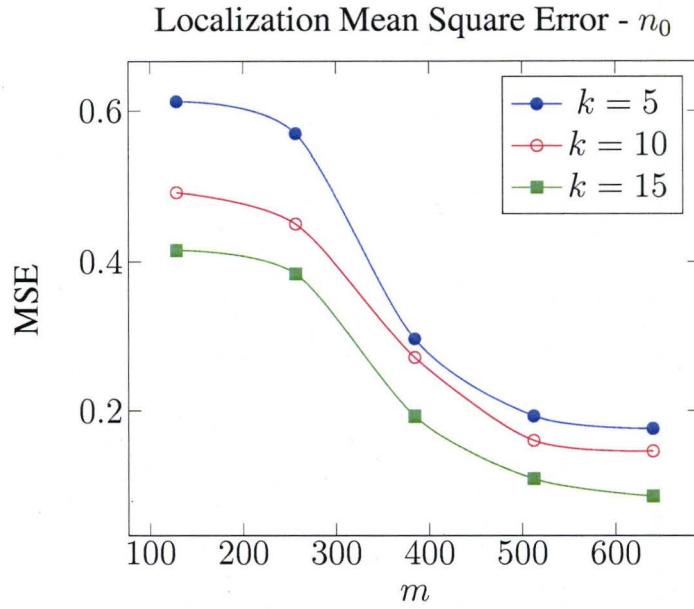


(a) MSE of estimating $n_0 - r_0$ is known.

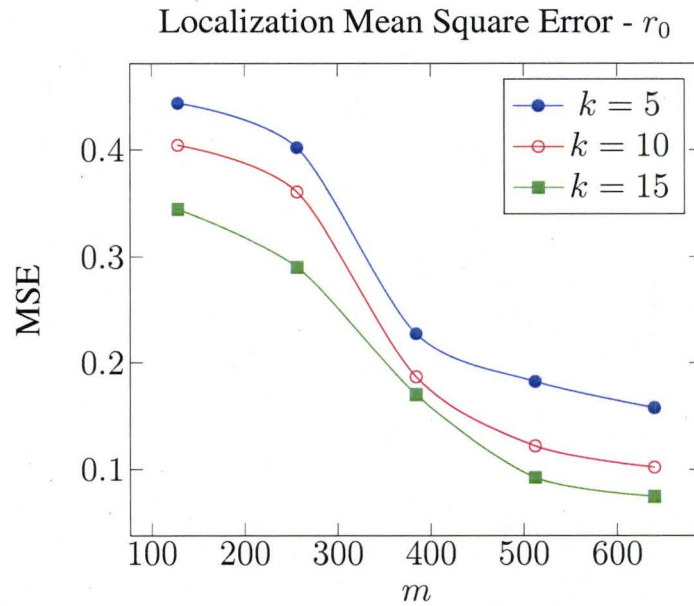


(b) MSE of estimating $r_0 - n_0$ is known.

Figure 4.2: Mean square error for estimating n_0 and r_0 as a function of number of sensors and time samples for 500 particles - in the absence of noise. a) MSE for estimating $n_0 - r_0$ is known. b) MSE for estimating $r_0 - n_0$ is known.

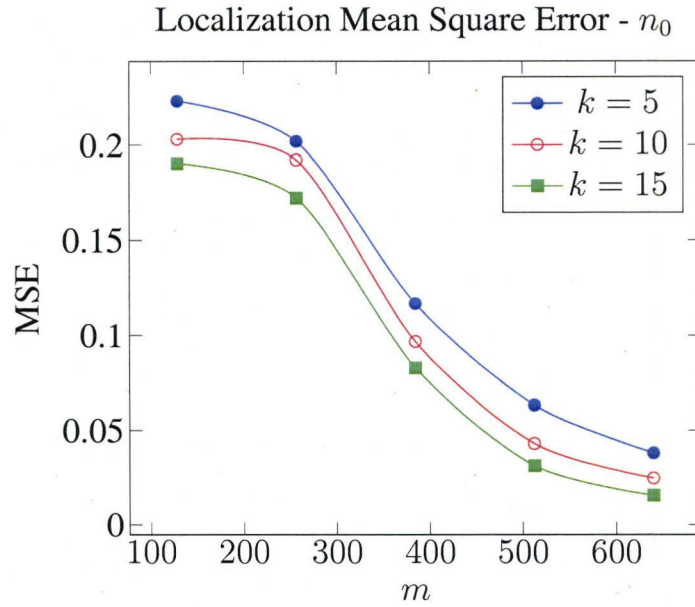


(a) MSE of estimating $n_0 - r_0$ is unknown.

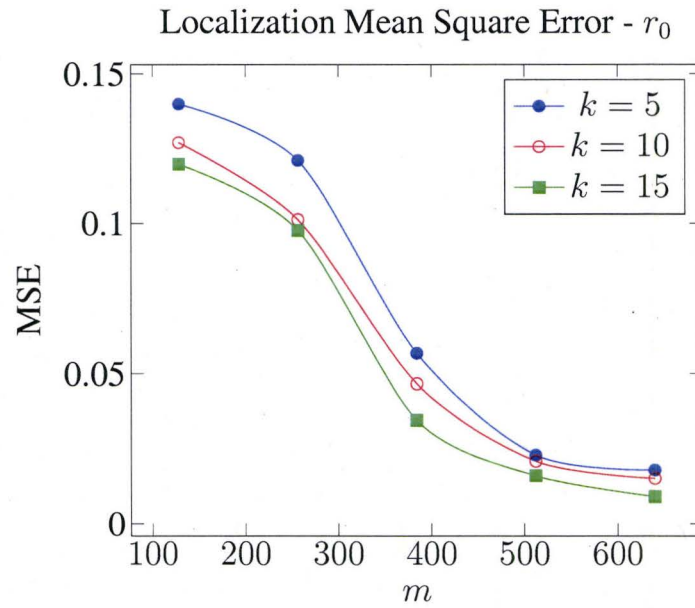


(b) MSE of estimating $r_0 - n_0$ is unknown.

Figure 4.3: Mean square error for estimating n_0 and r_0 as a function of number of sensors and time samples for 500 particles - in the absence of noise. a) MSE for estimating $n_0 - r_0$ is unknown. b) MSE for estimating $r_0 - n_0$ is unknown.



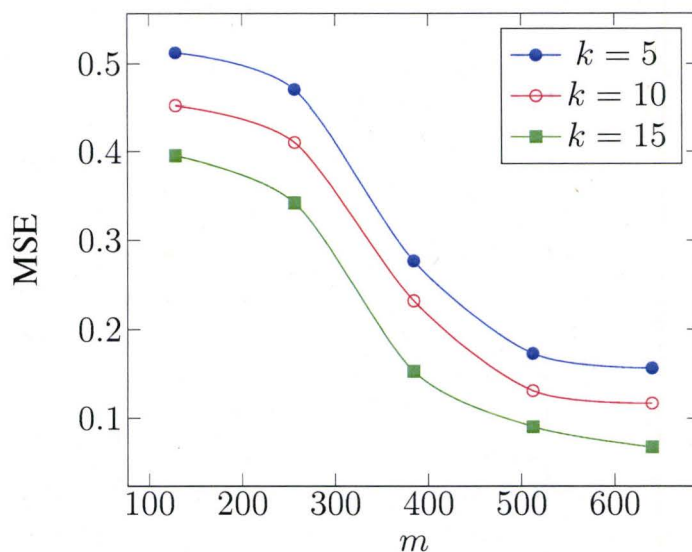
(a) MSE of estimating n_0 - r_0 is known.



(b) MSE of estimating r_0 - n_0 is known.

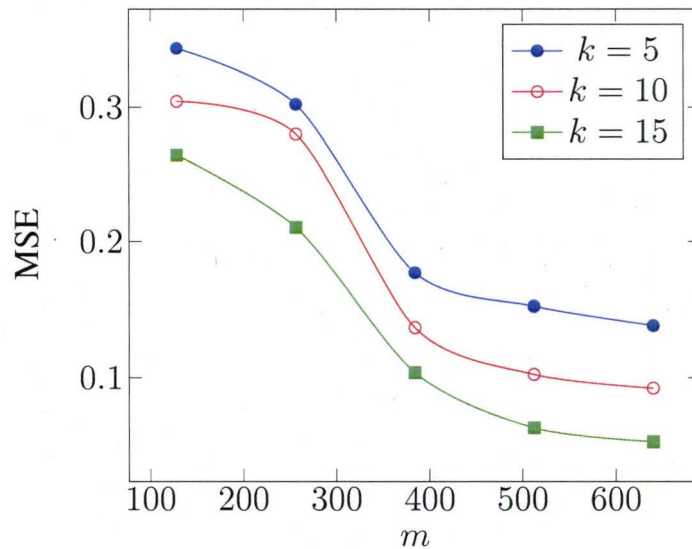
Figure 4.4: Mean square error for estimating n_0 and r_0 as a function of number of sensors and time samples for 1000 particles - in the absence of noise. a) MSE for estimating n_0 - r_0 is known. b) MSE for estimating r_0 - n_0 is known.

Localization Mean Square Error - n_0



(a) MSE of estimating n_0 - r_0 is unknown.

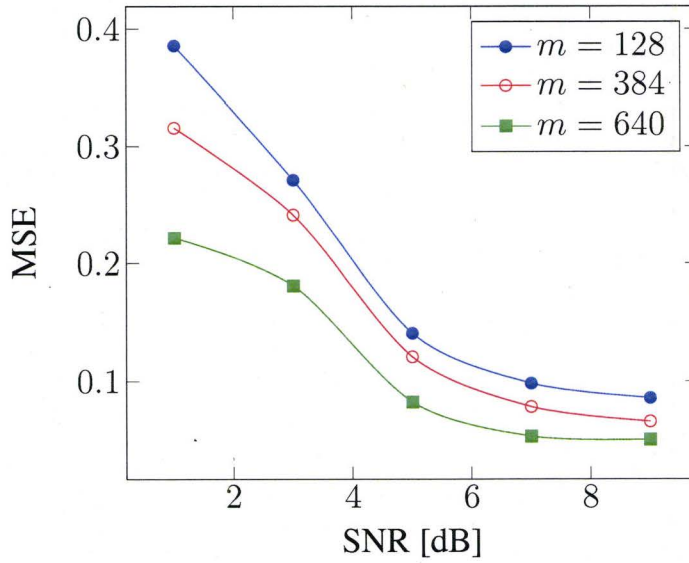
Localization Mean Square Error - r_0



(b) MSE of estimating r_0 - n_0 is unknown.

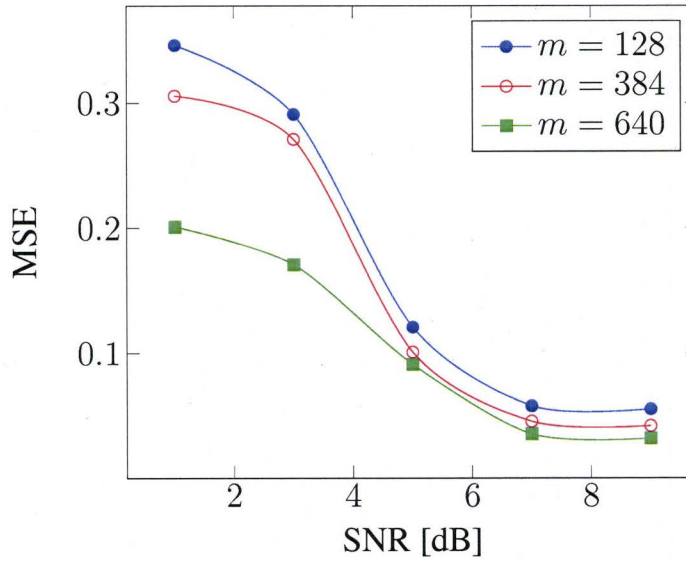
Figure 4.5: Mean square error for estimating n_0 and r_0 as a function of number of sensors and time samples for 1000 particles - in the absence of noise. a) MSE for estimating n_0 - r_0 is unknown. b) MSE for estimating r_0 - n_0 is unknown.

Localization Mean Square Error - $n_0 - k = 15$



(a) MSE of estimating $n_0 - r_0$ is known.

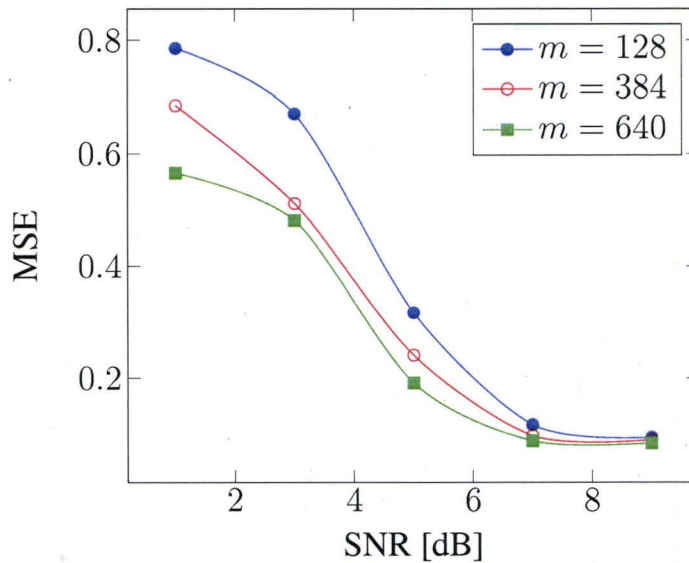
Localization Mean Square Error - $r_0 - k = 15$



(b) MSE of estimating $r_0 - n_0$ is known.

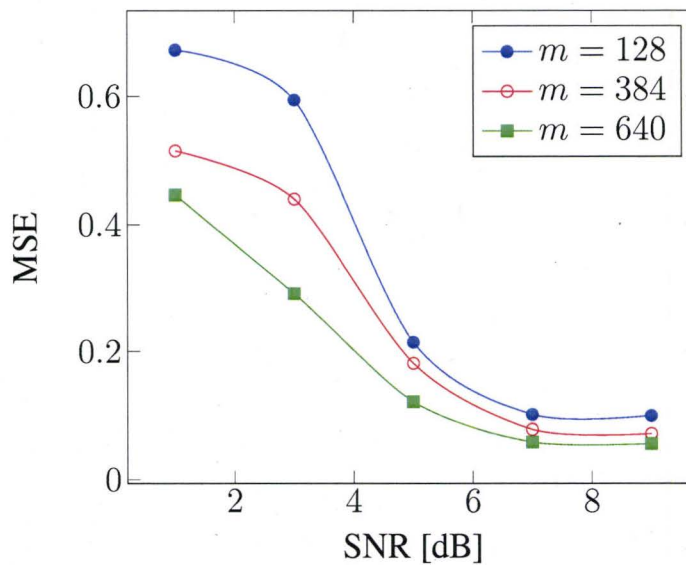
Figure 4.6: Mean square error for estimating n_0 and r_0 as a function of SNR and the number of sensors for 1000 particles. a) MSE for estimating $n_0 - r_0$ is known. b) MSE for estimating $r_0 - n_0$ is known.

Localization Mean Square Error - $n_0 - k = 15$



(a) MSE of estimating $n_0 - r_0$ is unknown.

Localization Mean Square Error - $r_0 - k = 15$



(b) MSE of estimating $r_0 - n_0$ is unknown.

Figure 4.7: Mean square error for estimating n_0 and r_0 as a function of SNR and the number of sensors for 1000 particles. a) MSE for estimating $n_0 - r_0$ is unknown. b) MSE for estimating $r_0 - n_0$ is unknown.

Chapter 5

Estimation of Boundary Properties

Using Stochastic Differential Equations

5.1 Introduction

The inverse diffusion problems deal with the estimation of many crucial parameters such as the diffusion coefficient, source properties, and boundary conditions. Such algorithms are widely applied in many design problems in different physical [Yang 96, Yang 97, Shiguemori 02, Vabishchevich 85], chemical [Nehorai 95, Jeremic 98, Porat 96, Jeremic 00, Ortner 07], and biological fields [Terayama 01]. Recently, the estimation of the boundary properties, of the diffusion process, have attracted researchers [Yang 96, Yang 97]. However, due to the complexity of the problem, the work accomplished is not yet satisfactory. On the other hand, most of the analytical and numerical methods proposed for such problems have only been used to deal with one- or at most two-dimensional problems with simple and symmetric geometries. Limited work has been achieved on three-dimensional problems, at which

simplified problems are solved. Moreover, the major purpose was to estimate the properties of a pre-determined boundary position. Nevertheless, they only account for the classical nature of the diffusion, neglecting its stochastic (random) nature described by the stochastic differential equations (SDE) and the Fokker-Planck equation [Risken 89].

Absorbing and reflecting boundaries are often encountered in realistic problems such as drug delivery where the organ surfaces represent reflecting/absorbing boundaries for the dispersion of drug particles [Terayama 01]. In this chapter, we extend previous results and propose a model that can deal with arbitrary boundaries. We are addressing the issue where we estimate the absorption property of the boundary. We propose a computationally efficient framework for estimating the boundary properties using stochastic differential equations. The main advantage of this technique lies in the fact that it accounts for both drift and random effects such as Brownian motion which are not accounted for in commonly used classical techniques based on Fick's law of diffusion. The extension to realistic geometry is straight forward since it can be dealt with using Finite Element Method. Absorbing and reflecting boundaries are often encountered in realistic problems such as drug delivery where the organ surfaces represent reflecting/absorbing boundaries for the dispersion of drug particles.

This chapter introduces a Fokker-Planck based algorithm in order to estimate the position and the length of the absorbing region of the boundary. We first utilize Fokker-Planck equation with the corresponding boundary conditions to derive the forward model, at which, we utilize the COMSOL Multiphysics package to solve for the position density function of the particle undergoing diffusion. Next, we deduce the corresponding statis-

tical model for the measurement of the number of particles. Finally, we show numerical examples to illustrate the proposed algorithm.

5.2 Physical Model

In the previous chapter we proposed a maximum likelihood algorithm for estimating the source intensity and location for particles under diffusion in homogeneous, drift-free space. However, this is a special configuration at which Fokker-Planck equation has an analytical solution. In this section we consider geometries with boundaries and drift.

In the presence of boundaries, we assume a domain \mathcal{V} , bounded by the surface \mathcal{S} , where \mathcal{S} is composed, in general, of mixed absorbing and reflecting boundaries, as in Figure (5.1).

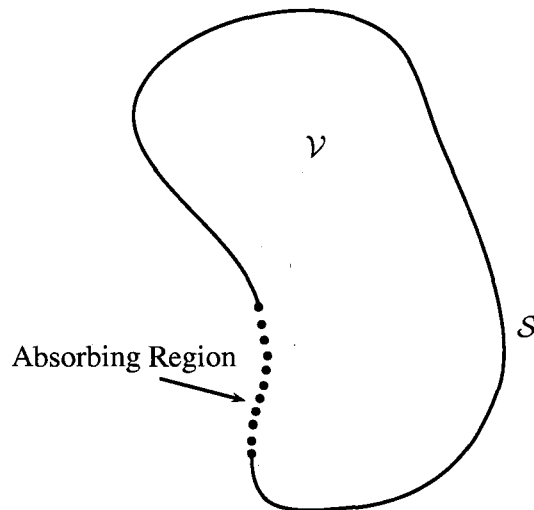


Figure 5.1: Bounded domain \mathcal{V} with boundary \mathcal{S} .

The behavior of a particle under a reflecting condition can be modeled with the specular reflection algorithm [Szymczak 03]. The implementation of the specular reflection can

be realized by reflecting each particle crossing the reflecting boundary. The stochastic trajectory X_t , in the region of a reflecting boundary defined by the local surface normal \hat{n} , evolves according to

$$\begin{aligned} X_{t+\Delta t} &= X_t + \Delta W_t, & X_t + \Delta W_t &\in \mathcal{V} \\ X_{t+\Delta t} &= X_t + dX_{t1} + |dX_{t2}| \cdot \hat{r}, & X_t + \Delta W_t &\notin \mathcal{V} \end{aligned} \quad (5.1)$$

where \hat{r} is the mirror reflection operator and Δt is the time step, and ΔW_t is the random jump at Δt , see Figure (5.2).

Specular reflection is commonly used to simulate a zero-flux boundary condition [Szymczak 03]. Other methods have also been proposed, these include the following

Rejection: [Drazer 01, Kurowski 94] the particle does not change its position for the given time step, i.e. $\Delta W_t = 0$.

Multiple rejection: [Rage 96] new increments are calculated until a ΔW_t is achieved such that $X_t + \Delta W_t \in \mathcal{V}$.

Interruption: [Salles 93, Maier 00] the particle stops at the wall and its clock is incremented by $\zeta \Delta t$ with given ζ by

$$X_{t+\zeta \Delta t} = X_t + \zeta \Delta W_t \quad (5.2)$$

Then, an additional step with $(1 - \zeta) \Delta t$ is performed.

However, all these algorithms fail to impose the zero-flux boundary condition correctly [Szymczak 03]. For the case of the absorbing boundary, a distribution of holes (hollow circles in Figure (5.3)) is introduced to account for the loss of the absorbed particles. Holes

are a fictitious particles that hold negative, but equal, mass to the particles. Mainly, the particles trying to cross the absorbing boundary are reflected and converted to holes, which are imaginary particles with negative and equal mass to the diffusive particles. Similarly, holes trying to recross the boundary are reflected and converted to particles, as in Figure (5.3). Finally, after sufficient time steps equal number of holes and particles are canceled within a sufficiently small volume. This algorithm has been introduced in [Szymczak 03] and has the advantage over the commonly called “total absorption” [Zhang 97a] method in the sense that it insures zero-concentration on the absorbing boundary. The total absorption method states that particles are removed when $X_t + \Delta W_t$ lies outside the domain \mathcal{V} .

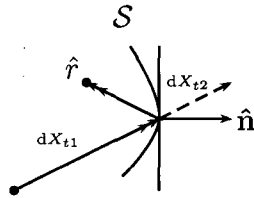
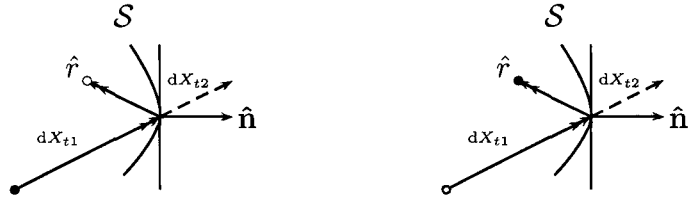


Figure 5.2: Behavior of a particle near a reflecting boundary.

Assuming three-dimensional environment $\mathbf{r} = (x_1, x_2, x_3)$, The probability density function, $f(\mathbf{r}, t)$, of one particle occupying space around \mathbf{r} at time t in homogeneous drift-free space, is given by

$$f(\mathbf{r}, t) = \frac{1}{4\pi D(t - t_0)^{3/2}} e^{-\|\mathbf{r} - \mathbf{r}_0\|^2 / 4D(t - t_0)} \quad (5.3)$$

where D is the coefficient of diffusivity. Note that, In 3D space, the variance corresponding to the diffusion process is a spherical function in time, given by $\sigma^2 = 6D(t - t_0)$. The



(a) Behavior of a particle near an absorbing boundary.

(b) Behavior of a hole near an absorbing boundary.

Figure 5.3: Specular reflection method. Solid dot represents a particle, hollow dot represents a hole.

observable contour of the particles underlying diffusion forms, in average, a sphere having a radius of $d = \sqrt{6D(t - t_0)}$, where d is called the mean diffusion distance, see Figure (5.4).

For the bounded domain with drift $v(\mathbf{r}, t)$, Fokker-Planck equation can be solved numerically, with the initial condition $f(\mathbf{r}, t_0) = \delta(\mathbf{r} - \mathbf{r}_0)$ and following boundary conditions [Reif 77]

$$f(\mathbf{r}, t) = 0 \quad \text{for absorbing boundaries} \quad (5.4)$$

$$\hat{\mathbf{n}} \cdot \nabla f = 0 \quad \text{for reflecting boundaries} \quad (5.5)$$

where $\hat{\mathbf{n}}$ is the normal vector to the boundary.

To illustrate the time evolution of $f(\mathbf{r}, t)$ in the presence of absorbing and reflecting boundaries, we solve the Fokker Planck equation, using a Finite Element package (COMSOL) for a closed circular domain consisting of a reflecting boundary (black segment) and an absorbing boundary (red segment of length l) as in Figure (5.5). In Figures (5.6.a and

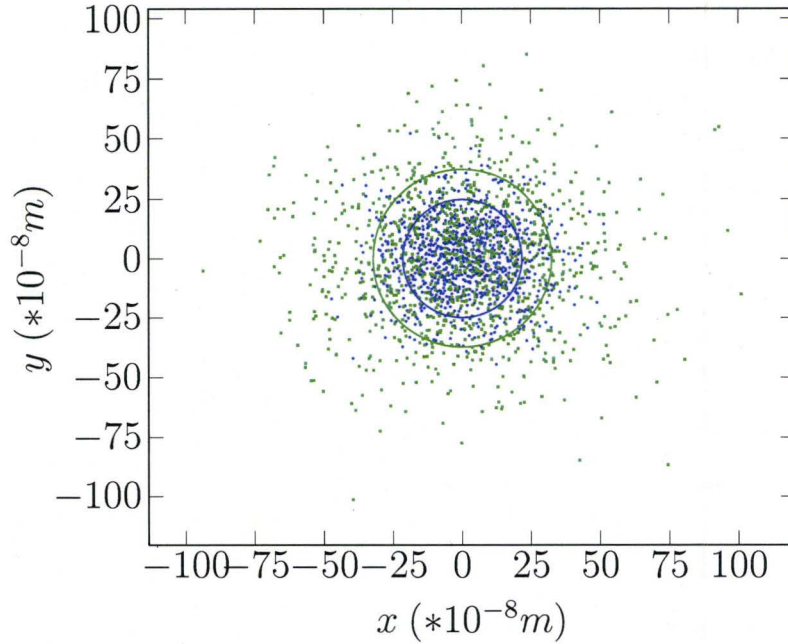


Figure 5.4: Mean diffusion distance for 1000 particles at two different time samples - $D = 4.29 * 10^{-13} m^2/s$. **Blue:** $t = 0.02 sec$, $d = 22.69 * 10^{-8} m$. **Green:** $t = 0.04 sec$, $d = 32.09 * 10^{-8} m$.

b), the effect of the absorbing boundary is idle since the flux of $f(\mathbf{r}, t)$ did not reach the boundary by then. On the other hand, in Figures (5.6.c and d), a region of lower probability (density) appears in the region nearby the absorbing boundary, since the probability of the particle to exist in this region is less than that for the other regions.

5.3 Statistical Model

In this section we introduce a SDE based technique for the estimation of boundary properties. In general, the parameters of the absorbing boundary can be estimated using the (MLE) that is based on the probability mass function (PMF) of the number of particles n

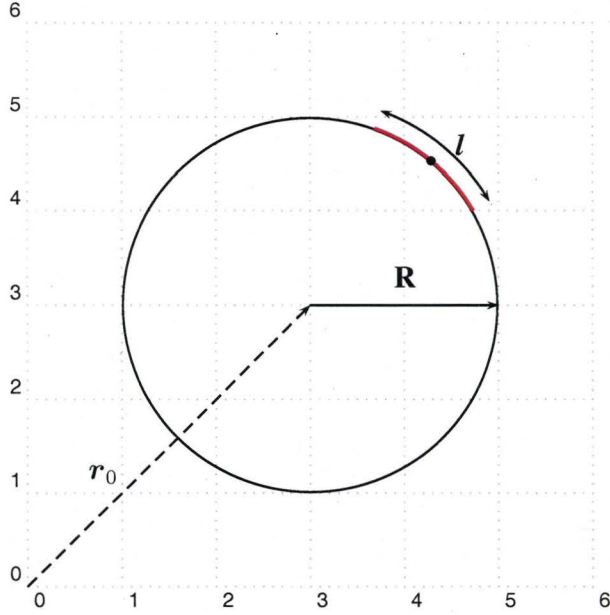


Figure 5.5: Closed circular domain with reflecting and absorbing boundaries - $R = 2mm$, $D = 4mm^2/s$, and $\pi/6 \leq l \leq \pi/3$

discussed in the previous section.

We assume a spatially distributed sensor array consisting of m chemical sensors measuring the number of particles at certain volumes and located at $\mathbf{r}_1, \mathbf{r}_2, \dots, \mathbf{r}_m$ inside the bounded geometry. Further, we assume that each sensor takes measurements at times t_1, \dots, t_k . Let y_{ij} be the number of particles measured by a sensor located at \mathbf{r}_i and time t_j . In general, the sensor measurements can be modeled as

$$y_{ij} = n_{ij}(\psi) + e_{ij} \quad (5.6)$$

where n_{ij} is the model predicted data, e_{ij} is the noise vector and ψ is the estimation parameter vector. This parameter vector considers boundaries characteristics such as size,

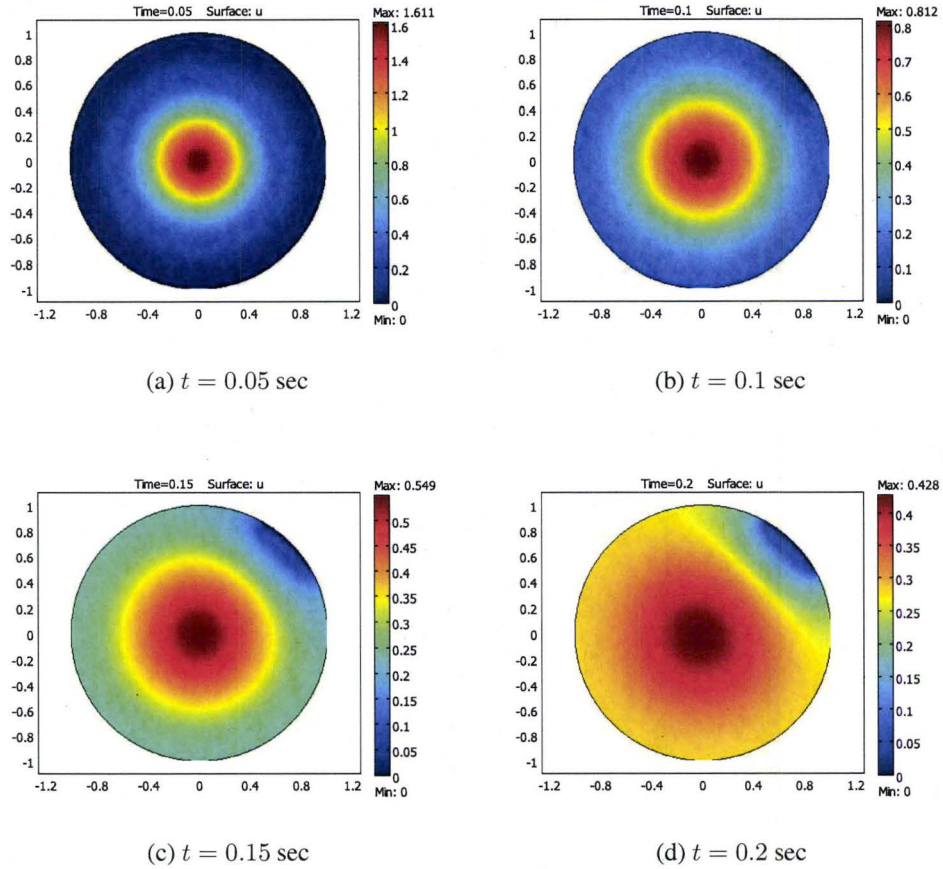


Figure 5.6: Evolution of $f(r, t)$ for a boundary problem.

position, etc...

The derivation of the probability mass function (PMF) of model predicted data and thereon to the log likelihood function is similar to the one introduced in Chapter 4, leads to

$$\begin{aligned}
 \mathcal{L}(\psi) &= \sum_{j=1}^k \log \binom{n_0}{y_{1j} \cdots y_{mj}} + \\
 &+ \sum_{j=1}^k \sum_{i=1}^m y_{ij} \log P_{j, \Delta_i} + \\
 &+ \sum_{j=1}^k \left\{ \left(n_0 - \sum_{i=1}^m y_{ij} \right) \log \left(1 - \sum_{i=1}^m P_{j, \Delta_i} \right) \right\}
 \end{aligned} \tag{5.7}$$

In this chapter we focus on demonstrating the ability to estimate the boundary properties and hence, assume that the source properties (i.e., n_0) are known or have been previously estimated. Thus, the first term of $l(n_0, \mathbf{r}_0, t_0)$ can be removed and the log likelihood function becomes

$$\begin{aligned} \mathcal{L}(\psi) = & \sum_{j=1}^k \sum_{i=1}^m y_{ij} \log P_{j, \Delta_i} + \\ & + \sum_{j=1}^k \left\{ \left(n_0 - \sum_{i=1}^m y_{ij} \right) \log \left(1 - \sum_{i=1}^m P_{j, \Delta_i} \right) \right\} \end{aligned} \quad (5.8)$$

In the presence of noise, the probability mass function of the measurement vector \mathbf{y} becomes the convolution of the probability mass functions of the actual data, i.e., Equation (4.13), and the measurement noise. In order to account for the discrete nature of the measurement process, we propose to model the measurement noise using Poisson distribution. Note that Poisson distribution is commonly used for modeling the uncertainties in image processing problems [Chan 07, Han 07].

Next, we assume that the measurement noise is spatially and temporally uncorrelated Poisson distributed with a rate of λ

$$\begin{aligned} e_{ij} & \sim \text{Pois}(\lambda) \\ \mathbb{E}[(e_{ij} - \lambda)(e_{i'j'} - \lambda)] & = \lambda \delta(i - i') \delta(j - j') \end{aligned}$$

where $\text{Pois}(\lambda)$ is a Poisson distribution with parameter λ and $\delta()$ is the Kronecker delta function.

The log likelihood function, derived in a similar way to 4.17, is given by

$$\mathcal{L}(\psi, \lambda) = \sum_{j=1}^k \log \sum_{\tau_1=0}^{y_{1j}} \cdots \sum_{\tau_m=0}^{y_{mj}} \binom{n_0}{\tau_1 \cdots \tau_m} \cdot \left(1 - \sum_{i=1}^m P_{j, \Delta_i}\right)^{n_0 - \sum_{i=1}^m \tau_i} \prod_{i=1}^m \frac{\lambda^{y_{ij} - \tau_i}}{(y_{ij} - \tau_i)!} P_{j, \Delta_i}^{\tau_i} \quad (5.9)$$

5.4 Estimation Algorithm

The estimation algorithm, in Figure(5.7), consists mainly of a Matlab based optimization code that interacts with both the Brownian simulator and a PDE solver. The Brownian simulator is based on the $it\tilde{o}$ stochastic differential equation presented in Equation (5.1) combined with the specular reflection method to account for the different boundary conditions. In order to find the unknown number of parameters, we propose the following algorithm

Step 1: Submit the initial guess to the main code i.e., ψ_0 .

Step 2: Solve for $f(r, t)$, using FD/FE method.

Step 3: Calculate P_{j, Δ_i} , using Gauss quadrature method to calculate the integration in Equation (4.12).

Step 4: Using the Brownian simulator, compute the current particle positions. Combine it with Poisson noise to generate the measurement vector y_i .

Step 5: Estimate the next boundary condition vector (ψ) using data from steps 3 and 5.

Step 6: Repeat steps 2-5 until stratifying:

$$[\hat{\psi}]^T = \arg \max_{\psi} \mathcal{L}(\psi, \lambda) \quad (5.10)$$

Step 7: Output $\hat{\psi}$, the vector of estimated parameters.

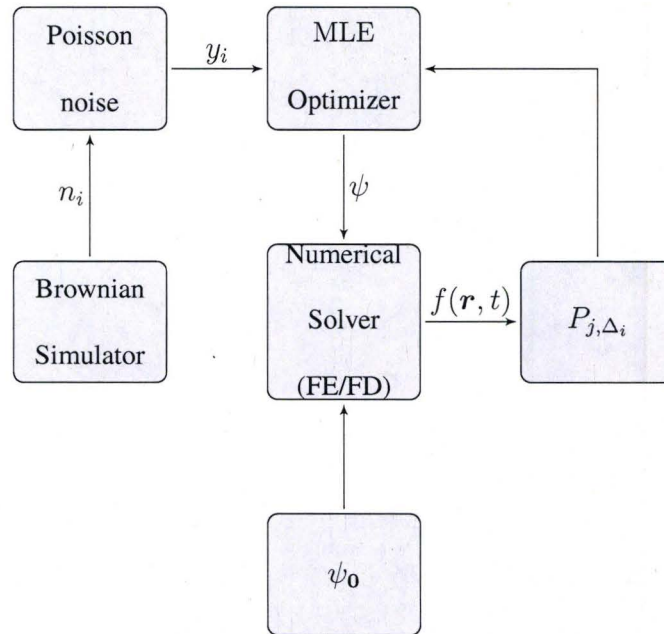


Figure 5.7: Flow chart.

5.5 Numerical Results

In this section, we present numerical examples to demonstrate the applicability of the proposed algorithms. We estimate the position and the size of the absorbing segment for two different examples

1. *Sphere with absorbing segment:*
2. *Cylinder with absorbing segment:*

In all the examples, we assume the diffusion coefficient to be known, as it can be estimated using different techniques such as, the ones in [Kvarnstrom 05, Kvarnstrom 06]. Also,

the signal-to-noise ratio (SNR) is defined as

$$\text{SNR} = 5 \log \frac{\sum_{i=1}^m \sum_{j=1}^k n_0 P_{j, \Delta_i}}{km\lambda}$$

5.5.1 Sphere with absorbing segment

We now present numerical results that demonstrates the applicability of the proposed algorithms. The forward model was created using a Brownian simulator of 500 and 1000 particles in a drift free medium surrounded by a spherical boundary with radius-diffusivity ratio $R^2/6D = 10$. We also assume a sudden appearance of an absorbing region defined by $(R, \theta_1 : \theta_2, \phi_1 : \phi_2)$, shown in Figure (5.8). The diffusive particles are assumed to reach equilibrium, i.e. uniformly distributed, prior to the change in the boundary conditions. We define the parameter vector as

$$\psi = [\theta_1, \theta_2, \phi_1, \phi_2]^T \quad (5.11)$$

Also, we define the MSE as

$$\text{MSE}_{\psi} = \frac{\|\hat{\psi}_i - \psi_i^*\|^2}{\pi} \quad (5.12)$$

where ψ_i^* is the true value (i.e. $\psi_i^* \in \{\theta_1^*, \theta_2^*, \phi_1^*, \phi_2^*\}$) and $\hat{\psi}_i$ is the corresponding MLE estimate.

In order to achieve better computational time, we first show, in Table (5.1), a computational-time based comparison between the FE and FD methods. Both methods are used to solve the Fokker Planck equation for the geometry introduced in Figure (5.8). Then, the estimation of the boundary properties is carried out for 5000 particles, 15 times samples and 18 sensors. The estimation is then repeated 1000 times. Finally, the estimation results are compared in accuracy. The percentage accuracy represents the average accuracy of

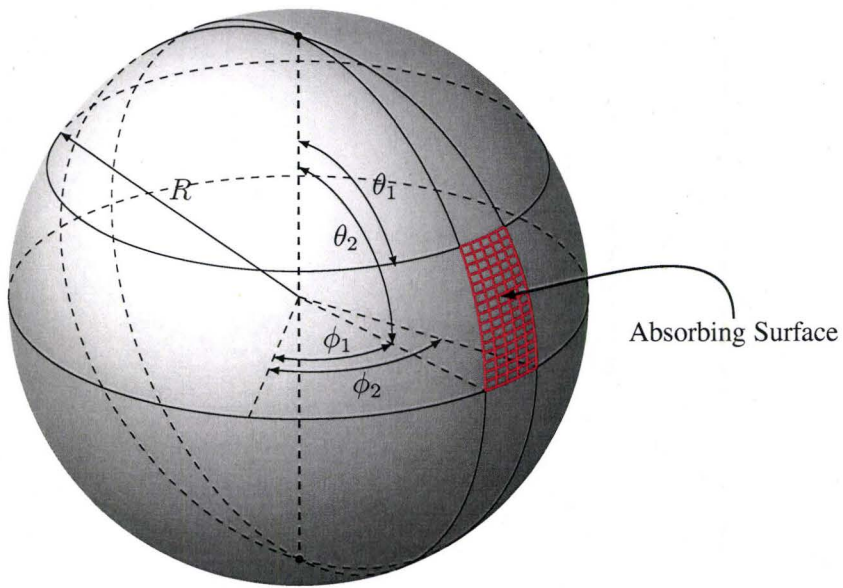


Figure 5.8: Sphere with absorbing segment defined by $(R, \theta_1 : \theta_2, \phi_1 : \phi_2)$.

the four different estimation parameters. Obviously, the FD technique outperforms the FE package regarding the required computational time to achieve an accuracy level of almost 98% accuracy. Hence, in all the examples, we use the FD solver in the estimation process.

	FE Package (COMSOL)	FD Solver
Computational time (sec)	5.45	3.26
Nodes	3422	5400
Accuracy	98.3%	97.91%

Table 5.1: Computational times for FE and FD solvers.

In Figures (5.9 and 5.10), we illustrate the MLE error in estimating the size and the position of the absorbing region for 500 and 1000 particles, respectively. The number of time samples is 15 and the grid includes 18 sensors. The presented results represent an average of 1000 runs. As expected, the estimation error decreases when increasing the SNR and reaches satisfactory results when $\text{SNR} > 5$.

In Figures (5.11-5.14), we show the robustness curves in order to study the reliability of the proposed algorithm subjected to the error in estimating the diffusion tensor (D) and the initial concentration (n_0) for the cases of $n_0 = 500$ and $n_0 = 1000$. Observe that, the proposed algorithm is very robust with respect to errors in both D and n_0 . However, as the error rapidly increases, the reliability with respect to errors strongly decreases and the performance deteriorates.

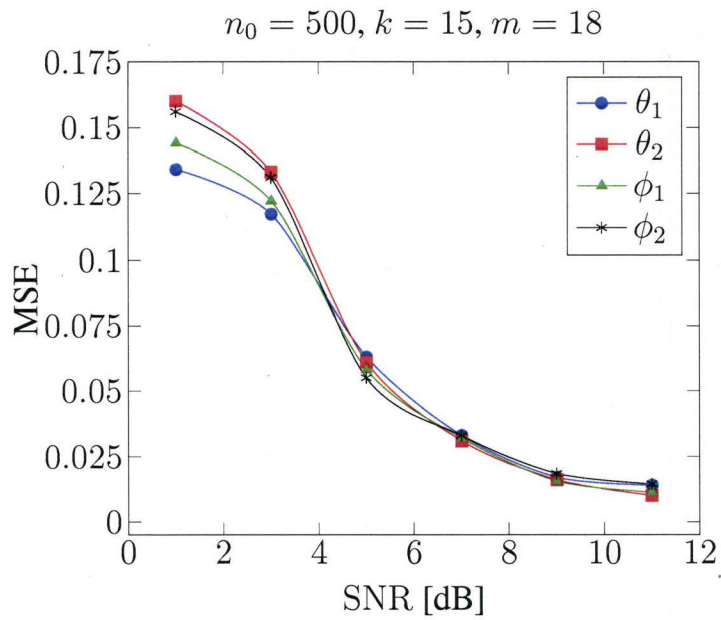


Figure 5.9: MLE error of the absorbing region - $n_0 = 500$.

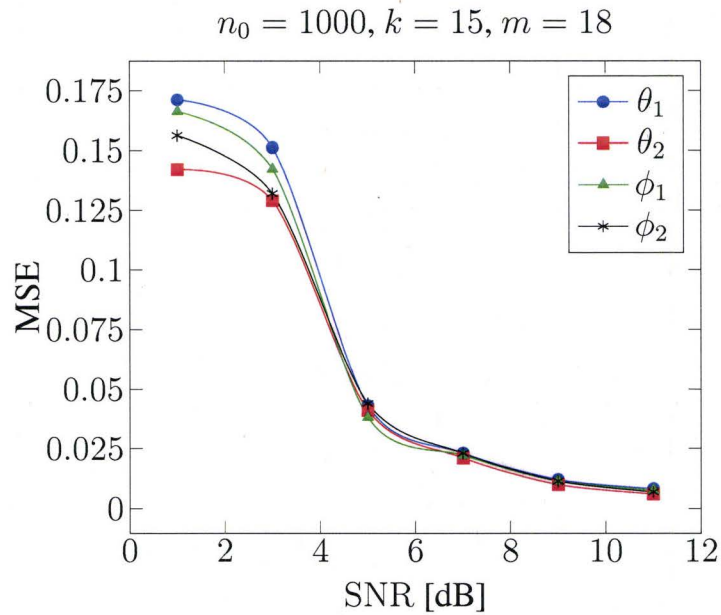


Figure 5.10: MLE error of the absorbing region - $n_0 = 1000$.

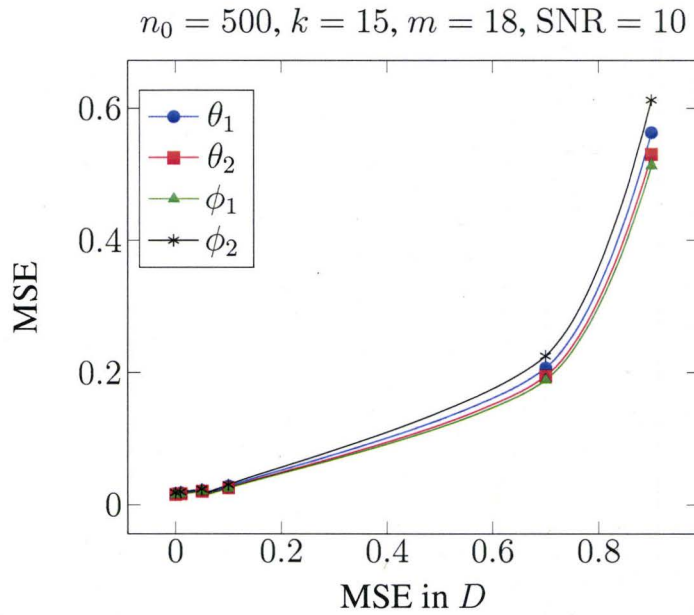


Figure 5.11: Robustness curves with respect to MSE in $D - n_0 = 500$.

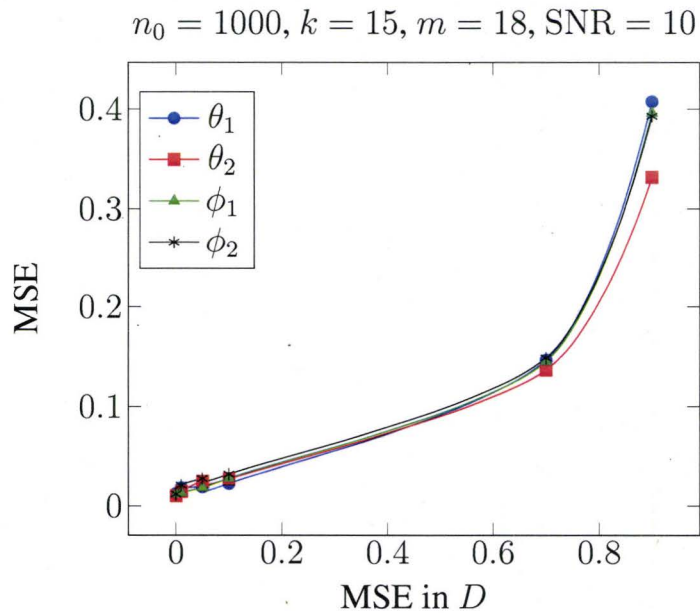


Figure 5.12: Robustness curves with respect to MSE in $D - n_0 = 1000$.

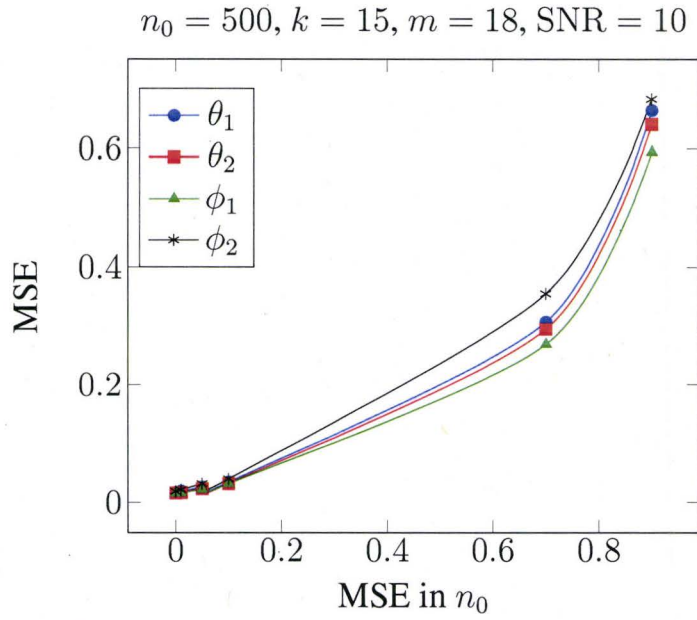


Figure 5.13: Robustness curves with respect to MSE in $n_0 - n_0 = 500$.

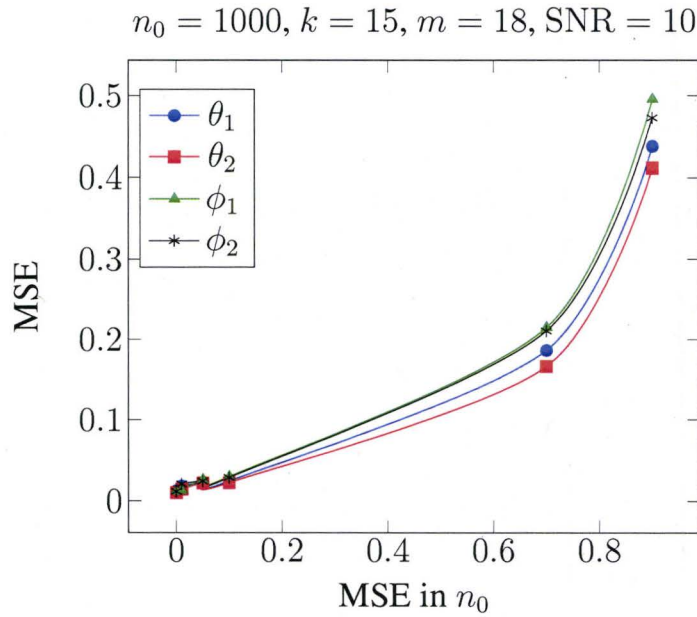


Figure 5.14: Robustness curves with respect to MSE in $n_0 - n_0 = 1000$.

5.5.2 Cylinder with absorbing segment

In this section, we present numerical examples to demonstrate the applicability of the proposed algorithm in the presence of a drift. The forward model was created using a Brownian simulator of 1000 particles subjected to a laminar velocity field inside a cylindrical geometry with an absorbing region defined by $(R, \phi_1 : \phi_2, z_1 : z_2)$, shown in Figure (5.15). The laminar flow is given by

$$\frac{v(\mathbf{r}, t) = v(1 - \rho^2)}{R^2} \quad (5.13)$$

where v is maximum velocity and R is the radius.

The estimation is carried out using 15 time samples and 18 sensors and represents an average result for 1000 runs. We define the parameter vector as

$$\psi = [\phi_1, \phi_2, z_1, z_2]^T \quad (5.14)$$

Also, we define the relative errors as

$$\text{MSE}_\phi = \frac{\|\hat{\phi}_i - \phi_i^*\|^2}{2\pi} \quad i = 1, 2 \quad (5.15)$$

$$\text{MSE}_z = \frac{\|\hat{z}_i - z_i^*\|^2}{L} \quad i = 1, 2 \quad (5.16)$$

where ϕ_i^* and z_i^* are the true values, $\hat{\phi}_i$ and \hat{z}_i are the corresponding MLE estimates.

In order to achieve better computational time, once more, we show in Table (5.2), a comparison between the FE and FD methods. Both methods are used to solve the Fokker Planck equation for the geometry introduced in Figure (5.15). The estimation of the boundary properties is carried out for 5000 particles, 15 times samples and 18 sensors. The estimation is then repeated 1000 times and the estimation results are compared in accuracy. The

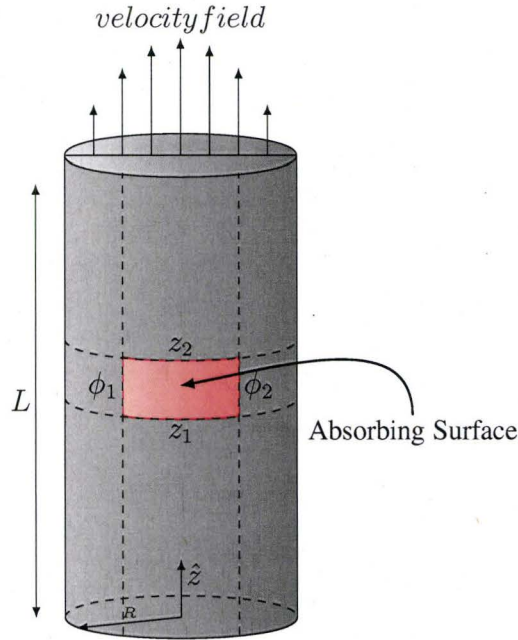


Figure 5.15: Cylinder with absorbing segment defined by $(R, \phi_1 : \phi_2, z_1 : z_2)$.

percentage accuracy represents the average accuracy of the four different estimation parameters. Obviously, the FD technique outperforms the FE package regarding the required computational time to achieve an accuracy level of almost 97% accuracy. Hence, in all the examples, we use the FD solver in the estimation process.

	FE Package (COMSOL)	FD Solver
Computational time (sec)	6.81	4.10
Nodes	4682	6380
Accuracy	97.01%	97.62%

Table 5.2: Computational times for FE and FD solvers.

In Figure (5.16), we show the estimation results for a drift free medium with $R/D = 10$. In

Figure (5.17), we illustrate the estimation error when the drift-diffusivity relation is given by

$$\beta = \frac{(R^2/6D)}{(L/v)} = 0.5 \quad (5.17)$$

Note that, in the previous relation, the numerator (L/v) presents the minimum time required for a particle to reach the end of the tube by the drift action (traveling time). On the other hand, the denominator $(R^2/6D)$ shows the mean time for a particle to hit the cylindrical boundary (hitting time). This ratio helps in understanding the maximum velocity at which the estimation is feasible.

In Figures (5.18 and 5.19), we illustrate the estimation results at different field velocities (i.e. different values of β). In Figure (5.18), for reference purposes, we illustrate the estimation error when the velocity is known. In Figure (5.19), we illustrate the estimation error when all the parameters are unknown. As expected, when the hitting time is higher than the traveling time, the performance deteriorates exponentially and the estimation is not feasible. This is because, most of the particles tend to reach the end of the tube before being absorbed. Hence, the estimation algorithm fails to detect any absorption in the system. This justifies the very low hitting-to-traveling time ratio in human capillaries. In average the human capillary has a length of $1mm$ with a radius of approximately $6\mu m$. El Shahed [Elshahed 04], studied the effect of exchange of fluid across the capillary wall on the flow of blood with slip velocity and proposed a closed form for the velocity fields. His results show a maximum axial velocity of $10mm/s$. This gives a traveling-to-hitting time ratio of 0.01 which is adequate for the capillary exchange process to take place efficiently.

In Figures (5.20-5.23), we show the robustness curves in order to study the reliability of

the proposed algorithm subjected to the error in estimating the diffusion tensor (D) and the initial concentration (n_0) for the cases of drift free and $\beta = 0.5$. Observe that, the proposed algorithm is very robust with respect to errors in both D and n_0 . However, as the error rapidly increases, the reliability with respect to errors strongly decreases and the performance deteriorates.

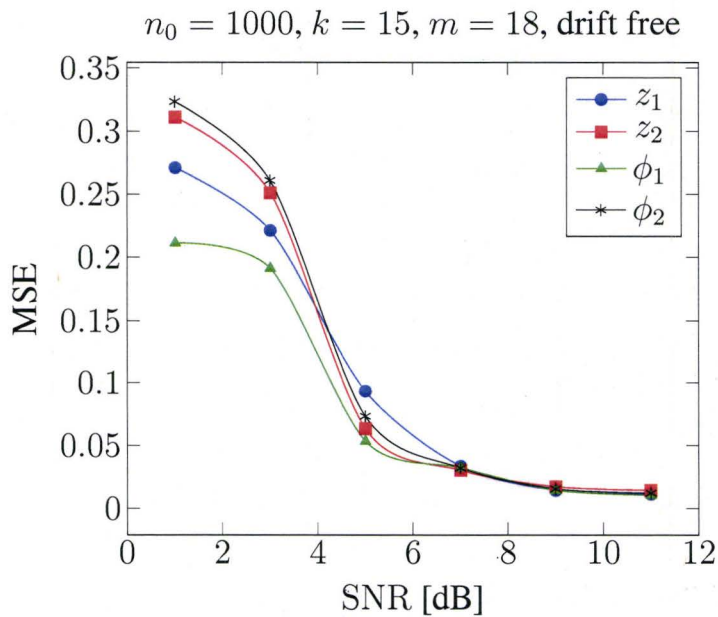


Figure 5.16: MLE error of the absorbing region - no drift.

5.6 Conclusions

In this chapter, we addressed the problem of estimating the size and the position of an absorbing region in the presence and absence of drift. This model can be extended to model an arbitrary region as well as to account for random flow. To the best of our knowledge, this is a first attempt to estimate the absorbing region using stochastic differential equations

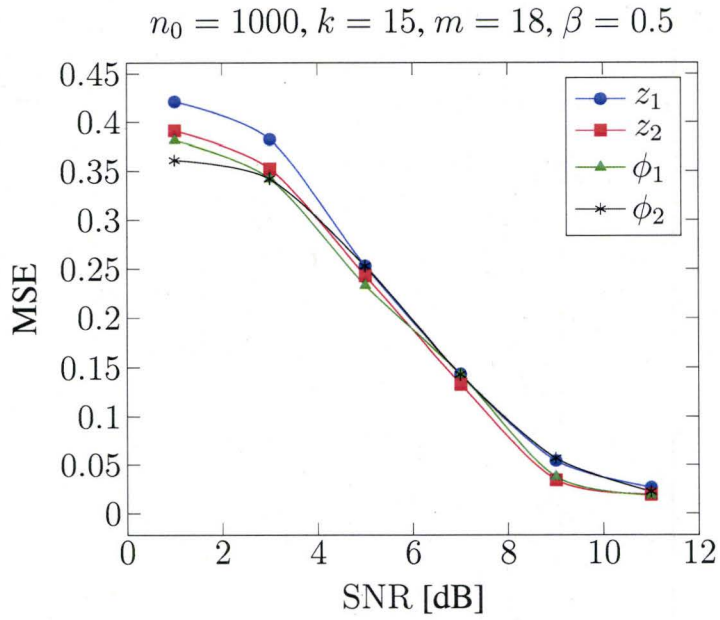


Figure 5.17: MLE error of the absorbing region.

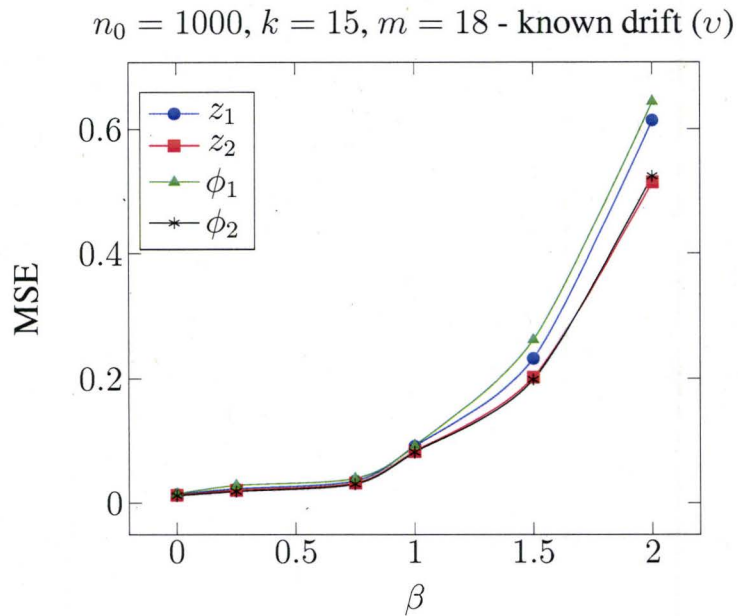


Figure 5.18: MLE error of the absorbing region - known drift.

$n_0 = 1000, k = 15, m = 18$ - unknown drift (v)

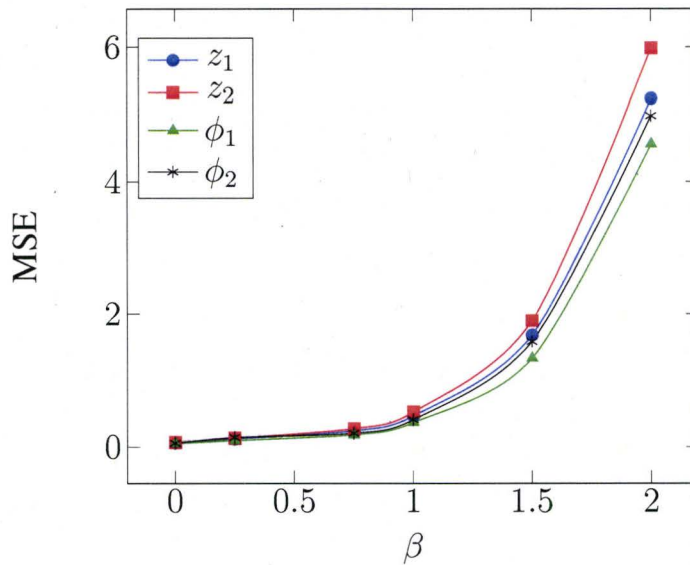


Figure 5.19: MLE error of the absorbing region - unknown drift.

$n_0 = 1000, k = 15, m = 18, \text{SNR} = 10, \text{drift free}$

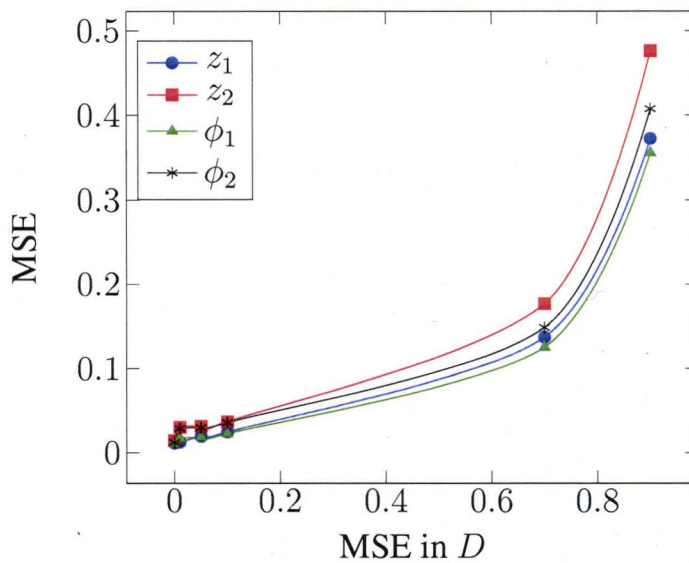


Figure 5.20: Robustness curves with respect to MSE in D - drift free.

$n_0 = 1000, k = 15, m = 18, \text{SNR} = 10, \beta = 0.5$

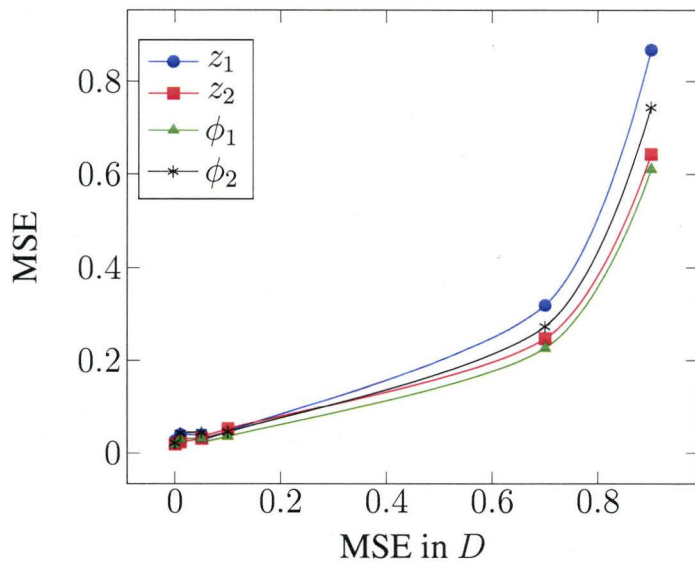


Figure 5.21: Robustness curves with respect to MSE in D - $\beta = 0.5$.

$n_0 = 1000, k = 15, m = 18, \text{SNR} = 10, \text{drift free}$

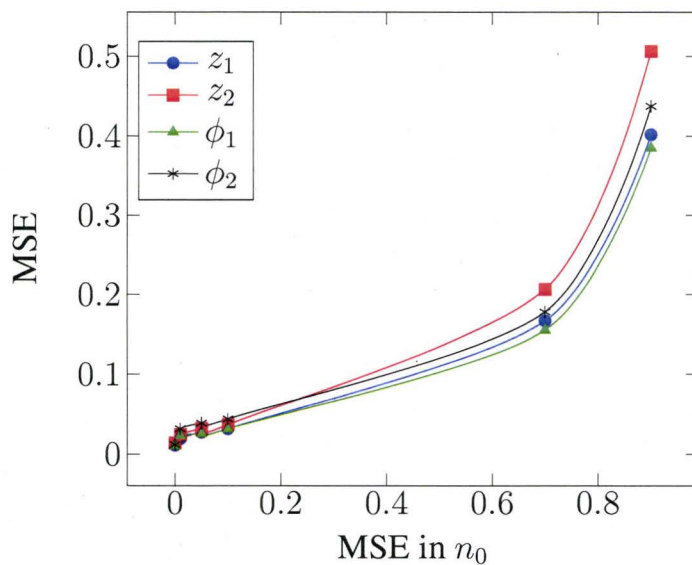


Figure 5.22: Robustness curves with respect to MSE in n_0 - drift free.

$n_0 = 1000, k = 15, m = 18, \text{SNR} = 10, \beta = 0.5$

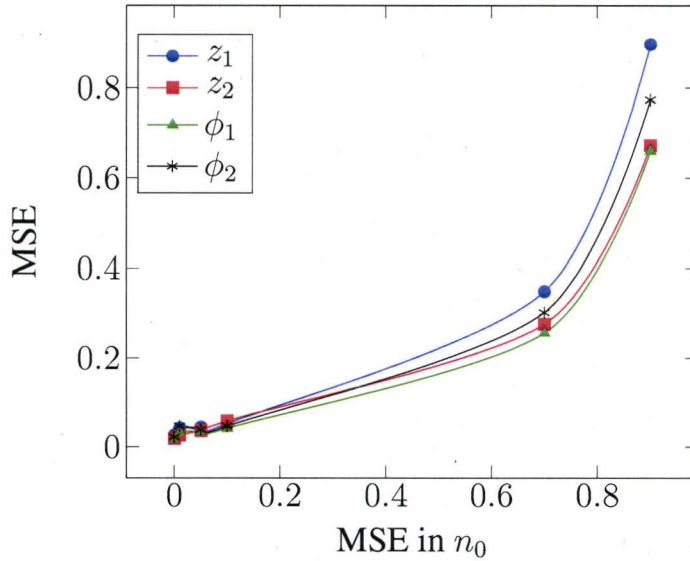


Figure 5.23: Robustness curves with respect to MSE in $n_0 - \beta = 0.5$.

in the presence of drift and our preliminary results indicate that the problem is invertible i.e., the unknown parameters can be estimated under certain conditions of the flow speed.

5.7 Publications

- A. Atalla, A. Jeremic and A. Nehorai, “*Estimation of Boundary Properties Using Stochastic Differential Equations*”, to appear in *Journal of Applied Mathematics*.
- A. Atalla and A. Jeremic, “*Estimation of Boundary Properties Using Stochastic Differential Equations and COMSOL*”, COMSOL Conference 2009.
- A. Atalla and A. Jeremic, “*Estimation of Boundary Properties Using Stochastic Differential Equations*”, Canadian Conference on Electrical and Computer Engineering, CCECE 2009, pp 385-389.

Chapter 6

Modeling the Bacterial Clearance in Capillary Network Using Coupled Stochastic-Differential and Navier-Stokes Equations

6.1 Introduction

The capillary network is a complex-interconnected structure. A single blood cell traveling from the arteriole to a venule via a capillary bed passes through, on average in the respiratory system, 40 – 100 capillary segments [Doerschuk 00]. The cardiovascular systems is responsible for delivering blood to the tissue under sufficient pressure to exchange materials. This is a two way process, at which nutrients, Oxygen, and other materials are carried to the tissue and cells during the outflow. On the other hand, blood is returned along with

the wastes of cellular metabolism during the return flow.

Tissue fluid exchange occurs in capillary beds, where blood is in close proximity to tissue fluid (that surrounds all the cells in the body). This is because the thin walls of the capillaries (one endothelial cell layer) allow the movement of many materials to cross them with relative ease. Moreover, the lower blood velocity in capillaries (compared to the other blood vessels) allows sufficient time for effective exchange. Capillary - tissue fluid exchange is controlled by the blood pressure in the capillary and the osmotic pressure of blood (pressure of the tissue fluid outside the capillaries). As blood enters the capillary bed at the arteriole end, the blood pressure on the walls of the capillary is about 40 *mmHg*. By the time blood travels to the venule end of a capillary bed, it drops to about 15 *mmHg*. The blood pressure acts to push plasma fluid from the blood into the tissues. The osmotic pressure exerted by blood due to high concentrations of dissolved salts and plasma proteins is constant at about 25 *mmHg*. These dissolved salts and proteins make blood hypertonic to tissue fluid. The osmotic pressure of blood acts to pull water (tissue fluid) back into the blood.

There are three mechanisms whereby capillary exchange can occur. These are:

Diffusion, which depends on the presence of a concentration gradient across the capillary wall.

Bulk flow, which depends on mechanical forces (pressures) across the capillary wall. It occurs through pores and intercellular clefts and follows Poiseuille's equation for hydrodynamic flow.

Vesicular transport, which depends on the formation of specific transport systems in the capillary wall. it is involved in the translocation of macromolecules across capillary endothelium

It is necessary to have an accurate model for the capillary-tissue exchange mechanism. This can be useful in many applications such as understanding the dispersion of drug particles, through vascular system, in human tissue [Terayama 01, Yano 89] as well as understanding the behavior of bacterial dispersion [Cannon 32] and and the factors influencing its clearance [Green 64, Holman 04, Pollard Jr 84, Rogers 60].

Modeling the exchange process can be carried by means of coupling the classical diffusion (Fick's law) with Navier-Stokes equations. However, for a small number of particles, classical diffusion fails to introduce a satisfactory representation of the particle dispersion. It has been observed that the patterns of drug dispersion in human body organs exhibit certain irregularities (discontinuities) which can not be modeled with Fick's law of diffusion even using anisotropic and nonhomogeneous diffusivity. In order to accurately model the exchange process, we propose a stochastic based model of the diffusion process based on the well known Fokker Planck equation [Risken 89]. In order to account for the different mechanisms whereby capillary exchange can occur (diffusion and bulk flow), we model the capillary walls with means of pressure-dependent anisotropic diffusivity with slip conditions for the plasma flow inside the capillary. The main advantage of this technique lies in the fact that it accounts for both drift and random effects such as Brownian motion which are not accounted for in commonly used classical techniques based on Fick's law of diffusion. The extension to realistic geometry is straight forward since it can be dealt with using

Finite Element Method.

This chapter is organized as follows. First, we introduce the flow model using Navier-Stokes equations. Next, we utilize Fokker Planck equation with convection field to represent the probability function of the position of a particle (i.e, single bacteria) in the capillary-tissue region. Then, we compute the probabilities of absorption and transmission (clearance) of a single particle. and utilize them to compute the probability mass function (PMF) of the total number of bacterial particles.

6.2 Capillary Blood Flow Model

Many attempts are done to study the motion of blood through a capillary segment. Oka and Murata [Oka 70] studied the steady motion of blood through the capillary wall using a linear model of the blood flow and utilizing Starling's law, that is, the rate of flow per unit area across the the wall boundary is directly proportional to the pressure difference across the wall. However, Srivastava [Srivastava 83] showed that the linearized model fails to give an adequate representation of the flow field, especially in short vessels. Oka's linear model has been extended to the non-linear case by Mariamma and Maghi [Mariamma 00]. They considered the steady laminar flow of the blood as a homogeneous Newtonian fluid in tube with permeable wall. Elshahed [El-Shahed 04] studied the effect of exchange of fluid across the capillary wall on the flow of blood with slip velocity and proposed a closed form the velocity fields. In this work, we solve the set of equations provided by Elshahed numerically, in order to compute the velocity field through the capillary.

Consider the motion of blood as an incompressible Newtonian fluid. We consider a three dimensional circular cylindrical tube, representing a capillary segment of radius R and finite length L with permeable wall to promote fluid exchange across the wall. The equations of momentum and continuity are given by

$$\rho \left(\underbrace{\frac{\partial \mathbf{u}}{\partial t}}_{\text{Unsteady acceleration}} + \underbrace{\mathbf{u} \cdot \nabla \mathbf{u}}_{\text{Convective acceleration}} \right) = \underbrace{-\nabla p}_{\text{Pressure gradient}} + \underbrace{\mu \nabla^2 \mathbf{u}}_{\text{Viscosity}} + \underbrace{\mathbf{f}}_{\text{Other body forces}} \quad (6.1)$$

$$\nabla \cdot \mathbf{v} = 0 \quad (6.2)$$

where ρ is the plasma fluid density, μ is the viscosity, p is the hydrostatic capillary blood pressure, and \mathbf{u} is the velocity vector.

In cylindrical coordinates, neglecting the gravitational forces, (6.1) and (6.2) can be expanded to

$$\begin{aligned} r : \quad & \rho \left(\frac{\partial u_r}{\partial t} + u_r \frac{\partial u_r}{\partial r} + \frac{u_\theta}{r} \frac{\partial u_r}{\partial \theta} + u_z \frac{\partial u_r}{\partial z} - \frac{u_\theta^2}{r} \right) = -\frac{\partial p}{\partial r} + \\ & + \mu \left[\frac{1}{r} \frac{\partial}{\partial r} \left(r \frac{\partial u_r}{\partial r} \right) + \frac{1}{r^2} \frac{\partial^2 u_r}{\partial \theta^2} + \frac{\partial^2 u_r}{\partial z^2} - \frac{u_r}{r^2} - \frac{2}{r^2} \frac{\partial u_\theta}{\partial \theta} \right] \\ \theta : \quad & \rho \left(\frac{\partial u_\theta}{\partial t} + u_r \frac{\partial u_\theta}{\partial r} + \frac{u_\theta}{r} \frac{\partial u_\theta}{\partial \theta} + u_z \frac{\partial u_\theta}{\partial z} + \frac{u_r u_\theta}{r} \right) = -\frac{1}{r} \frac{\partial p}{\partial \theta} + \\ & + \mu \left[\frac{1}{r} \frac{\partial}{\partial r} \left(r \frac{\partial u_\theta}{\partial r} \right) + \frac{1}{r^2} \frac{\partial^2 u_\theta}{\partial \theta^2} + \frac{\partial^2 u_\theta}{\partial z^2} + \frac{2}{r^2} \frac{\partial u_r}{\partial \theta} - \frac{u_\theta}{r^2} \right] \\ z : \quad & \rho \left(\frac{\partial u_z}{\partial t} + u_r \frac{\partial u_z}{\partial r} + \frac{u_\theta}{r} \frac{\partial u_z}{\partial \theta} + u_z \frac{\partial u_z}{\partial z} \right) = -\frac{\partial p}{\partial z} + \\ & + \mu \left[\frac{1}{r} \frac{\partial}{\partial r} \left(r \frac{\partial u_z}{\partial r} \right) + \frac{1}{r^2} \frac{\partial^2 u_z}{\partial \theta^2} + \frac{\partial^2 u_z}{\partial z^2} \right] \end{aligned} \quad (6.3)$$

$$\frac{1}{r} \frac{\partial}{\partial r} (r u_r) + \frac{1}{r} \frac{\partial u_\theta}{\partial \theta} + \frac{\partial u_z}{\partial z} = 0 \quad (6.4)$$

The radial velocity u_r is governed by Starling's law which is a mathematical model for fluid movement across capillaries, given by

$$u_r = K[(p - p_i) - (\varrho_c - \varrho_i)] \quad (6.5)$$

where, K is the filtration constant which is the product of the capillary surface area (A) and the capillary hydraulic conductance (L_c), i.e., $K = AL_c$. p_i is the hydrostatic interstitial hydrostatic fluid pressure, ϱ_c is the capillary oncotic pressure (osmotic pressure of the plasma proteins), and ϱ_i is the tissue oncotic pressure (osmotic pressure of the proteins in the interstitial fluid).

Note that, in the previous equation, $[(p - p_i) - (\varrho_c - \varrho_i)]$ represents the net driving pressure for filtration. The corresponding boundary conditions are

$$\phi \frac{\partial u_z}{\partial r} + u_z = 0 \quad \text{at } r = R \quad (6.6a)$$

$$u_r = \frac{K\mu}{R} \left(\frac{p}{\varrho_c - \varrho_i + p_i} - 1 \right) \quad \text{at } r = R \quad (6.6b)$$

$$p = p_a \quad \text{at } z = 0 \quad (6.6c)$$

$$p = p_v \quad \text{at } z = L \quad (6.6d)$$

The boundary condition (6.6a) is the Beavers and Joseph condition while (6.6b) results from Starling's law, where $\phi = \sqrt{k}/\delta R$, δ is the slip parameter and k is the specific permeability of the porous medium. (6.6a) reduces to the no-slip condition when $k = 0$. Also, p_a and p_v are the pressures at the arterial and venous ends, respectively.

The introduced system of equations, i.e., (6.3)-(6.6), is solved using Finite Element package (COMSOL Multiphysics) for a capillary segment with specifications defined in Table (6.1).

In Figure (6.1), we show the axial velocity field profile along the radial direction at the

Capillary specifications	
L	1mm
R	1 μ m
ρ	1025kg/m ³
μ	0.0015Ns/m ² at 37°
$p_{\text{atriole end}}$	40mmHg
$p_{\text{vanule end}}$	15mmHg
p_i	-6mmHg
Q_c	25mmHg
Q_i	5mmHg
L_c	28.6 * 10 ⁻⁷ cm/(s · cmH ₂ O), cmH ₂ O = 0.098KPa
ϕ	0 and 0.15

Table 6.1: Capillary specifications.

center of the capillary. Observe that the axial velocity increases as the slip coefficient (ϕ) increases and vice versa. Moreover, it coincides with the no-slip condition when $\phi = 0$. In figure (6.2), we illustrate the variation of axial velocity along the axis $r = 0$ for different ϕ . It is observed that u_z has a concave profile downwards with a minimum around the center of the capillary segment. In Figure (6.3), we present the radial velocity at two different levels of the capillary. observe that, the radial velocity is positive (fluid is pushed outwards) at the beginning of the capillary segment, where the capillary blood pressure, p , is greater than the tissue fluid pressure. Moving along the capillary, the blood pressure decreases (as described in Figure (6.4)) and the radial velocity is acting to push the tissue fluid inside the capillary (i.e., negative). Also, observe that the blood pressure almost has a linear relation with the capillary-segment length. The deviation from linearity is due to the introduction of the permeable wall condition in (6.6b). This relation is very important in this context and will be utilized in Section 6.4.

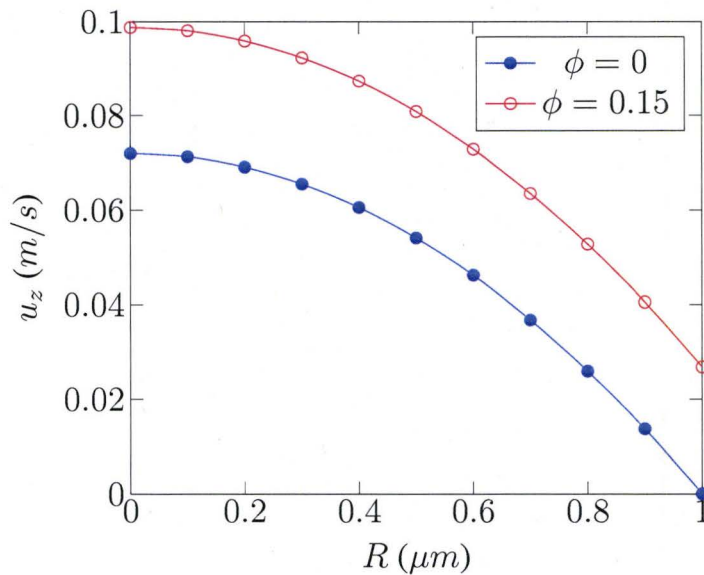


Figure 6.1: Axial velocity profile at $z = L/2$ for different slip coefficients.

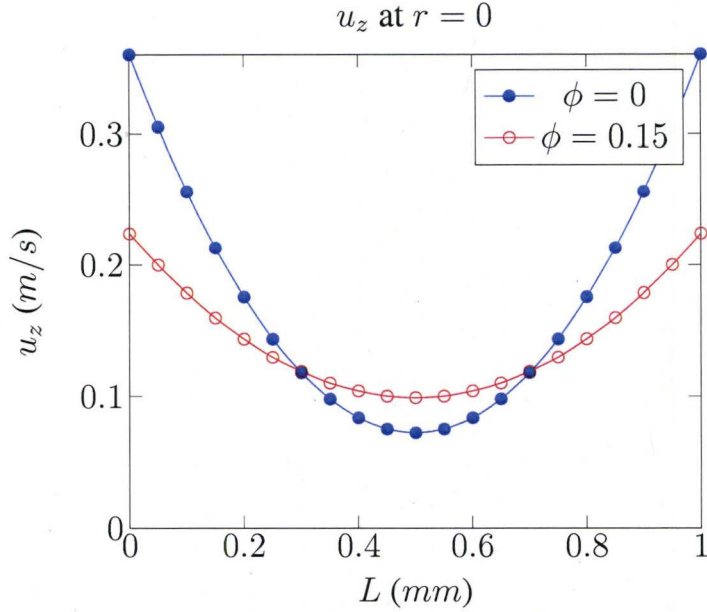


Figure 6.2: Axial velocity profile along the axis $r = 0$ for different slip coefficients.

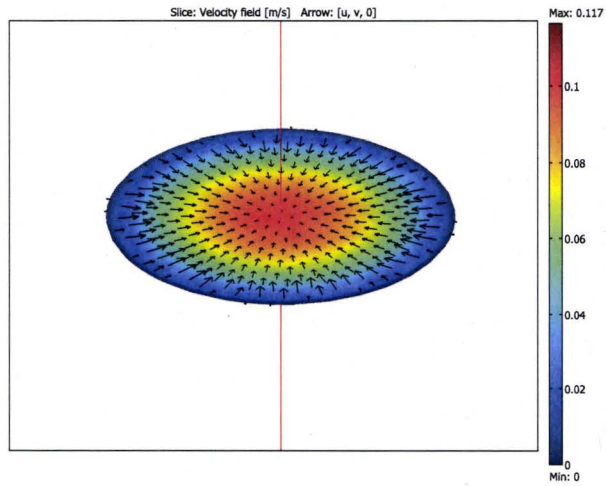
6.3 Modeling the Exchange Process

In order to model the dispersion of particles through and inside a capillary segment, let us assume that at an arbitrary time t_0 we introduce n_0 (or equivalently concentration c_0) particles at location r_0 being at the beginning of the capillary segment. To model the motion of the particles we utilize the $it\tilde{o}$ stochastic differential equation, described previously in Chapters 4 and 5,

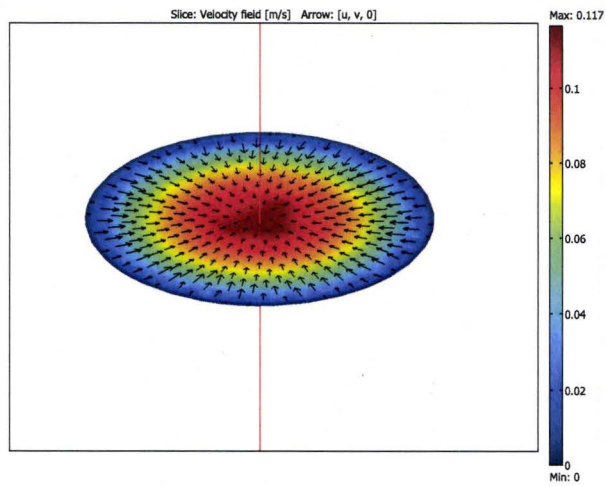
$$dX_t = \mu(X_t, t)dt + \sigma(X_t, t)dW_t \quad (6.7)$$

where X_t , in R^3 , is the location and W_t is a standard Wiener process in R^3 .

Assuming three-dimensional environment $r = (x_1, x_2, x_3)$, we compute the probability density function, $f(r, t)$, of one particle occupying space around r at time t using the



(a) Arteriole end - $L = 0$.



(b) Venule end - $L = 1\text{mm}$.

Figure 6.3: Radial velocity at two different levels of the capillary segment.

Fokker-Planck equation [Risken 89]

$$\frac{\partial f(\mathbf{r}, t)}{\partial t} = \left[- \sum_{i=1}^3 \frac{\partial}{\partial x_i} D_i^1(\mathbf{r}) + \sum_{i=1}^3 \sum_{j=1}^3 \frac{\partial^2}{\partial x_i \partial x_j} D_{ij}^2(\mathbf{r}) \right] f(\mathbf{r}, t) \quad (6.8)$$

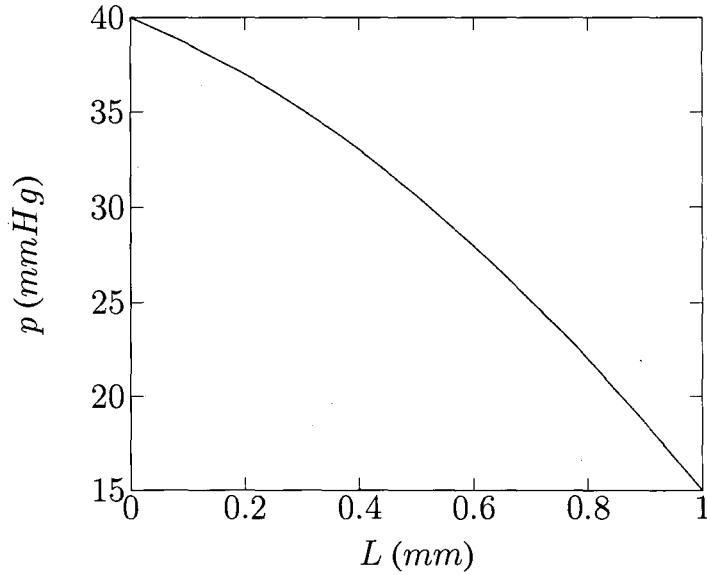


Figure 6.4: Pressure profile along the axis $z = 0$ of a capillary segment.

where partial derivatives apply the multiplication of D and $f(\mathbf{r}, t)$, D^1 is the drift vector and D^2 is the diffusion tensor given by

$$\begin{aligned} D_i^1 &= \mu \\ D_{ij}^2 &= \frac{1}{2} \sum_l \sigma_{il} \sigma_{lj}^T \end{aligned} \quad (6.9)$$

In the case of anisotropic diffusivity, the diffusivity tensor is defined by a 3×3 matrix. We can understand the geometry of anisotropic diffusion by looking at the eigenvalue decomposition of D .

$$D^2 = \mathbf{X} \mathbf{\Lambda} \mathbf{X}^{-1} \quad (6.10)$$

where $\mathbf{X} = [e_1 e_2 e_3]$, e_i are the eigenvectors of D^2 and $\mathbf{\Lambda} = \begin{bmatrix} \lambda_1 & 0 & 0 \\ 0 & \lambda_2 & 0 \\ 0 & 0 & \lambda_3 \end{bmatrix}$, $\lambda_1, \lambda_2,$

and λ_3 are the eigenvalues of D^2 .

The eigenvalues are real, mutually orthogonal, and positive. When $\lambda_1 = \lambda_2 = \lambda_3$, the diffusion process is considered isotropic and the observable contour of $f(\mathbf{r}, t)$ forms a sphere, as explained previously. In general, the contour of $f(\mathbf{r}, t)$ forms an ellipsoid with the following function

$$\frac{x^2}{\lambda_1^2} + \frac{y^2}{\lambda_2^2} + \frac{z^2}{\lambda_3^2} = 1 \quad (6.11)$$

For the bounded domain, (6.8) can be easily solved, numerically, with the initial condition $f(\mathbf{r}, t_0) = \delta(\mathbf{r} - \mathbf{r}_0)$ and following boundary conditions [Reif 77]

$$f(\mathbf{r}, t) = 0 \quad \text{for absorbing boundaries} \quad (6.12)$$

$$\hat{\mathbf{n}} \cdot \nabla f = 0 \quad \text{for reflecting boundaries} \quad (6.13)$$

where $\hat{\mathbf{n}}$ is the normal vector to the boundary.

The diffusion model does not only include the inner region of the capillary, but also the surrounding tissues, the arterial end, and the proceeding parts of the capillary network which can be observed from Figure (6.5). The coupling between the flow model and the diffusion-convection equations is achieved by implementing domain and boundary conditions as follows:

Domain Configuration

- Capillary inner domain: we use homogenous diffusivity with a convection flux corresponding to the velocity field, \mathbf{u} , calculated in 6.2, i.e., $\boldsymbol{\mu} = \mathbf{u}$ and $\mathbf{D}^2 = DI_3$
- Capillary wall: only convection flux in the radial direction is considered with anisotropic diffusivity with the following eigenvalues

$$\lambda_1 = \beta \cos(\theta),$$

$$\lambda_2 = \beta \sin(\theta), \text{ and}$$

$$\lambda_3 = 0$$

where β is a scaling factor that is a function of pressure difference, i.e. $\beta = \text{sign}(p - p_c)$. This representation of the diffusivity tensor allows diffusion only in the radial direction.

Boundary Configuration

- Capillary inner wall: we use the continuity condition.
- Capillary outer wall: we propose an absorbing boundary condition to enforce absorption of all the particles leaving the capillary to the surrounding tissues.
- Arteriole end: we assume a reflecting boundary in order to prevent all particles from re-entering the arteriole.
- Venule end: we assume an infinite domain with continuity condition in between.

Then, the probability density function is calculated in the proposed geometry using COMSOL Multiphysics. In Figure (6.6) we show the time evolution of the particle pdf inside a capillary segment assuming that the particle starts moving from the arterial end. In order to study the behavior of the capillary network, we study two main probabilities:

1. P_A : The probability of a particle to get absorbed into the surrounding tissues.
2. P_T : The probability of a particle to get transmitted to the proceeding capillary network.

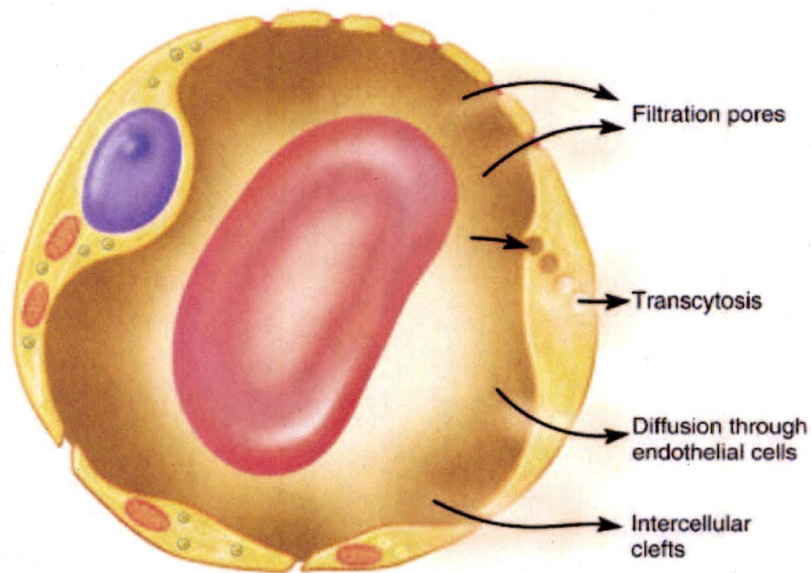


Figure 6.5: Cross section of the capillary showing the different mechanisms of transportation and different capillary boundaries.

In Figure (6.6a), we present P_A as a function of time. Observe that, the probability of absorption increases with time as the particle moves along the capillary segment which reaches an upper bound (saturation) as it moves to the rest of the capillary bed ($t_{sat} \approx 2 * 10^{-5} sec$). The plot in Figure (6.6b) shows the time function of P_T . Similarly, the probability of transmission reaches an upper bound as it moves to the rest of the capillary bed. Moreover, P_T shows a delay response due to the time required by a particle to hit the venule end of the capillary. However, the simulation time required to calculate the previous results, for a simple geometry, is 15965 seconds (4.4 hrs). We expect the computational time required to simulate the whole capillary network to be unreasonably large. In Section 6.4, we propose a novel technique to calculate the absorption and transmission probabilities of a single particle that can efficiently be used for a complex capillary

network.

6.4 Segmentation Model of the Capillary Network

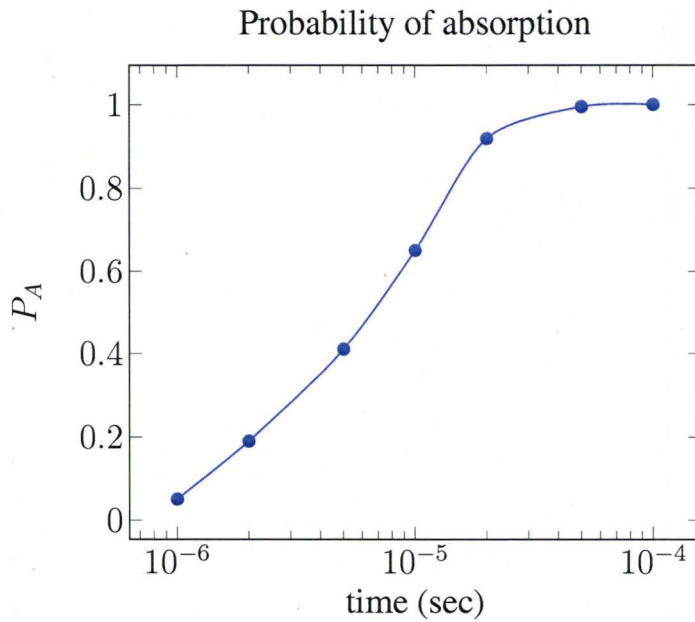
In this section, we propose a time efficient technique, segmentation model (SM), to calculate the aforementioned absorption and transmission probabilities (P_A and P_T , respectively) which can be used for a complex capillary network. The main idea of this technique is breaking the capillary network into smaller sections with pre-defined properties in order to reduce the overall computational time. Ahead, we present the main steps to implement the proposed algorithm:

Step 1: discretization of the capillary into a large number of smaller sections.

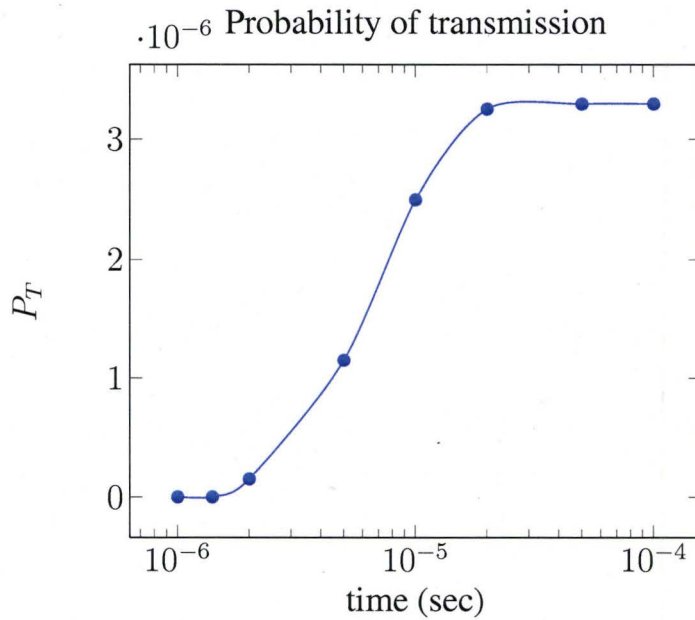
Step 2: calculating the P_A and P_T of each section as a function of pressure.

Step 3: integrating over the capillary network.

First, we start by discretizing the previously introduced capillary segment into n smaller sections, as shown in Figure (6.8). Next, we calculate P_{A_i} and P_{T_i} , namely, the absorption and transmission probabilities within the i^{th} section, where $i = 1, \dots, n$. This is done separately for each section under the same conditions calculated in Section 6.2, i.e., the pressure along each section is set to the values corresponding to those in Figure (6.4). The pressure at the beginning of i^{th} section is defined as p_{i-1} and its pressure drop is Δp_i with p_0 is the maximum pressure at the arteriole end and p_n is the minimum pressure at the venule end. Also, we assume that the diffusive particle starts its movement from the beginning of each section.



(a) Probability of absorption



(b) Probability of transmission

Figure 6.6: Evolution of the probabilities of absorption and transmission of a single particle traveling from the arteriole to a venule via a capillary segment.

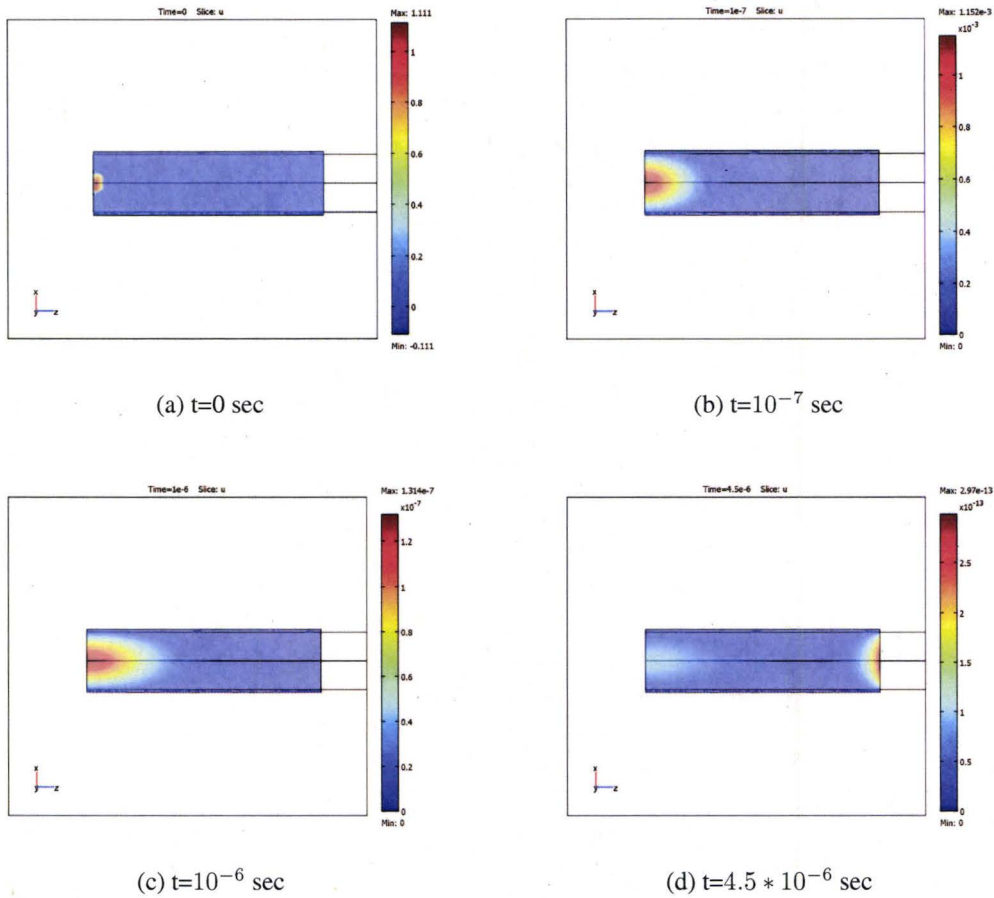


Figure 6.7: Evolution of $f(r, t)$ inside a capillary segment.

In Figures (6.9 and 6.10), we illustrate the probabilities of absorption and transmission, respectively, of each section as a function of capillary blood pressure. The calculations are done for $n = 20$ sections at $1.01\mu sec$. Note that, this relation can also be interpreted to be a function of the capillary length if we assumed a linear dependency of the blood pressure on the capillary length, previously illustrated in Section 6.2. This assumption is valid and will be used in this section as well. As expected, P_{A_i} decreases as moving along the capillary segment since, in principle, the absorption on the capillary walls depends on the pressure difference across the wall, recall (6.4), which decreases as moving towards the

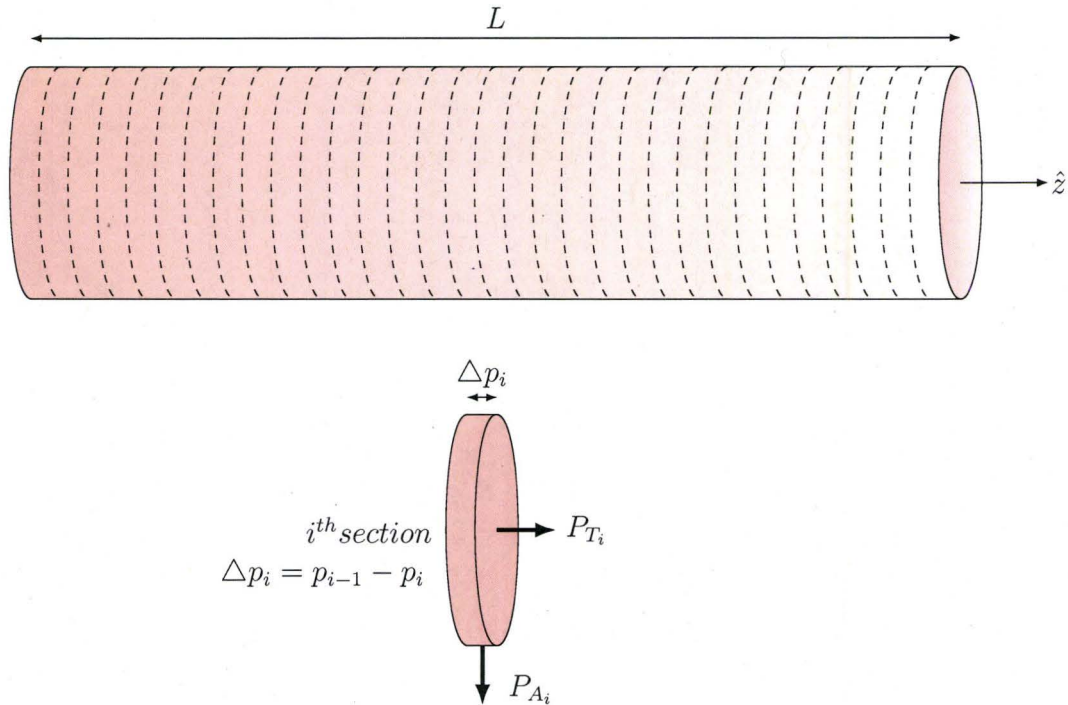


Figure 6.8: Discretization of a capillary segment.

venule end. However, P_{T_i} shows a minima near the middle of the capillary segment since it mainly depends on the axial velocity of the blood which has a minima near the middle of the capillary as well.

In Appendix D, Tables (D.1 and D.2) show the values of P_{A_i,t_j} and P_{T_i,t_j} for 50 sections spanning a pressure domain of $15 - 40 \text{ mmHg}$ with osmotic pressure of 25 mmHg . The calculations are done for 10 time steps.

This discrete representation of the absorption and transmission probabilities of each section is very useful in calculating the total absorption or transmission probabilities for a general capillary segment and hence for a capillary network at different time instances. For better understanding of the importance of Figures (6.9 and 6.10) and Tables (D.1 and D.2),

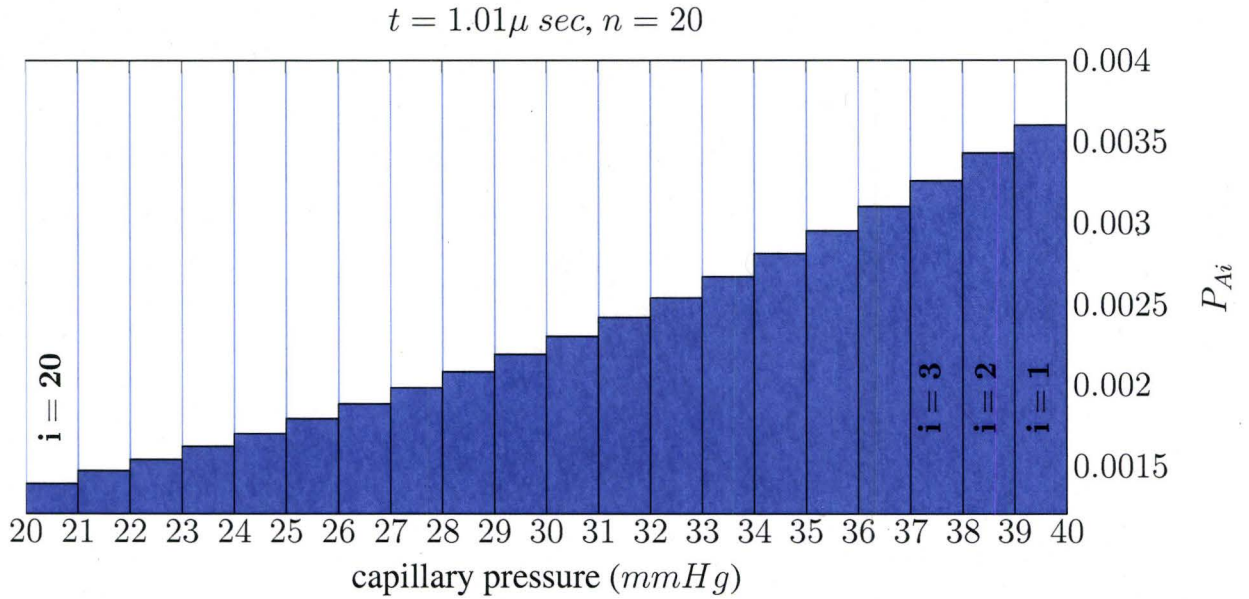


Figure 6.9: Probability of absorption of the i^{th} capillary section, for $i = 1, \dots, n$, as a function of capillary blood pressure.

we show an example of calculating the total absorption and transmission probabilities for a capillary segment consisting of n sections with known starting pressure and length. Also, for simplicity, we assume that the section length is equal to that presented in Figures (6.9 and 6.10). We first define the different probabilities that will be used in the example below.

$P_{A_i,t}$, the absorption probability of the i^{th} section at time t for a particle starting from the same section.

$P_t^{A_i}$, the absorption probability of the i^{th} section at time t for a particle starting from the 1st section.

$P_{tot,t}^{A_i}$, the total absorption probability of the sections $1, \dots, i$ at time t for a particle starting from the 1st section.

$P_{T_i,t}$, the transmission probability of the i^{th} section at time t for a particle starting from the

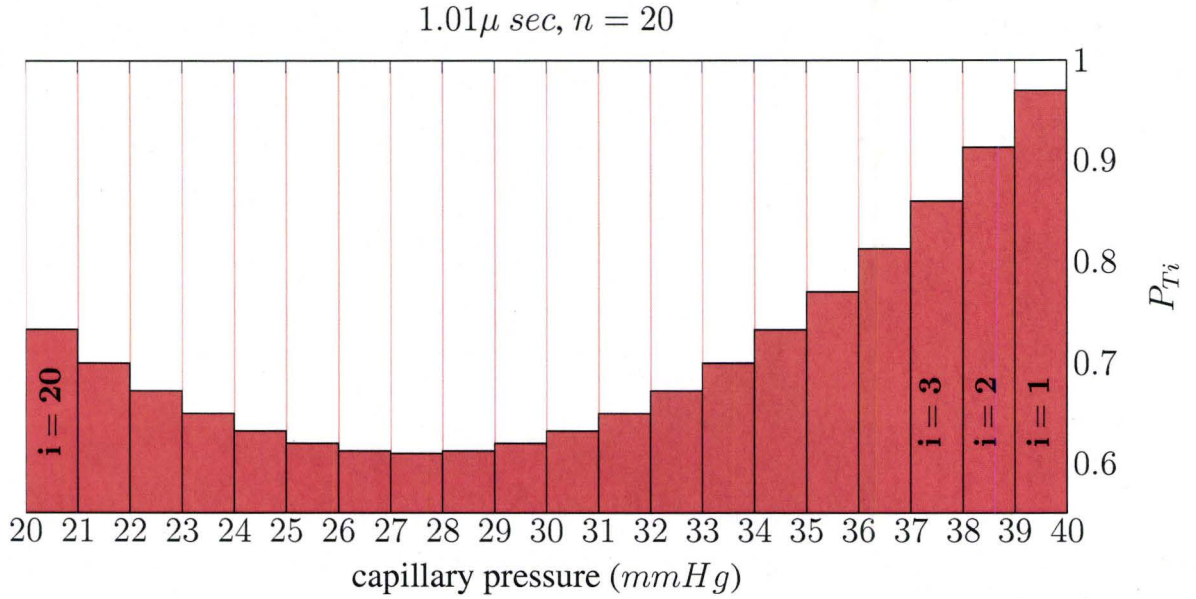


Figure 6.10: Probability of transmission of the i^{th} capillary section, for $i = 1, \dots, n$, as a function of capillary blood pressure.

same section.

$P_{tot,t}^{T_i}$, the total transmission probability from the sections $1, \dots, i$ at time t for a particle starting from the 1^{st} section. Also, equal to $P_t^{T_i}$.

For two successive sections, $P_t^{A_1} = P_{tot,t}^{A_1} = P_{A_1,t}$ and $P_{tot,t}^{T_1} = P_{T_1,t}$, since there are no preceding sections. For the second section, $P_t^{A_2}$ is given by

$$P_t^{A_2} = \int_{t=0}^t \frac{\partial P_{tot,t'}^{T_1}}{\partial t'} P_{A_2,t'} dt' \quad (6.14)$$

where $\frac{\partial P_{tot,t'}^{T_1}}{\partial t'}$ represents the rate of the transmission probability of the 1^{st} section. Since we assume a steady state flow (i.e., $\frac{dp}{dt} = 0$), then $\frac{\partial P_{tot,t'}^{T_1}}{\partial t'} = \frac{dP_{tot,t'}^{T_1}}{dt'}$ and (6.14) can be written as

$$P_t^{A_2} = \int_{t=0}^t P_{A_2,t} dP_{tot,t}^{T_1} \quad (6.15)$$

The discrete form of (6.15) is given by

$$P_{t_k}^{A_2} = \sum_{j=1}^k (P_{tot,t_j}^{T_1} - P_{tot,t_{j-1}}^{T_1}) P_{A_2,t_j} \quad (6.16)$$

and the total absorption probability will be

$$P_{tot,t_k}^{A_2} = P_{t_k}^{A_1} + P_{t_k}^{A_2} \quad (6.17)$$

Similarly, the total transmission probability is

$$P_{tot,t_k}^{T_2} = P_{t_k}^{T_2} = \sum_{j=1}^k (P_{tot,t_j}^{T_1} - P_{tot,t_{j-1}}^{T_1}) P_{T_2,t_j} \quad (6.18)$$

In general, the total probabilities for n sections at time t_k are given by

$$P_{tot,t_k}^{A_n} = \sum_{i=1}^n P_{t_k}^{A_i} \quad (6.19)$$

$$P_{tot,t_k}^{T_i} = P_{t_k}^{T_i} = \sum_{j=1}^k (P_{tot,t_j}^{T_{i-1}} - P_{tot,t_{j-1}}^{T_{i-1}}) P_{T_i,t_j} \quad (6.20)$$

where

$$P_{t_k}^{A_i} = \sum_{j=1}^k (P_{tot,t_j}^{T_{i-1}} - P_{tot,t_{j-1}}^{T_{i-1}}) P_{A_i,t_j} \quad (6.21)$$

In order to validate the proposed algorithm, we illustrate, in Figure (6.11), the total absorption and transmission probabilities for a capillary segment similar to the one studied previously in Section 6.3 and compare our results to the results obtained using the Finite Element solver. It is obvious that the results obtained using the segmentation model are very accurate and close to those obtained by the Finite Element solver. Also, the computational time required for implementing our model (using MATLAB) is $7.8474 * 10^{-2}$ sec which

is greatly less than the time required by the Finite Element solver (4.4 hrs). Moreover, the segmentation algorithm can be easily used to model complex capillary network since it can be divided into smaller sections that will be integrated using the data provided in Tables (D.1 and D.2).

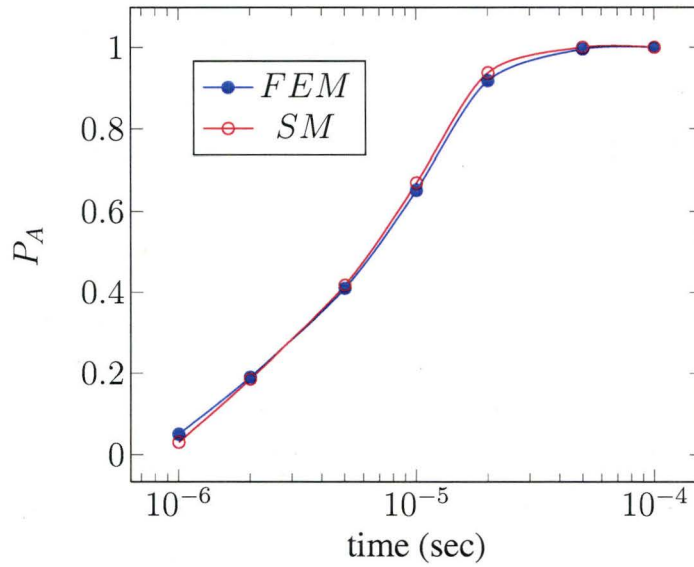
In order to have a handy method for the calculation of $P_{tot,t_j}^{A_n}$, we introduce, in Figure (6.12), a diagram representing the absorption probability for a capillary segment of different lengths using the data presented in Table (D.1). The main advantage of Figure (6.12) is that it can be used to acquire $P_{tot,t_j}^{A_n}$ for a capillary segment with a known pressure terminals. For example, the absorbing probability at time t_j of a capillary segment starts at the arteriole end (40mmHg) with p_o at the end terminal can be calculated directly from the diagram at the point $(\ln(t_j) + 18.4, \frac{49p_o}{15} + 1)$. Further diagrams, for segments starting at different pressure levels, can also be acquired using the data in Tables (D.1 and D.2).

6.5 Modeling the Exchange of Multiple Particles

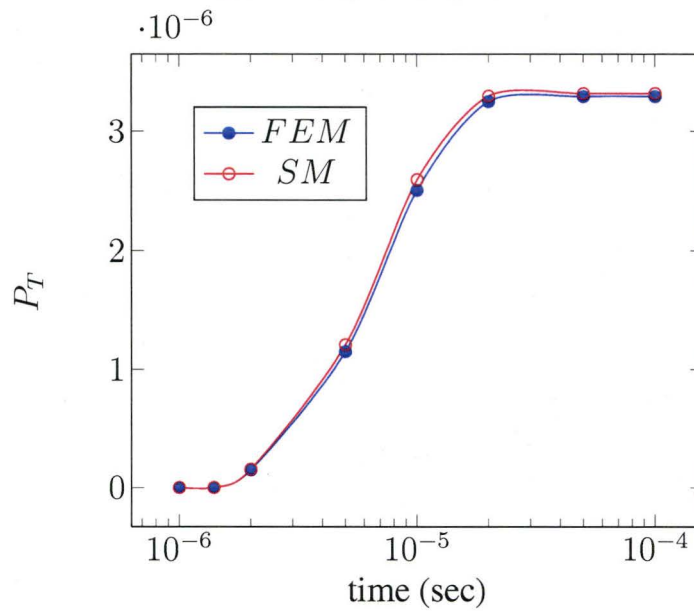
In this section we model the exchange probabilities (absorption and transmission) of multiple particles entering a capillary network. Let n_0 be the initial number of particles entering a capillary network that has an absorbing and transmission probabilities of $P_{A,t_j} \equiv P_{tot,t_j}^{A_n}$ and $P_{T,t_j} \equiv P_{tot,t_j}^{T_n}$, respectively. Hence, the probability that there are n absorbed particles within the network at time t_j becomes

$$P_j(n) = \binom{n_0}{n} P_{A,t_j}^n (1 - P_{A,t_j})^{n_0-n} \quad n = 1, \dots, n_0 \quad (6.22)$$

Similarly, the probability that there are m transmitted particles within the network at time t_j is



(a) Probability of absorption



(b) Probability of transmission

Figure 6.11: Comparison of the Finite Element and Segmentation Methods in calculating P_A and P_T .

$$P_j(m) = \binom{n_0}{m} P_{T,t_j}^m (1 - P_{T,t_j})^{n_0 - m} \quad m = 1, \dots, n_0 \quad (6.23)$$

Finally, The joint probability of n absorbed and m transmitted particles is given by

$$P_j(m, n) = \binom{n_0}{m} \binom{n_0 - m}{n} P_{T,t_j}^m P_{A,t_j}^n (1 - P_{A,t_j} - P_{T,t_j})^{n_0 - m - n} \quad m + n = 1, \dots, n_0 \quad (6.24)$$

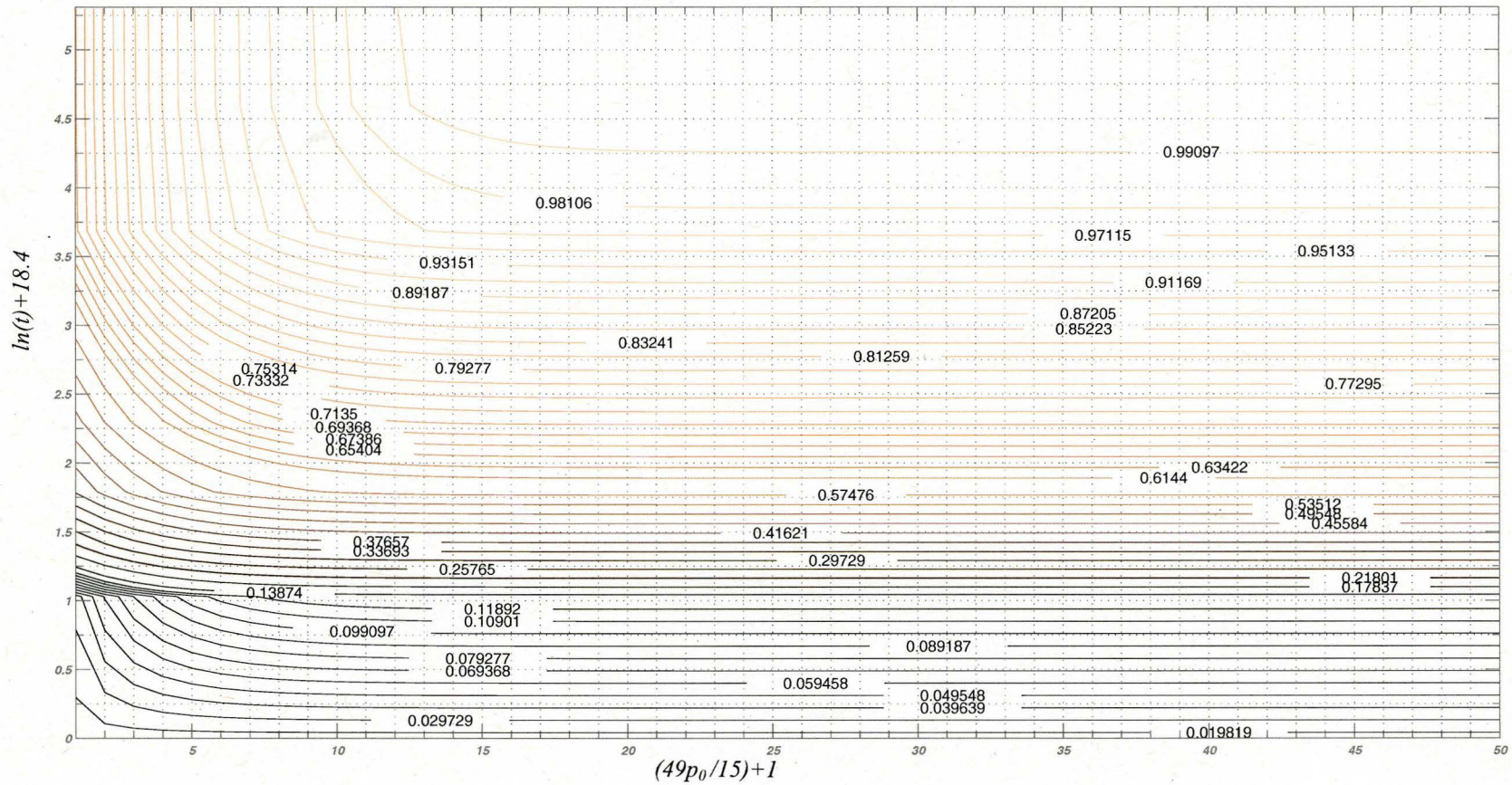


Figure 6.12: Absorbing probability ($P_{tot,t_j}^{A_n}$) of a capillary segment starts at 40mmHg.

6.6 Conclusions

In this chapter we addressed the problem of modeling the exchange process in capillary networks. To model the flow in the capillary plasma, we used Navier-Stokes equations with no-slip walls and no-slip condition. To calculate the absorption and transmission probabilities of a particle in a capillary segment, we implemented Fokker-Planck equations with anisotropic diffusivity in the presence of plasma flow. To achieve computational efficiency, we proposed the Segmentation Model (SM), at which the capillary segment is divided into small sections and the probabilities of absorption and transmission are calculated separately for each section. These probabilities are then used to integrate any general capillary network.

Our approach can be easily applied to any capillary network. For the best of our knowledge, it can be used in different applications such as drug delivery, bacterial clearance, . . . etc.

6.7 Publications

- A. Atalla and A. Jeremic, "*Modeling the Capillary Exchange Using Coupled Stochastic-Navier Stokes Model*", submitted to Physical Review E.
- A. Atalla and A. Jeremic, "*Modeling the Bacterial Clearance in Capillary Network Using Coupled Stochastic-Differential and Navier-Stokes Equations*", COMSOL Conference 2009.

Chapter 7

Concluding Remarks

We have proposed modeling techniques for some diffusion problems and their inverse algorithms. We addressed the problem of localizing the diffusivity disorder in the myocardium using ECG/MCG sensor arrays. The proposed algorithm can be easily extended to account for an arbitrary spatial variation in the diffusivity tensor using a set of *a priori* known basis functions. In addition the parametric shape of the anomaly can be extended to model an arbitrary region using a three-dimensional spatial Fourier transform. An effort should be made to examine the sensitivity of the proposed algorithms to the size of diffusivity difference between “regular” tissue and anomaly as well as the number of the unknown parameters needed to model arbitrary shapes.

For the cases of low source intensity, where the classical model of diffusion fails to provide satisfactory estimates, we proposed a computationally efficient algorithm for source localization using stochastic differential equations. The stochastic model accounts for the random effects which are not accounted for in commonly used classical techniques based

on Fick's law of diffusion. Hence, it provides accurate results when estimating the properties of low intensity sources. Also, we extended our algorithm to account for boundaries and proposed a maximum likelihood estimators for the boundary properties. To the best of our knowledge, this is a first attempt to estimate the absorbing region using stochastic differential equations in the presence of drift. This algorithm can be easily extended to various scenarios consisting of realistic geometries (urban environment, tunnel structures, turbulence etc.), by properly accounting for drift (wind, flow) and boundary conditions. An effort should be done to examine the robustness of the stochastic algorithm. Also, a study of the source intensity limit, at which the classical technique fails, should be done.

We have also addressed the problem of modeling the exchange process in capillary networks. At which, we used a coupled Navier-Stocks and Fokker-Planck equations to construct a computationally efficient algorithm (Segmentation Model - SM) for modeling the absorption and transmission probabilities of particles traveling through a capillary bed. The SM can be used to model complex capillary networks without the need of numerical simulation.

Further research should include the implementation of the SM in drug delivery problems and examine its robustness when applied to different capillary networks. Also, it should be extended to include different blood vessels and surrounding tissues. This would include implementing the different tissue and flow properties.

Appendix A

Solution of the Diffusion Equation

The solution to (2.4) is obtained by using the fundamental solution (i.e. Green's function) along with coordinate transformation. First let us consider the diffusion equation with no advection term that is

$$\frac{\partial c(\mathbf{r}, t)}{\partial t} = \nabla \cdot (\mathcal{K}(c, \mathbf{r}) \nabla c(\mathbf{r}, t)) \quad (\text{A.1})$$

For the isotropic and homogenous media, the above equation can be written in the following form

$$\frac{\partial c(\mathbf{r}, t)}{\partial t} = \mathcal{K} \nabla^2 c(\mathbf{r}, t) \quad (\text{A.2})$$

We show that the Green's function for the diffusion equation

$$G(\mathbf{r}, t) = \frac{1}{6\mathcal{K}\pi(t-t_0)} \exp\left\{-\frac{\|\mathbf{r}-\mathbf{r}_0\|^2}{6\mathcal{K}(t-t_0)}\right\} \quad (\text{A.3})$$

satisfies A.2 and behaves like a delta function at $t = t_0$.

Plugging the Green's function into the diffusion equation, (A.2), gives on both sides

$$\frac{\partial G(\mathbf{r}, t)}{\partial t} = -\frac{1}{t}G(\mathbf{r}, t) + \frac{\|\mathbf{r} - \mathbf{r}_0\|^2}{6\mathcal{K}t^2}G(\mathbf{r}, t) = \mathcal{K}\nabla^2 G(\mathbf{r}, t) \quad (\text{A.4})$$

verifying that it is a solution to the equation.

As $t \rightarrow t_0$, for $\mathbf{r} \neq \mathbf{r}_0$, the argument of the exponent goes to $-\infty$, and $G(\mathbf{r}, t) \rightarrow 0$. For $\mathbf{r} = \mathbf{r}_0$, it goes to infinity as $t \rightarrow \infty$. For a general initial condition $c(\mathbf{r}, 0) = g(\mathbf{r})$, the solution of the diffusion equation is

$$c(\mathbf{r}, t) = \int g(\mathbf{r}^*)G(\mathbf{r} - \mathbf{r}^*, t)d_3\mathbf{r}^* \quad (\text{A.5})$$

Now, lets account for the convection term and substitute the coordinate transformation for the moving reference frame into (A.1). The coordinate transformation for the moving system is

$$\hat{\mathbf{r}} = \mathbf{r} - (\mathbf{r}_0 + \nu t) \quad (\text{A.6})$$

$$\hat{t} = t - t_0 \quad (\text{A.7})$$

and this can be substituted into (2.4) using the chain rule we can derive

$$\frac{\partial c(\hat{\mathbf{r}}, \hat{t})}{\partial \hat{t}} = \mathcal{K}\nabla^2 c(\hat{\mathbf{r}}, \hat{t}) \quad (\text{A.8})$$

This is just the diffusion equation in the coordinates $\hat{\mathbf{r}}$ and \hat{t} with solution for an instantaneous point source of

$$G(\hat{\mathbf{r}}, \hat{t}) = \frac{1}{6\mathcal{K}\pi\hat{t}} \exp\left\{-\frac{(\hat{\mathbf{r}})^2}{6\mathcal{K}\hat{t}}\right\} \quad (\text{A.9})$$

Converting the solution back to \mathbf{r} and t coordinates

$$G(\mathbf{r}, t) = \frac{1}{6\mathcal{K}\pi(t-t_0)} \exp \left\{ -\frac{\|\mathbf{r} - (\mathbf{r}_0 + \nu(t-t_0))\|^2}{6\mathcal{K}(t-t_0)} \right\} \quad (\text{A.10})$$

(A.5) can be used then to calculate the general solution for $c(\mathbf{r}, 0) = g(\mathbf{r})$.

Appendix B

Computation of the Classical Estimators for \bar{c}_0 and \bar{r}_0

We compute the estimators \bar{c}_0 and \bar{r}_0 that maximize (2.13).

The derivative of (2.13) with respect to c_0 is given by

$$\frac{\partial \log(\mathcal{L})}{\partial c_0} = \frac{1}{\sigma^2} \sum_{k=1}^p (\mathbf{y}_k - c_0 \mathbf{a}_k(\theta))^T \mathbf{a}_k(\theta) \quad (\text{B.1})$$

In order to maximize (2.13), let

$$\frac{\partial \log(\mathcal{L})}{\partial c_0} = 0 \quad (\text{B.2})$$

Which leads to

$$\sum_{k=1}^p \mathbf{y}_k^T \mathbf{a}_k(\theta) = c_0 \sum_{k=1}^p \mathbf{a}_k(\theta)^T \mathbf{a}_k(\theta) \quad (\text{B.3})$$

And

$$c_0 = \frac{\sum_{k=1}^p \mathbf{y}_k^T \mathbf{a}_k(\theta)}{\sum_{k=1}^p \|\mathbf{a}_k(\theta)\|^2} \quad (\text{B.4})$$

For the computation of $\bar{\mathbf{r}}_0$, we take the derivative of (2.13) with respect to \mathbf{r}_0

$$\frac{\partial \log(\mathcal{L})}{\partial \mathbf{r}_0} = \frac{1}{\sigma^2} \sum_{k=1}^p \frac{(\mathbf{y}_k - c_0 \mathbf{a}_k(\theta))^T \partial \mathbf{a}_k(\theta)}{\|(\mathbf{y}_k - c_0 \mathbf{a}_k(\theta))\|} \frac{\partial \mathbf{a}_k(\theta)}{\partial \mathbf{r}_0} \quad (\text{B.5})$$

Let

$$\frac{\partial \log(\mathcal{L})}{\partial \mathbf{r}_0} = 0 \quad (\text{B.6})$$

Which leads to

$$\sum_{k=1}^p \frac{2}{4\kappa(t_k - t_0)} \frac{(\mathbf{y}_k - c_0 \mathbf{a}_k(\theta))^T \mathcal{R} \mathbf{a}_k(\theta)}{\|(\mathbf{y}_k - c_0 \mathbf{a}_k(\theta))\|} = 0 \quad (\text{B.7})$$

where \mathcal{R} is a diagonal matrix that holds the differences between the measurement point and \mathbf{r}_0 , as follows

$$\mathcal{R} = \begin{bmatrix} \mathbf{r}_1 - \mathbf{r}_0 & 0 & \dots & 0 \\ 0 & \mathbf{r}_2 - \mathbf{r}_0 & \dots & 0 \\ \vdots & \vdots & \ddots & \vdots \\ 0 & 0 & \dots & \mathbf{r}_m - \mathbf{r}_0 \end{bmatrix} \quad (\text{B.8})$$

Then, estimator $\bar{\mathbf{r}}_0$ that maximizes (2.13) is given by

$$\bar{\mathbf{r}}_0 = \arg \min_{\mathbf{r}_0} \sum_{k=1}^p \frac{1}{(t_k - t_0)} \frac{(\mathbf{y}_k - c_0 \mathbf{a}_k(\theta))^T \mathcal{R} \mathbf{a}_k(\theta)}{\|(\mathbf{y}_k - c_0 \mathbf{a}_k(\theta))\|} \quad (\text{B.9})$$

Appendix C

Derivation of the Likelihood Function in the Presence of Noise

In the presence of noise, the measurement vector (y_j) is given by

$$y_j = \mathbf{n}_j(\psi) + \mathbf{e}_j \quad (\text{C.1})$$

where \mathbf{n}_j is the model predicted data vector, \mathbf{e}_j is the noise vector and ψ is the estimation parameter vector.

We assume that the model vector and the noise vector are statistically independent (uncorrelated), hence, the probability mass function of the measurement vector y_j becomes the convolution of the probability mass functions of the actual data vector, i.e., Equation (4.13), and the measurement noise vector. The measurement noise is assumed to have a multivariate Poisson distribution, given by

$$P(e_1, \dots, e_m) = \exp\left(-\sum_{i=1}^m \lambda_i\right) \prod_{i=1}^m \frac{\lambda_i^{e_i}}{e_i!} \sum_{i=0}^s \prod_{j=1}^m \binom{e_j}{i} i! \left(\frac{\lambda_0}{\prod_{i=1}^m \lambda_i}\right)^i \quad (\text{C.2})$$

where $s = \min(e_1, \dots, e_m)$ and λ_0 is the covariance between all the pairs of the error vector.

Since we assume the error vector to be uncorrelated (i.e. $\lambda_0 = 0$), (C.2) reduces to

$$P(e_1, \dots, e_m) = \exp\left(-\sum_{i=1}^m \lambda_i\right) \prod_{i=1}^m \frac{\lambda_i^{e_i}}{e_i!} \quad (\text{C.3})$$

Also, we assume the error to be i.i.d (i.e. $\lambda_1 = \dots = \lambda_m = \lambda$), which leads to the following simplification

$$P(e_1, \dots, e_m) = e^{-m\lambda} \prod_{i=1}^m \frac{\lambda^{e_i}}{e_i!} \quad (\text{C.4})$$

Hence, the joint PMF of the measurement vector is given by

$$P(y_{1j}, \dots, y_{mj}) = P(n_{1j}, \dots, n_{mj}) * P(e_{1j}, \dots, e_{mj}) \quad (\text{C.5})$$

Which leads to

$$P(y_{1j}, \dots, y_{mj}) = \sum_{\tau_1=0}^{y_{1j}} \dots \sum_{\tau_m=0}^{y_{mj}} e^{-m\lambda} \binom{n_0}{\tau_1 \dots \tau_m} \cdot \left(1 - \sum_{i=1}^m P_{j, \Delta_i}\right)^{n_0 - \sum_{i=1}^m \tau_i} \prod_{i=1}^m \frac{\lambda^{y_{ij} - \tau_i}}{(y_{ij} - \tau_i)!} P_{j, \Delta_i}^{\tau_i} \quad (\text{C.6})$$

Appendix D

Values of P_{A_i,t_j} and P_{T_i,t_j} for 50

Capillary Sections

Below, in Tables (D.1 and D.2), we list the values of P_{A_i,t_j} and P_{T_i,t_j} for 50 sections spanning a pressure domain of 15 – 40 *mmHg* with osmotic pressure of 25 *mmHg*. The calculations are done for 10 time steps.

		$P_{A_i,t}$									
		1	2.8	3	4	6	10	20	40	100	200
i	$t * 10^{-8} sec$										
1	1	0.09582	0.8145	0.8624	0.9007	0.9295	0.939	0.9486	0.9534	0.9579	0.9582
2	2	0.0935	0.7948	0.8415	0.8789	0.907	0.9163	0.9257	0.9303	0.9347	0.935
3	3	0.09126	0.7757	0.8213	0.8578	0.8852	0.8943	0.9035	0.908	0.9123	0.9126
4	4	0.0891	0.7573	0.8019	0.8375	0.8643	0.8732	0.8821	0.8865	0.8907	0.891
5	5	0.08702	0.7397	0.7832	0.818	0.8441	0.8528	0.8615	0.8658	0.8699	0.8702
6	6	0.08502	0.7227	0.7652	0.7992	0.8247	0.8332	0.8417	0.8459	0.8499	0.8502
7	7	0.0831	0.7064	0.7479	0.7811	0.8061	0.8144	0.8227	0.8268	0.8308	0.831
8	8	0.08126	0.6907	0.7313	0.7638	0.7882	0.7963	0.8045	0.8085	0.8124	0.8126
9	9	0.0795	0.6757	0.7155	0.7473	0.7712	0.7791	0.7871	0.791	0.7948	0.795
10	10	0.07782	0.6615	0.7004	0.7315	0.7549	0.7626	0.7704	0.7743	0.778	0.7782
11	11	0.07622	0.6479	0.686	0.7165	0.7393	0.747	0.7546	0.7584	0.762	0.7622
12	12	0.0747	0.635	0.6723	0.7022	0.7246	0.7321	0.7395	0.7433	0.7468	0.747
13	13	0.07326	0.6227	0.6593	0.6886	0.7106	0.7179	0.7253	0.7289	0.7324	0.7326
14	14	0.0719	0.6111	0.6471	0.6759	0.6974	0.7046	0.7118	0.7154	0.7188	0.719
15	15	0.07062	0.6003	0.6356	0.6638	0.685	0.6921	0.6991	0.7027	0.706	0.7062

		$P_{A_i,t}$								
		1	2.8	3	4	6	10	20	40	100
i	$t * 10^{-8} sec$									
16	0.06942	0.5901	0.6248	0.6525	0.6734	0.6803	0.6873	0.6907	0.694	0.6942
17	0.0683	0.5806	0.6147	0.642	0.6625	0.6693	0.6762	0.6796	0.6828	0.683
18	0.06726	0.5717	0.6053	0.6322	0.6524	0.6591	0.6659	0.6692	0.6724	0.6726
19	0.0663	0.5636	0.5967	0.6232	0.6431	0.6497	0.6564	0.6597	0.6628	0.663
20	0.06542	0.5561	0.5888	0.6149	0.6346	0.6411	0.6477	0.6509	0.654	0.6542
21	0.06462	0.5493	0.5816	0.6074	0.6268	0.6333	0.6397	0.643	0.646	0.6462
22	0.0639	0.5432	0.5751	0.6007	0.6198	0.6262	0.6326	0.6358	0.6388	0.639
23	0.06326	0.5377	0.5693	0.5946	0.6136	0.6199	0.6263	0.6294	0.6324	0.6326
24	0.0627	0.533	0.5643	0.5894	0.6082	0.6145	0.6207	0.6239	0.6268	0.627
25	0.06222	0.5289	0.56	0.5849	0.6035	0.6098	0.616	0.6191	0.622	0.6222
26	0.06182	0.5255	0.5564	0.5811	0.5997	0.6058	0.612	0.6151	0.618	0.6182
27	0.0615	0.5228	0.5535	0.5781	0.5966	0.6027	0.6089	0.6119	0.6148	0.615
28	0.06126	0.5207	0.5513	0.5758	0.5942	0.6003	0.6065	0.6095	0.6124	0.6126
29	0.0611	0.5193	0.5499	0.5743	0.5927	0.5988	0.6049	0.6079	0.6108	0.611
30	0.06102	0.5187	0.5492	0.5736	0.5919	0.598	0.6041	0.6071	0.61	0.6102

		$P_{A_i,t}$									
		1	2.8	3	4	6	10	20	40	100	200
i	$t * 10^{-8} sec$										
31		0.06102	0.5187	0.5492	0.5736	0.5919	0.598	0.6041	0.6071	0.61	0.6102
32		0.0611	0.5193	0.5499	0.5743	0.5927	0.5988	0.6049	0.6079	0.6108	0.611
33		0.06126	0.5207	0.5513	0.5758	0.5942	0.6003	0.6065	0.6095	0.6124	0.6126
34		0.0615	0.5227	0.5535	0.5781	0.5966	0.6027	0.6089	0.6119	0.6148	0.615
35		0.06182	0.5255	0.5564	0.5811	0.5997	0.6058	0.612	0.6151	0.618	0.6182
36		0.06222	0.5289	0.56	0.5849	0.6035	0.6098	0.616	0.6191	0.622	0.6222
37		0.0627	0.533	0.5643	0.5894	0.6082	0.6145	0.6207	0.6239	0.6268	0.627
38		0.06326	0.5377	0.5693	0.5946	0.6136	0.6199	0.6263	0.6294	0.6324	0.6326
39		0.0639	0.5432	0.5751	0.6007	0.6198	0.6262	0.6326	0.6358	0.6388	0.639
40		0.06462	0.5493	0.5816	0.6074	0.6268	0.6333	0.6397	0.643	0.646	0.6462
41		0.06542	0.5561	0.5888	0.6149	0.6346	0.6411	0.6477	0.6509	0.654	0.6542
42		0.0663	0.5636	0.5967	0.6232	0.6431	0.6497	0.6564	0.6597	0.6628	0.663
43		0.06726	0.5717	0.6053	0.6322	0.6524	0.6591	0.6659	0.6692	0.6724	0.6726
44		0.0683	0.5805	0.6147	0.642	0.6625	0.6693	0.6762	0.6796	0.6828	0.683
45		0.06942	0.5901	0.6248	0.6525	0.6734	0.6803	0.6873	0.6907	0.694	0.6942

		$P_{A_i,t}$									
		$t * 10^{-8} sec$	1	2.8	3	4	6	10	20	40	100
i											
46		0.07062	0.6003	0.6356	0.6638	0.685	0.6921	0.6991	0.7027	0.706	0.7062
47		0.0719	0.6111	0.6471	0.6759	0.6974	0.7046	0.7118	0.7154	0.7188	0.719
48		0.07326	0.6227	0.6593	0.6886	0.7106	0.7179	0.7253	0.7289	0.7324	0.7326
49		0.0747	0.635	0.6723	0.7022	0.7246	0.7321	0.7395	0.7433	0.7468	0.747
50		0.07622	0.6479	0.686	0.7165	0.7393	0.747	0.7546	0.7584	0.762	0.7622

Table D.1: P_{A_i,t_j} for 50 sections and 10 time steps.

$t * 10^{-8} sec$		$P_{T_i,t}$									
		1	2.8	3	4	6	10	20	40	100	200
1		0.01384	0.03461	0.06922	0.2077	0.3807	0.4845	0.5884	0.6887	0.692	0.6922
2		0.01358	0.03394	0.06789	0.2037	0.3734	0.4752	0.577	0.6755	0.6787	0.6789
3		0.01332	0.03329	0.06658	0.1997	0.3662	0.4661	0.5659	0.6625	0.6656	0.6658
4		0.01306	0.03265	0.0653	0.1959	0.3591	0.4571	0.555	0.6497	0.6528	0.653
5		0.01281	0.03202	0.06404	0.1921	0.3522	0.4483	0.5444	0.6372	0.6402	0.6404
6		0.01256	0.0314	0.06281	0.1884	0.3455	0.4397	0.5339	0.625	0.6279	0.6281
7		0.01232	0.0308	0.0616	0.1848	0.3388	0.4312	0.5236	0.6129	0.6158	0.616
8		0.01208	0.03021	0.06041	0.1812	0.3323	0.4229	0.5135	0.6011	0.604	0.6041
9		0.01185	0.02963	0.05925	0.1778	0.3259	0.4148	0.5036	0.5896	0.5923	0.5925
10		0.01162	0.02906	0.05811	0.1743	0.3196	0.4068	0.4939	0.5782	0.5809	0.5811
11		0.0114	0.0285	0.05699	0.171	0.3135	0.3989	0.4844	0.5671	0.5698	0.5699
12		0.01118	0.02795	0.0559	0.1677	0.3074	0.3913	0.4751	0.5562	0.5588	0.559
13		0.01096	0.02741	0.05482	0.1645	0.3015	0.3837	0.466	0.5455	0.548	0.5482
14		0.01075	0.02688	0.05376	0.1613	0.2957	0.3764	0.457	0.535	0.5375	0.5376
15		0.01055	0.02636	0.05273	0.1582	0.29	0.3691	0.4482	0.5247	0.5271	0.5273

		$P_{A_i,t}$									
		1	2.8	3	4	6	10	20	40	100	200
i	$t * 10^{-8} sec$										
16		0.01034	0.02586	0.05171	0.1551	0.2844	0.362	0.4396	0.5146	0.517	0.5171
17		0.01014	0.02536	0.05072	0.1522	0.279	0.355	0.4311	0.5047	0.507	0.5072
18		0.009949	0.02487	0.04974	0.1492	0.2736	0.3482	0.4228	0.4949	0.4973	0.4974
19		0.009757	0.02439	0.04879	0.1464	0.2683	0.3415	0.4147	0.4854	0.4877	0.4879
20		0.009569	0.02392	0.04785	0.1435	0.2632	0.3349	0.4067	0.4761	0.4783	0.4785
21		0.009385	0.02346	0.04692	0.1408	0.2581	0.3285	0.3989	0.4669	0.4691	0.4692
22		0.009204	0.02301	0.04602	0.1381	0.2531	0.3222	0.3912	0.4579	0.4601	0.4602
23		0.009027	0.02257	0.04514	0.1354	0.2482	0.316	0.3837	0.4491	0.4512	0.4514
24		0.008853	0.02213	0.04427	0.1328	0.2435	0.3099	0.3763	0.4405	0.4425	0.4427
25		0.008683	0.02171	0.04341	0.1302	0.2388	0.3039	0.369	0.432	0.434	0.4341
26		0.008516	0.02129	0.04258	0.1277	0.2342	0.2981	0.3619	0.4237	0.4257	0.4258
27		0.008352	0.02088	0.04176	0.1253	0.2297	0.2923	0.355	0.4155	0.4175	0.4176
28		0.008191	0.02048	0.04096	0.1229	0.2253	0.2867	0.3481	0.4075	0.4094	0.4096
29		0.008033	0.02008	0.04017	0.1205	0.2209	0.2812	0.3414	0.3997	0.4016	0.4017
30		0.007879	0.0197	0.03939	0.1182	0.2167	0.2758	0.3348	0.392	0.3938	0.3939

		$P_{A_i,t}$									
		1	2.8	3	4	6	10	20	40	100	200
i	$t * 10^{-8} sec$										
31	0.007727	0.01932	0.03864	0.1159	0.2125	0.2705	0.3284	0.3844	0.3862	0.3864	
32	0.007578	0.01895	0.03789	0.1137	0.2084	0.2652	0.3221	0.377	0.3788	0.3789	
33	0.007433	0.01858	0.03716	0.1115	0.2044	0.2601	0.3159	0.3698	0.3715	0.3716	
34	0.007289	0.01822	0.03645	0.1093	0.2005	0.2551	0.3098	0.3627	0.3644	0.3645	
35	0.007149	0.01787	0.03575	0.1072	0.1966	0.2502	0.3038	0.3557	0.3573	0.3575	
36	0.007012	0.01753	0.03506	0.1052	0.1928	0.2454	0.298	0.3488	0.3505	0.3506	
37	0.006877	0.01719	0.03438	0.1031	0.1891	0.2407	0.2923	0.3421	0.3437	0.3438	
38	0.006744	0.01686	0.03372	0.1012	0.1855	0.236	0.2866	0.3355	0.3371	0.3372	
39	0.006614	0.01654	0.03307	0.09922	0.1819	0.2315	0.2811	0.3291	0.3306	0.3307	
40	0.006487	0.01622	0.03244	0.09731	0.1784	0.227	0.2757	0.3227	0.3243	0.3244	
41	0.006362	0.01591	0.03181	0.09543	0.175	0.2227	0.2704	0.3165	0.318	0.3181	
42	0.00624	0.0156	0.0312	0.0936	0.1716	0.2184	0.2652	0.3104	0.3119	0.312	
43	0.00612	0.0153	0.0306	0.09179	0.1683	0.2142	0.2601	0.3044	0.3059	0.306	
44	0.006002	0.015	0.03001	0.09003	0.165	0.2101	0.2551	0.2986	0.3	0.3001	
45	0.005886	0.01472	0.02943	0.08829	0.1619	0.206	0.2502	0.2928	0.2942	0.2943	

		$P_{T_i,t}$									
		1	2.8	3	4	6	10	20	40	100	200
i	$t * 10^{-8} sec$										
46		0.005773	0.01443	0.02886	0.08659	0.1588	0.2021	0.2453	0.2872	0.2886	0.2886
47		0.005662	0.01415	0.02831	0.08493	0.1557	0.1982	0.2406	0.2817	0.283	0.2831
48		0.005553	0.01388	0.02776	0.08329	0.1527	0.1943	0.236	0.2763	0.2776	0.2776
49		0.005446	0.01361	0.02723	0.08169	0.1498	0.1906	0.2315	0.2709	0.2722	0.2723
50		0.005341	0.01335	0.02671	0.08012	0.1469	0.1869	0.227	0.2657	0.267	0.2671

Table D.2: P_{T_i,t_j} for 50 sections and 10 time steps.

Bibliography

- [Arapis 06] M. Arapis & J. Gao. *Empirical comparisons in short-term interest rate models using nonparametric methods*. Journal of Financial Econometrics, vol. 4, no. 2, pages 310–345, 2006.
- [Baillet 01] S. Baillet, JC Mosher & RM Leahy. *Electromagnetic brain mapping*. IEEE Signal processing magazine, vol. 18, no. 6, pages 14–30, 2001.
- [Ball 93] C.A. Ball & A. Roma. *A jump diffusion model for the European Monetary System*. Journal of International Money and finance, vol. 12, no. 5, pages 475–492, 1993.
- [Bashkansky 97] M. Bashkansky, MD Duncan, M. Kahn, D. Lewis III & J. Reintjes. *Subsurface defect detection in ceramics by high-speed high-resolution optical coherent tomography*. Optics letters, vol. 22, no. 1, pages 61–63, 1997.
- [Biddle 00] V. Biddle & G. Parker. *Chemistry: Precision and design*. Pensacola Christian College, second edition, 2000.

- [Briggs 73] GA Briggs. *Diffusion estimation for small emissions, in environmental research laboratories*. Environmental research laboratories air resources atmospheric turbulence and diffusion laboratory, 1973.
- [Cannon 32] P.R. Cannon, FL Sullivan & EF Neckermann. *Conditions influencing the disappearance of living bacteria from the blood stream*. Journal of Experimental Medicine, vol. 55, no. 1, pages 121–137, 1932.
- [Chan 07] R.H. Chan & K. Chen. *Multilevel algorithm for a Poisson noise removal model with total-variation regularization*. International Journal of Computer Mathematics, vol. 84, no. 8, pages 1183–1198, 2007.
- [Dargatz 06] C. Dargatz, V. Georgescu & L. Held. *Stochastic modelling of the spatial spread of influenza in Germany*. Austrian Journal of Statistics, vol. 35, no. 1, pages 5–20, 2006.
- [Dhariwal 04] A. Dhariwal, G. Sukhatme & A. Requicha. *Bacterium-inspired robots for environmental monitoring*. In IEEE International Conference on Robotics and Automation, volume 2, pages 1436–1443. Citeseer, 2004.
- [Di Miscia] O. Di Miscia. Estimation of continuous-time interest rate models: a nonparametric approach. CAF, Centre for Analytical Finance.
- [di Miscia 04] O. di Miscia. *Nonparametric estimation of diffusion process: a closer look*. Centre for Analytical Finance, University of Aarhus, Aarhus School of Business. Rapport technique, Working Paper Series, 2004.

- [Doerschuk 00] C.M. Doerschuk. *Leukocyte trafficking in alveoli and airway passages*. Respiratory Research, vol. 1, no. 3, page 136, 2000.
- [Doornbos 99] RMP Doornbos, R. Lang, MC Aalders, FW Cross & H. Sterenborg. *The determination of in vivo human tissue optical properties and absolute chromophore concentrations using spatially resolved steady-state diffuse reflectance spectroscopy*. Physics in medicine and biology, vol. 44, pages 967–982, 1999.
- [Drazer 01] G. Drazer & J. Koplik. *Tracer dispersion in two-dimensional rough fractures*. Physical Review E, vol. 63, no. 5, page 56104, 2001.
- [Egan 72] B.A. Egan & J.R. Mahoney. *Numerical modeling of advection and diffusion of urban area source pollutants*. Journal of Applied Meteorology, vol. 11, no. 2, pages 312–322, 1972.
- [Einstein 56] A. Einstein. *Investigations on the Theory of the Brownian Movement*. Dover Publications, first edition, 1956.
- [El-Shahed 04] M. El-Shahed. *Blood flow in a capillary with permeable wall*. Physica A: Statistical Mechanics and its Applications, vol. 338, no. 3-4, pages 544–558, 2004.
- [Elshahed 04] M. Elshahed. *Blood flow in capillary under starling hypothesis*. Applied Mathematics and Computation, vol. 149, no. 2, pages 431–439, 2004.

- [Farrell 92] T.J. Farrell, M.S. Patterson & B. Wilson. *A diffusion theory model of spatially resolved, steady-state diffuse reflectance for the noninvasive determination of tissue optical properties in vivo*. Med. Phys, vol. 19, no. 4, pages 879–888, 1992.
- [Fitzhugh 61] R. Fitzhugh. *Impulses and physiological states in theoretical models of nerve membrane*. Biophysical Journal, vol. 1, no. 6, pages 445–466, 1961.
- [Gabriel 96a] C. Gabriel. *Compilation of the Dielectric Properties of Body Tissues at RF and Microwave Frequencies.*, 1996.
- [Gabriel 96b] C. Gabriel, S. Gabriel & E. Corthout. *The dielectric properties of biological tissues: I. Literature survey*. Physics in medicine and biology, vol. 41, no. 11, pages 2231–2250, 1996.
- [Geselowitz 70] D. Geselowitz. *On the magnetic field generated outside an inhomogeneous volume conductor by internal current sources*. IEEE Transactions on Magnetics, vol. 6, no. 2, pages 346–347, 1970.
- [Green 64] G.M. Green & E.H. Kass. *Factors influencing the clearance of bacteria by the lung*. Journal of Clinical Investigation, vol. 43, no. 4, page 769, 1964.
- [Grill 94] W.M. Grill & J. Thomas Mortimer. *Electrical properties of implant encapsulation tissue*. Annals of biomedical engineering, vol. 22, no. 1, pages 23–33, 1994.

- [Gulrajani 98] R.M. Gulrajani. Bioelectricity and biomagnetism. Wiley New York, 1998.
- [Haberkoorn 82] R. Haberkoorn & D. Ruben. *A two-dimensional nuclear Overhauser experiment with pure absorption phase in four quadrants*. Journal of Magnetic Resonance, vol. 48, no. 286, pages 286–292, 1982.
- [Han 07] X.H. Han, Y.W. Chen, K. Kitamura, A. Ishikawa, Y. Inoue, K. Shibata, Y. Mishina & Y. Mukuta. *An ICA Based Noise Reduction for PET Reconstructed Images*. In Proceedings of the Third International Conference on International Information Hiding and Multimedia Signal Processing (IIH-MSP 2007)-Volume 01, pages 113–116. IEEE Computer Society Washington, DC, USA, 2007.
- [Hanson 04] F.B. Hanson, J.J. Westman & Z. Zhu. *Multinomial maximum likelihood estimation of market parameters for stock jump-diffusion models*. In Mathematics of finance: Proceedings of an AMS-IMS-SIAM Joint Summer Research Conference on Mathematics of Finance, June 22-26, 2003, Snowbird, Utah, volume 351, page 155. AMS Bookstore, 2004.
- [Holman 04] J.D. Holman, K.G. Burnett & L.E. Burnett. *Effects of hypercapnic hypoxia on the clearance of Vibrio campbellii in the Atlantic blue crab, Callinectes sapidus Rathbun*. Biological bulletin, pages 188–196, 2004.
- [Hull] J.C. Hull. Options, futures, and other derivatives.

- [Ishida 97] H. Ishida, T. Nakamoto & T. Moriizumi. *Remote sensing and localization of gas/odor source and distribution using mobile sensing system*. In Solid State Sensors and Actuators, 1997. TRANSDUCERS'97 Chicago., 1997 International Conference on, volume 1, 1997.
- [Ishida 01] H. Ishida, T. Nakamoto, T. Moriizumi, T. Kikas & J. Janata. *Plume-tracking robots: A new application of chemical sensors*. Biological Bulletin, vol. 200, no. 2, pages 222–226, 2001.
- [Jeremic 98] A. Jeremic & A. Nehorai. *Design of Chemical Sensor Arrays for Monitoring Disposal Sites on the Ocean Floor*. IEEE Journal of Oceanic Engineering, vol. 23, no. 4, pages 334–343, June 1998.
- [Jeremic 00] A. Jeremic & A. Nehorai. *Landmine Detection and Localization Using Chemical Sensor Array Processing*. IEEE Transactions on Signal Processing, vol. 48, no. 5, pages 1295–1305, May 2000.
- [Jiang 97] G.J. Jiang & J.L. Knight. *A nonparametric approach to the estimation of diffusion processes, with an application to a short-term interest rate model*. Econometric Theory, pages 615–645, 1997.
- [Jossinet 96] J. Jossinet. *Variability of impedivity in normal and pathological breast tissue*. Medical and Biological Engineering and Computing, vol. 34, no. 5, pages 346–350, 1996.
- [Kadah 96] Y.M. Kadah, A.A. Farag, J.M. Zurada, A.M. Badawi & A.B.M. Youssef. *Classification algorithms for quantitative tissue character-*

- ization of diffuse liver disease from ultrasound images.* IEEE Transactions on Medical Imaging, vol. 15, no. 4, pages 466–478, 1996.
- [Khapalov 94] A. Khapalov. *Localization of Unknown Sources for Parabolic Systems on the Basis of Available Observations.* International journal of systems science, vol. 25, no. 8, pages 1305–1322, September 1994.
- [Kou 02] SG Kou. *A jump-diffusion model for option pricing.* Management Science, vol. 48, no. 8, pages 1086–1101, 2002.
- [Kuang 06] X. Kuang & H. Shao. *Maximum Likelihood Localization Algorithm Using Wireless Sensor Networks.* In Innovative Computing, Information and Control, 2006. ICICIC'06. First International Conference on, volume 3, pages 263–266, Aug.30-Sept.1 2006.
- [Kurowski 94] P. Kurowski, I. Ippolito, JP Hulin, J. Koplík & EJ Hinch. *Anomalous dispersion in a dipole flow geometry.* Physics of Fluids, vol. 6, page 108, 1994.
- [Kvarnstrom 05] M. Kvarnstrom. *Estimation of the diffusion coefficient in a mixture model.* Kwantitatieve Methoden, vol. 72, pages 1–23, 2005.
- [Kvarnstrom 06] M. Kvarnstrom & C. Glasbey. *Estimation of the Diffusion Coefficient in a Mixture Model.* Biometrical Journal, vol. 49, no. 2, pages 300–311, August 2006.

- [Liang 01] M.T. Liang & P.J. Su. *Detection of the corrosion damage of rebar in concrete using impact-echo method*. Cement and Concrete research, vol. 31, no. 10, pages 1427–1436, 2001.
- [Maier 00] R.S. Maier, D.M. Kroll, R.S. Bernard, S.E. Howington, J.F. Peters & H.T. Davis. *Pore-scale simulation of dispersion*. Physics of Fluids, vol. 12, page 2065, 2000.
- [Malmivuo 95] J. Malmivuo & R. Plonsey. *Bioelectromagnetism: principles and applications of bioelectric and biomagnetic fields*. Oxford University Press, USA, 1995.
- [Mancini 06] C. Mancini & R. Reno. *Threshold estimation of jump-diffusion models and interest rate modeling*. Manuscript, University of Florence and University of Siena, 2006.
- [Mariamma 00] NK Mariamma & SN Majhi. *Flow of a newtonian fluid in a blood vessel with permeable wall: A theoretical model*. Computers and Mathematics with Applications, vol. 40, no. 12, pages 1419–1432, 2000.
- [Matthes 04] J. Matthes, L. Gröll & H.B. Keller. *Source Localization Based on Pointwise Concentration Measurements*. Sensors & Actuators: A. Physical, vol. 115, no. 1, pages 32–37, September 2004.
- [Matthes 05] J. Matthes, L. Groll & H.B. Keller. *Source Localization by Spatially Distributed Electronic Noses for Advection and Diffusion*. IEEE Transactions on Signal Processing, vol. 53, no. 5, pages 1711–1719, May 2005.

- [Mosher 99] J.C. Mosher, R.M. Leahy & P.S. Lewis. *EEG and MEG: Forward solutions for inverse methods*. IEEE Transactions on Biomedical Engineering, vol. 46, no. 3, pages 245–259, 1999.
- [Nehorai 95] A. Nehorai, B. Porat & E. Paldi. *Detection and Localization of Vapor Emitting Sources*. IEEE Transactions on Signal Processing, vol. 43, no. 1, pages 243–253, June 1995.
- [Nievergelt 98] Yves Nievergelt. *Solution to an Inverse Problem in Diffusion*. SIAM Rev., vol. 40, no. 1, pages 74–80, 1998.
- [Niliot 98] C.L. Niliot. *The boundary-element method for the time-varying strength estimation of point heat sources: application to a two-dimensional diffusion system*. Numerical Heat Transfer, Part B: Fundamentals, vol. 33, no. 3, pages 301–321, 1998.
- [Oka 70] S. Oka & T. Murata. *A theoretical study of the flow of blood in a capillary with permeable wall*. Jap. J. Appl. Phys, vol. 9, pages 345–352, 1970.
- [Ortner 07] M. Ortner, A. Nehorai & A. Jeremic. *Biochemical Transport Modeling and Bayesian Source Estimation in Realistic Environments*. IEEE Transactions on Signal Processing, vol. 55, no. 6, pages 2520–2532, June 2007.
- [Panfilov 97] A.V. Panfilov & A.V. Holden. *Computational biology of the heart*. John Wiley & Son Ltd, 1997.

- [Pedersen 95] A.R. Pedersen. *A new approach to maximum likelihood estimation for stochastic differential equations based on discrete observations*. Scandinavian Journal of Statistics, pages 55–71, 1995.
- [Phillips 00] JW Phillips, RM Leahy & JC Mosher. *MEG-Based Imaging of Focal Neuronal Current Sources1*. In Biomag 96: proceedings of the Tenth International Conference on Biomagnetism, page 310. Springer Verlag, 2000.
- [Pollard Jr 84] J.K. Pollard Jr. *Material and method for removing immunoglobulins from whole blood*, August 7 1984. US Patent 4,464,165.
- [Porat 96] B. Porat & A. Nehorai. *Localizing Vapor Emitting Sources by Moving Sensors*. IEEE Transactions on Signal Processing, vol. 44, no. 4, pages 1018–1021, April 1996.
- [Raab] H. Raab. *Detecting and measuring faint point sources with a CCD*. In Proceedings of the Meeting on Asteroid and Comets in Europe, 2003, May 1-4, 2003, Costitx, Majorca, Spain.
- [Rage 96] T. Rage. *Studies of tracer dispersion and fluid flow in porous media*. PhD thesis, PhD thesis, University of Oslo, Oslo, Norway, 1996.
- [Ram 07] S.S. Ram & VV Veeravalli. *Localization and Intensity Tracking of Diffusing Point Sources Using Sensor Networks*. In Proceedings of IEEE Globecom, 2007.

- [Reif 77] J. Reif & R. Barakat. *Numerical solution of the Fokker-Planck equation via Chebyshev polynomial approximations with reference to first passage time probability density functions*. Journal of Computational Physics, vol. 23, pages 425–445, 1977.
- [Riskin 89] H. Riskin. The Fokker-Planck equation: Methods of solution and applications. Springer, 1989.
- [Rogers 60] D.E. Rogers. *Host mechanisms which act to remove bacteria from the blood stream*. Microbiology and Molecular Biology Reviews, vol. 24, no. 1, pages 50–66, 1960.
- [Rogers 94] JM Rogers & AD McCulloch. *A collocation-Galerkin finite element model of cardiac action potential propagation*. IEEE Transactions on Biomedical Engineering, vol. 41, no. 8, pages 743–757, 1994.
- [Russell 00] R.A. Russell, L. Kleeman & S. Kennedy. *Using volatile chemicals to help locate targets in complex environments*. In Proceedings of the Australian Conference on Robotics and Automation, pages 87–91. Citeseer, 2000.
- [Russell 01] R.A. Russell. *Tracking chemical plumes in constrained environments*. Robotica, vol. 19, no. 04, pages 451–458, 2001.
- [Sachse 04] F.B. Sachse. Computational cardiology: modeling of anatomy, electrophysiology, and mechanics. Springer-Verlag New York Inc, 2004.

- [Sahyoun 09] S.S. Sahyoun, S.M. Djouadi, H. Qi & A. Drira. *Source Localization Using Stochastic Approximation and Least Squares Methods*. In AIP Conference Proceedings, volume 1107, pages 59–64, March 2009.
- [Salles 93] J. Salles, J.F. Thovert, R. Delannay, L. Prevors, J.L. Auriault & PM Adler. *Taylor dispersion in porous media. Determination of the dispersion tensor*. Physics of Fluids A: Fluid Dynamics, vol. 5, page 2348, 1993.
- [Sam 08] A.G. Sam & G.J. Jiang. *Nonparametric Estimation of the Short Rate Diffusion Process from a Panel of Yields*. Journal of Financial and Quantitative Analysis, forthcoming, 2008.
- [Scott 97] L.O. Scott. *Pricing stock options in a jump-diffusion model with stochastic volatility and interest rates: Applications of Fourier inversion methods*. Mathematical Finance, vol. 7, no. 4, pages 413–426, 1997.
- [Shiguemori 02] EH Shiguemori, FP Harter, H.F.C. VELHO, JDS da Silva & B. SP. *Estimation of boundary conditions in conduction heat transfer by neural networks*. Tendencias em Matematica Aplicada e Computacional, vol. 3, no. 2, pages 189–195, 2002.
- [Sørensen 02] H. Sørensen. *Estimation of diffusion parameters for discretely observed diffusion processes*. Bernoulli, pages 491–508, 2002.

- [Srivastava 83] LM Srivastava & VP Srivastava. *On two-phase model of pulsatile blood flow with entrance effects*. Biorheology(Oxford), vol. 20, no. 6, pages 761–777, 1983.
- [Szymczak 03] P. Szymczak & AJC Ladd. *Boundary conditions for stochastic solutions of the convection-diffusion equation*. Physical Review E, vol. 68, no. 3, page 36704, 2003.
- [Terayama 01] H. Terayama, K. Okumura, K. Sakai, K. Torigoe & K. Esumi. *Aqueous dispersion behavior of drug particles by addition of surfactant and polymer*. Colloids and Surfaces B: Biointerfaces, vol. 20, no. 1, pages 73–77, 2001.
- [Vabishchevich 85] PN Vabishchevich. *Numerical solution of the inverse problem of heat conduction by using regularized difference schemes*. Journal of Engineering Physics and Thermophysics, vol. 49, no. 6, pages 1446–1449, 1985.
- [Vonesh 97] E.F. Vonesh & V.M. Chinchilli. *Linear and nonlinear models for the analysis of repeated measurements*. CRC, 1997.
- [Yang 96] C. Yanget al. *The boundary estimation in two-dimensional inverse heat conduction problems*. Journal of Physics D: Applied Physics, vol. 29, pages 333–339, 1996.
- [Yang 97] C. Yanget al. *Inverse estimation of the boundary condition in three-dimensional heat conduction*. Journal of Physics D: Applied Physics, vol. 30, pages 2209–2216, 1997.

- [Yano 89] Y. Yano, K. Yamaoka, Y. Aoyama & H. Tanaka. *Two-compartment dispersion model for analysis of organ perfusion system of drugs by fast inverse Laplace transform (FILT)*. Journal of Pharmacokinetics and Pharmacodynamics, vol. 17, no. 2, pages 179–202, 1989.
- [Zhang 97a] M. Zhang & J. Koplik. *Tracer dispersion in three-dimensional multipole flows*. Physical Review E, vol. 56, no. 4, pages 4244–4258, 1997.
- [Zhang 97b] X.L. Zhang. *Numerical analysis of American option pricing in a jump-diffusion model*. Mathematics of Operations Research, pages 668–690, 1997.
- [Zhukov 03] L. Zhukov & A.H. Barr. *Heart-muscle fiber reconstruction from diffusion tensor MRI*. In Proceedings of the 14th IEEE Visualization 2003 (VIS'03). IEEE Computer Society Washington, DC, USA, 2003.